

SHELLS, ORBIT BIFURCATIONS AND SYMMETRY RESTORATIONS IN FERMI SYSTEMS

A.G. Magner* and M.V. Koliesnik
Institute for Nuclear Research, 03680 Kyiv, Ukraine

K. Arita
Department of Physics, Nagoya Institute of Technology, Nagoya 466-8555, Japan
(Dated: April 20, 2016)

The periodic-orbit theory based on the improved stationary-phase method within the phase-space path integral approach is presented for the semiclassical description of the nuclear shell structure, concerning the main topics of the fruitful activity of V. G. Solovjov. We apply this theory to study bifurcations and symmetry breaking phenomena in a radial power-law potential which is close to the realistic Woods-Saxon one up to about the Fermi energy. Using the realistic parametrization of nuclear shapes we explain the origin of the double-humped fission barrier and the asymmetry in the fission isomer shapes by the bifurcations of periodic orbits. The semiclassical origin of the oblate-prolate shape asymmetry and tetrahedral shapes is also suggested within the improved periodic-orbit approach. The enhancement of shell structures at some surface diffuseness and deformation parameters of such shapes are explained by existence of the simple local bifurcations and new non-local bridge-orbit bifurcations in integrable and partially integrable Fermi-systems. We obtained good agreement between the semiclassical and quantum shell-structure components of the level density and energy for several surface diffuseness and deformation parameters of the potentials, including their symmetry breaking and bifurcation values.

I. INTRODUCTION

Semiclassical periodic-orbit theory (POT) is a convenient tool for analytical studies of the shell structure in the single-particle level density of finite fermionic systems near the Fermi surface [1–8]. This theory relates the oscillating level density and shell-correction energy to the sum of periodic orbits and their stability characteristics, and thus, gives the analytical quantum-classical correspondence. According to the shell-correction method (SCM) [9, 10], the oscillating part of the total energy of a finite fermion system, the so-called shell-correction energy, is associated with an inhomogeneity of the single-particle (s.p.) energy levels near the Fermi surface. The SCM is based on Strutinsky’s smoothing procedure to extract the shell components of the level density and energy, which has to be added to the macroscopic parts, in particular, within the Liquid Drop Model (LDM) [11] or Extended Thomas-Fermi (ETF) approach [12]. Deep foundations of the relation of a quasiparticle spectrum near the Fermi surface to the finite many-body fermionic systems with a strong particles’ interaction, such as atomic nuclei, can be found in Refs. [13, 14] which are based on the Landau quasiparticles’ theory of Fermi liquids [15, 16]. Depending on the level density at the Fermi energy – and with it the shell-correction energy – being a maximum or a minimum, the nucleus is particularly unstable or stable, respectively. This situation varies with particle numbers and deformation parameters of the nucleus, and other parameters of its mean-field potential. In consequence, the shapes of stable nuclei depend strongly on particle numbers and deformations. The SCM was successfully used to describe nuclear masses and deformation energies and, in partic-

ular, fission barriers of heavy nuclei, see the early review by Strutinsky’s group, in which also the microscopic foundations of the SCM are discussed in [10]. Numerous other phenomena for which the shell effects in deformed nuclei play a crucial role were studied in many other publications [7, 8, 17–19]. One of them is related, e.g., to the description of the rotational bands at high nuclear spins [20–22], in particular by using the semiclassical POT [23–34]. The shell effects are always in a center of attention in the description of the collective nuclear dynamics, within the semi-microscopic approaches [17–19], also within the physically transparent Quasiparticle-Phonon Model (QPM) [35–41]. The collective modes were intensively studied within this model, especially in the complex deformed nuclei [37, 42, 43], see also the pioneer works [44–47] concerning the pairing-correlation effects in nuclear physics, as well as within the more microscopical Hartree-Fock (HF) [48] and Hartree-Fock-Bogoliubov (HFB) approaches (see e.g., [18, 49, 50] and references therein), and within the theory of finite Fermi systems [13]. In addition, concerning the main content of this review article, we should mention calculations of the transport coefficients, such as the inertia, friction and moments of inertia within the response function theory [19, 51, 52], by applying the POT [22, 28–33, 53–57].

The idea was to use the POT for a deeper understanding, based on classical pictures, of the origin of the nuclear shell structure and its relation to a possible chaotic nature of the nucleons’ dynamics [3, 5, 7, 8, 58, 59]. This provides us with a transparent description in terms of the classical periodic orbits (POs) for answering, sometimes even analytically, some fundamental questions concerning the physical origins of the double-humped fission barrier and, in particular, of the existence of the isomer minimum [5, 7, 8, 60–63]. Gutzwiller was the first [1] who suggested the Feynman path integral representation for the Green’s function to apply POT in the case of absence of any symmetry of the Hamiltonian, in addition

* Email: magner@kinr.kiev.ua

to its time independence. In this case, the energy E of the particle moving in a mean-field potential is the only one integral of motion. For a given E , the POs are isolated, i.e., any variation of the classical trajectory (CT) leads to a change of the classical action along the CT. The Gutzwiller POT was extended to the continuous symmetries, as rotational and high (e.g., harmonic oscillator) ones, in [3, 5, 64] on the basis of the early investigation of billiard-like systems within another Green's multiple-reflection method by Balian and Bloch [2]. Independently, Berry and Tabor [4] developed their direct Poisson-summation method using the phase-space variables for POs having a high degeneracy¹ in integrable systems.

Some applications of the POT to nuclear deformation energies with pronounced shell effects were presented and discussed by using the phase space variables [4–7] and Maslov-Fedoriuk catastrophe (turning- and caustic-point) theories [65–69]. Within the improved stationary-phase method [8, 61, 62, 69–71] (improved SPM, or ISPM), one can solve the symmetry-breaking and bifurcation problems². See also [7, 72–85] concerning the bifurcation and normal-form theories and semi-analytical uniform approximations. The divergences and discontinuities of the standard SPM (SSPM) [2–4, 6, 7] near the symmetry-breaking and bifurcation points were removed, in particular within the analytical ISPM.

In the way to a more realistic semiclassical calculation, it is important also to account for a diffuseness of the nuclear edge. As found in [84, 86], the shell structure in the radial power-law potential (RPLP) is a good approximation to that of the familiar Woods-Saxon (WS) potential for nuclei in the spatial domain where the particles are bound. We shall generalize the ISPM trace formulas [8, 87] for this potential from two to three dimensions, and discussed various limits to other known potentials as to the harmonic oscillator (HO) and the spherical billiard and to the SSPM results far from the symmetry-breaking and bifurcation points.

In Section II, we outlook the main ingredients of the POT within the extended Gutzwiller approach (EGA) accounting for the bifurcation phenomenon by the ISPM. Some general points of the phase space trace formulas are studied for families of the maximal degeneracy in arbitrary spherical potentials. The POT shell components of the s.p. level density and energy for any Hamiltonians, in particular, for a non-integrable potential like the Hénon-Heiles (HH) Hamiltonian is presented too. The isomer shapes within the fission cavity model with the realistic deformation parameters are discussed in Section III. In Section IV we extend the semiclassical ISPM for the RPLP from the two- to the three-dimensional case. The trace formulas for the level densities and en-

ergy shell corrections will be derived for all PO families found by scaling of the RPLP classical dynamics. Several asymptotics of the ISPM to the well known SSPM, billiard and HO limits will be obtained. The semiclassical calculations of the level density and energy shell corrections are compared with the quantum results for the RPLP for different radial powers. The extensions of the RPLP POT to more realistic deformed potentials with the surface diffuseness is given in Section V. The POT shell structures in these potentials with the oblate-prolate and tetrahedral deformations are analyzed and comparison of the semiclassical and quantum results is displaced in this Section. This review article is summarized in Section VI. Some technical details of our POT calculations are given in Appendix A.

II. GENERAL POT INGREDIENTS

In this section, we shall outlook the POT within the extended Gutzwiller approach by using the phase-space variables. The trace formulae for the semiclassical level density (Section IIA), the ISPM and bifurcations (Section IIB), level density averaging (Section IIC), and the shell-correction energy (Section IID) will be presented in terms of the PO sums. Sections IIE and IIF will be devoted to the specific trace formulae and classical dynamics for the integrable and non-integrable Hamiltonians, respectively.

A. Phase-space trace formula

The level density, $g(E) = \sum_i \delta(E - E_i)$, determined by spectrum levels E_i for the Hamiltonian \hat{H} can be obtained approximately semiclassically by using the phase-space trace formula in \mathcal{D} dimensions [61, 62, 69, 70]:

$$g_{\text{scl}}(E) = \frac{1}{(2\pi\hbar)^{\mathcal{D}}} \text{Re} \sum_{\text{CT}} \int d\mathbf{r}'' \int d\mathbf{p}' \times \quad (1)$$

$$\times \delta(E - H(\mathbf{r}', \mathbf{p}')) |\mathcal{J}_{\text{CT}}(\mathbf{p}'_{\perp}, \mathbf{p}''_{\perp})|^{1/2} \times$$

$$\times \exp \left\{ \frac{i}{\hbar} \Phi_{\text{CT}} - i \frac{\pi}{2} \mu_{\text{CT}} \right\},$$

where $H(\mathbf{r}, \mathbf{p})$ is the classical Hamiltonian in the phase space variables \mathbf{r}, \mathbf{p} , Φ_{CT} the phase integral,

$$\Phi_{\text{CT}} \equiv S_{\text{CT}}(\mathbf{p}', \mathbf{p}'', t_{\text{CT}}) + (\mathbf{p}'' - \mathbf{p}') \cdot \mathbf{r}'' = \quad (2)$$

$$= S_{\text{CT}}(\mathbf{r}', \mathbf{r}'', E) + \mathbf{p}' \cdot (\mathbf{r}' - \mathbf{r}''),$$

see the derivations in Appendix A2. In (1), the sum is taken over all discrete CT manifolds for a particle motion from the initial point $(\mathbf{r}', \mathbf{p}')$ to the final point $(\mathbf{r}'', \mathbf{p}'')$ with a given energy E [69]. A CT can uniquely be specified by fixing, for instance, the initial condition \mathbf{r}'' and the final momentum \mathbf{p}' for a given time t_{CT} of the motion along the CT. $S_{\text{CT}}(\mathbf{p}', \mathbf{p}'', t_{\text{CT}})$ is the action in the momentum representation,

$$S_{\text{CT}}(\mathbf{p}', \mathbf{p}'', t_{\text{CT}}) = - \int_{\mathbf{p}'}^{\mathbf{p}''} d\mathbf{p} \cdot \mathbf{r}(\mathbf{p}). \quad (3)$$

The integration by parts relates (3) to the action

$$S_{\text{CT}}(\mathbf{r}', \mathbf{r}'', E) = \int_{\mathbf{r}'}^{\mathbf{r}''} d\mathbf{r} \cdot \mathbf{p}(\mathbf{r}) \quad (4)$$

¹ The classical degeneracy is defined by the number of independent parameters \mathcal{K} for a continuous family of the classical periodic orbits at a given energy of the particle.

² The simplest PO bifurcation is a change of the number of solutions of the classical dynamic equations from one PO (or, PO family) to two POs (or PO families) with a variation of potential parameters.

[or other generating functions, see (A.11)] in the spatial coordinate space by the Legendre transformation. The Maslov phase μ_{CT} is determined by the number of conjugate (turning and caustics) points along the CT [65–67]. We introduced here a local phase-space 3D coordinate system, $\mathbf{r} = \{x, y, z\}$, $\mathbf{p} = \{p_x, p_y, p_z\}$, related to a PO which gives the main contribution into the trace integral among the CTs. The variables x, p_x are locally the parallel and $\{\mathbf{r}_\perp, \mathbf{p}_\perp\}$ the perpendicular (with respect to a CT) phase-space coordinates specified more below ($\mathbf{r}_\perp = \{y, z\}$, $\mathbf{p}_\perp = \{p_y, p_z\}$) [1, 5, 7]. In (1), $\mathcal{J}_{\text{CT}}(\mathbf{p}'_\perp, \mathbf{p}''_\perp)$ is the Jacobian for the transformation from an initial perpendicular-to-CT momentum component \mathbf{p}'_\perp to a final one \mathbf{p}''_\perp . We can take first the integral over p'_\parallel of the momentum integration by using the energy conservation δ -function,

$$\delta g_{\text{scl}}(E) = \frac{m}{(2\pi\hbar)^3} \text{Re} \sum_{\text{CT}} \int d\mathbf{r}'' \int \frac{d\mathbf{p}'_\perp}{p'_\parallel} \times \quad (5)$$

$$\times |\mathcal{J}_{\text{CT}}(\mathbf{p}'_\perp, \mathbf{p}''_\perp)|^{1/2} \exp \left[\frac{i}{\hbar} \Phi_{\text{CT}} - \frac{i\pi}{2} \mu_{\text{CT}} \right].$$

The CT is determined by the Hamilton equations with the energy conservation condition, $E = H(\mathbf{r}'', \mathbf{p}'') = H(\mathbf{r}', \mathbf{p}')$.

For calculations of the trace integral by the SPM, one may write the stationary phase conditions in both \mathbf{p}' and \mathbf{r}'' variables. According to the definitions (2) and (3), the stationary phase condition for the \mathbf{p}' variable is a closing condition in the spacial coordinates:

$$\left(\frac{\partial \Phi_{\text{CT}}}{\partial \mathbf{p}'} \right)^* \equiv (\mathbf{r}' - \mathbf{r}'')^* = 0. \quad (6)$$

The star means that any quantity in the circle brackets is taken at the stationary point, e.g., $\mathbf{p}' = \mathbf{p}'^*$. In the next integration over \mathbf{r}'' in (5) by the SPM we use the Legendre transformation (2). Thus, according to (6), the closing condition leads to the expression $\Phi_{\text{PO}}^* = S_{\text{PO}}(\mathbf{r}', \mathbf{r}'', E)$. The stationary-phase equation for this integration over spacial coordinates, $\mathbf{r} = \mathbf{r}' = \mathbf{r}''$, writes [1]

$$\left(\frac{\partial \Phi_{\text{CT}}}{\partial \mathbf{r}'} + \frac{\partial \Phi_{\text{CT}}}{\partial \mathbf{r}''} \right)^* \equiv \left(\frac{\partial S_{\text{CT}}}{\partial \mathbf{r}'} + \frac{\partial S_{\text{CT}}}{\partial \mathbf{r}''} \right)^* \equiv \quad (7)$$

$$\equiv -(\mathbf{p}' - \mathbf{p}'')^* = 0,$$

where the star means $\mathbf{r}' = \mathbf{r}'' = \mathbf{r}^*$ along with $\mathbf{p}'' = \mathbf{p}''^* = \mathbf{p}^*$. Equations (6) and (7) are the closing conditions for a CT in the phase space, too. Therefore, the *stationary phase* conditions are equivalent to these *periodic-orbit* equations. One of the SPM integrations in (1), for instance over the parallel momentum p'_\parallel in the local Cartesian coordinate system introduced above, is identity due the energy conservation, and therefore, can be taken exactly. The PO conditions (6) and (7) can be sometimes conveniently written in a more symmetric equivalent form,

$$\left(\frac{\partial \Phi_{\text{CT}}}{\partial \mathbf{p}''} \right)^* \equiv (\mathbf{r}' - \mathbf{r}'')^* = 0, \quad (8)$$

$$\left(\frac{\partial \Phi_{\text{CT}}}{\partial \mathbf{r}''} \right)^* \equiv (\mathbf{p}'' - \mathbf{p}')^* = 0.$$

After applying these PO equations [(6) and (7), or (8)], with accounting for the breaking of symmetries one may arrive at the trace formula in terms of the sum over POs [7, 8].

The total ISPM trace formula is the sum of the contribution of all POs (families with the classical degeneracy $\mathcal{K} \geq 1$ and isolated orbits ($\mathcal{K} = 0$),

$$\delta g_{\text{scl}}(E) = \sum_{\text{PO}} \delta g_{\text{PO}}(E), \quad (9)$$

where

$$\delta g_{\text{PO}}(E) = \text{Re} \left\{ A_{\text{PO}} \exp \left[\frac{i}{\hbar} S_{\text{PO}}(E) - \frac{i\pi}{2} \mu_{\text{PO}} \right] \right\}, \quad (10)$$

with A_{PO} being the amplitude of density oscillations depending on the PO classical degeneracy \mathcal{K} and stability factors. $S_{\text{PO}}(E)$ is the action and μ_{PO} the Maslov phase along the PO [1, 3, 7, 8, 31].

B. BIFURCATIONS AND AMPLITUDE ENHANCEMENT

For solving bifurcation problems in integrable and non-integrable systems, more exact integrations are required. In the SPM, after performing the exact integrations over the “cyclic” (“parallel”) phase-space variables related to the integrals of motion (the energy, angular momentum and others corresponding to the symmetries of the Hamiltonian), one uses an expansion of the action phase Φ_{CT} in the remaining “perpendicular” variables $\xi = \{\mathbf{r}', \mathbf{p}''\}_\perp$ in the integrand of (1) over ξ near the stationary point ξ^* ,

$$\Phi_{\text{CT}}(\xi) = \Phi_{\text{PO}} + \frac{1}{2} \Phi_{\text{PO}}''(\xi^*)(\xi - \xi^*)^2 + \quad (11)$$

$$+ \frac{1}{6} \Phi_{\text{PO}}'''(\xi^*)(\xi - \xi^*)^3 + \dots, \quad \Phi_{\text{PO}} = \Phi_{\text{CT}}^* = \Phi_{\text{CT}}(\xi^*).$$

To demonstrate the key point of our derivations of the trace formula, we consider here only one (one-dimensional) variable, called ξ again, from the phase space integration variables in (1), on which we meet a bifurcation (catastrophe) point in applying the SPM. (We shall give comments if this might lead to a misunderstanding.) In the standard SPM, the above expansion is truncated at the 2nd order term and the integration over the variable ξ is extended to $\pm\infty$. The integration can be performed analytically and yields a Fresnel integral, see e.g. [7].

However, one meets singularities using the standard SPM which are related to zeros or infinities of $\Phi_{\text{PO}}''(\xi^*)$ (or of eigenvalues of the corresponding matrix in the case of several integration variables ξ) while $\Phi_{\text{PO}}'''(\xi^*)$ remains finite in the simplest case. These singularities occur when a PO (isolated or family) undergoes a bifurcation at the stationary point ξ^* under the variation of some parameter (e.g., energy or deformation). The Fresnel integrals of the standard SPM sketched above will then diverge. In order to avoid such singularities, we observe that the bifurcation problem is similar to the caustic singularity, as two closed stationary points, considered by Fedoriuk within the catastrophe theory

[65, 67], adopted to its specific position at the edge of the phase-space volume accessible for the classical motion (see also Appendix A in [69]). Therefore, we employ what we call the “improved stationary-phase method” (ISPM) [8, 61, 62, 69, 70]. Hereby the integration over ξ in (1) is restricted to the *finite limits* defined by the classically allowed phase space region through the energy-conserving delta function in the integrand of (1). The expansion (11) of the action phases, and similarly, of the amplitudes in (3) is generally used up to the second- and zero-order terms, respectively, and if necessary, to higher order terms in $\xi - \xi^*$.

In the simplest version of the ISPM, the expansion of the phase is truncated at 2nd order, keeping the finite integration limits ξ_- and ξ_+ given by the accessible region of the classical motion in (1). It will lead to a factor like

$$e^{i\Phi_{\text{PO}}/\hbar} \int_{\xi_-}^{\xi_+} d\xi \exp \left[\frac{i}{2\hbar} \Phi''_{\text{PO}} (\xi - \xi^*)^2 \right] \propto \quad (12)$$

$$\propto \frac{1}{\sqrt{\Phi''_{\text{PO}}}} e^{i\Phi_{\text{PO}}/\hbar} \text{erf} [Z_-, Z_+],$$

where $\text{erf}(z_1, z_2)$ is the generalized error function with complex arguments

$$\text{erf}(z_1, z_2) = \frac{2}{\sqrt{\pi}} \int_{z_1}^{z_2} e^{-z^2} dz, \quad (13)$$

$$Z_{\pm} = (\xi_{\pm} - \xi^*) \sqrt{-\frac{i}{2\hbar} \Phi''_{\text{PO}}}.$$

Note that the above expression (12) has no divergence at the bifurcation point where $\Phi''_{\text{PO}}(\xi^*) = 0$, since the error function (13) also goes to zero linearly in $\sqrt{\Phi''_{\text{PO}}}$ [cf. the second equation in (13)], which keeps the result finite. [For the case of several variables ξ for which we find zeros or infinities of eigenvalues of the matrix $\Phi''_{\text{PO}}(\xi^*)$, we diagonalize this matrix and reduce the Fresnel-like integrals to products of error functions similar to (12).]

This procedure is proved to be valid in the semiclassical limit by the Maslov-Fedoriuk theorem [65–67]. In this way, we can derive contributions from each periodic orbit free of divergences at any bifurcation point, and the oscillating part of the level density can be approximated by the following *semiclassical trace formula*:

$$\delta g(E) \simeq \delta g_{\text{scl}}(E) = \sum_{\text{PO}} \delta g_{\text{PO}}(E), \quad (14)$$

with (10) for the PO contribution $\delta g_{\text{PO}}(E)$. The amplitude $A_{\text{PO}}(E)$ in (10) (complex, in general) is of the order of the phase space volume occupied by CTs, and the factor given in (12) which depends on the degeneracies and stabilities of the POs, respectively. Sometimes, it is convenient to split the Maslov phase which is invariant along the PO, $\mu_{\text{PO}} = \sigma_{\text{PO}} + \phi_d$, into two terms where σ_{PO} is called the Maslov index. ϕ_d is an extra phase that depends on the dimensionality of the system and degeneracy \mathcal{K} of the PO manifold. (ϕ_d is zero when all orbits are isolated ($\mathcal{K}=0$), as defined in [1]). The sum in (14) is an asymptotic one, correct to leading order in $1/\hbar^{1/2}$, and in non-integrable systems it is hampered by convergence problems [1]. For systems in which all orbits are isolated in phase space, Gutzwiller [1] expressed the amplitudes $A_{\text{PO}}(E)$ (which are real in this case) explicitly in terms of the periods and stability matrices of the

POs, see some examples below. His trace formula has become famous, in particular in connection with “*quantum chaos*” [1]. Notice that according to (12), any more exact integration in (1) over a bifurcation/catastrophe variable ξ of the improved SPM leads to an enhancement of the amplitude A_{PO} in the transition interval from the bifurcation point to the region of the asymptotic (SSPM) behaviour of A_{PO} . The height of this maximum is of order $1/\hbar^{1/2}$ as compared to the result of the standard SPM integration (integrable or non-integrable system; see more specific examples in Sections IIE, IIF and IIIE). Thus, for the family with the degeneracy \mathcal{K} , one has the enhancement of the level density amplitude,

$$A_{\text{PO}}^{(\mathcal{K})} \sim A_{\text{PO}}^{\text{G}} \hbar^{-\mathcal{K}/2}, \quad (15)$$

where A_{PO}^{G} is the Gutzwiller trace-formula amplitude for the contributions of isolated POs. In addition, for non-integrable systems, one finds a local enhancement of the PO amplitude A_{PO} as compared to the Gutzwiller amplitude, see examples below (Sections IIF and V).

The trace formula (14) thus relates the quantum oscillations in the level density to quantities that are determined purely by the classical system. Strutinsky and his collaborators, in their search for simple physical explanations of shell effects, realized that this kind of approach could help to understand the shell effects in terms of classical pictures [5, 8]. However, in the application to nuclear physics, Gutzwiller’s expression for the amplitudes $A_{\text{PO}}(E)$ could not be used, because they diverge when the POs are not isolated in phase space. This happens whenever a system has continuous (e.g., rotational) symmetries, and hence, for most typical shell-model potentials (except in non-axially deformed situations). Therefore, Gutzwiller’s theory was extended to systems with continuous symmetries [3, 7, 8].

Trace formulae for systems with all kinds of mixed symmetries, including the integrable cases, were also developed later by various other authors. The treatment of bifurcations is still an on-going subject of current research. Uniform approximations were constructed for orbit bifurcations and symmetry breaking under the variation of the energy or a potential parameter; references to most of these developments are given in [7, 8].

C. Averaged level density

For comparison with quantum densities we need also to use a local averaging of the trace formula (9) over the spectrum. As this trace formula has the simple form as a sum of separating PO terms everywhere, including the bifurcations, one can take approximately analytically the integral over energies with Gaussian weight factor (folding integral) [3, 7, 8, 87]. As the result, for this averaged density $\delta g_{\Gamma}^{\text{scl}}(E)$ with the averaging parameter Γ , which is much smaller than the Fermi energy E_F , one obtains

$$\delta g_{\Gamma}^{\text{scl}}(E) = \sum_{\text{PO}} \delta g_{\text{PO}}(E) \exp \left[- (t_{\text{PO}} \Gamma / \hbar)^2 \right], \quad (16)$$

where t_{PO} is the period for a PO, $t_{\text{PO}} = MT_{\text{PO}}$, M the PO repetition number, T_{PO} the period for a primitive ($M = 1$) PO.

The total ISPM level density as function of the energy E is given by

$$g_{\Gamma}^{\text{scl}}(E) = g_{\text{ETF}}(E) + \delta g_{\Gamma}^{\text{scl}}(E), \quad (17)$$

where $g_{\text{ETF}}(E)$ is the average part obtained within the extended Thomas-Fermi (ETF) approximation [7].

D. Shell-correction energy

The PO expansion for the shell-correction energy δU_{scl} can be expressed in terms of the oscillating PO component of level density $\delta g_{\text{PO}}(E)$ (10) at the Fermi energy E_F [3, 7, 62, 70, 87]

$$\begin{aligned} \delta U_{\text{scl}} &= 2 \sum_{\text{PO}} \frac{\hbar^2}{t_{\text{PO}}^2} \delta g_{\text{PO}}(E_F) = \\ &= 2 \text{Re} \sum_{\text{PO}} \left(\frac{\hbar}{MT_{\text{PO}}} \right)^2 A_{\text{PO}} \times \\ &\times \exp \left[\frac{i}{\hbar} S_{\text{PO}}(E_F) - \frac{i\pi}{2} \mu_{\text{PO}} \right], \end{aligned} \quad (18)$$

where $t_{\text{PO}} = MT_{\text{PO}}(E_F)$ is the time of particle motion along the PO (taking into account its repetition number M) at the Fermi energy $E = E_F$ as $\delta g_{\text{PO}}(E_F)$, T_{PO} is the period for the primitive ($M = 1$) PO. The factor 2 takes into account the spin degeneracy for neutron or proton Fermi systems. The Fermi energy E_F is related to the conservation of the particle number N through the equation:

$$N = \int_0^{E_F} dE g(E). \quad (19)$$

Note that the shell-correction energy δU is the observed physical quantity independent of any artificial averaging parameter Γ , in contrast to the level density $g_{\Gamma}^{\text{scl}}(E)$. The convergence of the PO sum (18) is ensured by the factor, \hbar^2/t_{PO}^2 , in addition to the amplitude A_{PO} of the oscillating level density $\delta g_{\text{PO}}(E_F)$ (10). Therefore, the short-time POs (their families) yield the main contributions into the PO sum (18) if they occupy enough large phase-space volume.

E. Spherical potentials

1. Trace formula in action-angle variables

We now transform the phase space trace formula (1) from the Cartesian phase space variables $\{\mathbf{r}; \mathbf{p}\}$ to the canonical angle-action coordinates $\{\Theta; \mathbf{I}\}$. They are specified in the spherical angle-action variables as $\{\Theta_r, \Theta_{\theta}(= \Theta), \Theta_{\varphi}(= \varphi); I_r, I_{\theta}, I_{\varphi}\}$, and then, $\{\Theta_r, \theta, \varphi; I_r, L, L_z\}$. The last variables have immediately physical meaning, and therefore, simpler to use for the integrable spherically symmetric Hamiltonian (21).

They parametrize the action variables $I_{\theta} = I_{\theta}(L, L_z)$ and $I_{\varphi} = L_z$ so that the CT characteristics, such as the curvature, are simplified for these potentials. In particular, for integrable systems the action-angle variables are preferably useful because in this case the Hamiltonian H does not depend on the angle variables Θ , i.e., $H = H(\mathbf{I}) = H(I_r, I_{\theta}, I_{\varphi}) = H(I_r, L)$. From (1) one simply has

$$\begin{aligned} g_{\text{scl}}(E) &= \frac{1}{(2\pi\hbar)^3} \text{Re} \sum_{\text{PO}} \int d\Theta'_r d\theta' d\varphi' \times \\ &\times \int dI_r dL dL_z \delta(E - H(I_r, L)) \times \\ &\times |\mathcal{J}_{\text{CT}}(\mathbf{p}_{\perp}'', \mathbf{p}_{\perp}')|^{1/2} \exp \left[\frac{i}{\hbar} \Phi_{\text{CT}} - \frac{i\pi}{2} \mu_{\text{CT}} \right]. \end{aligned} \quad (20)$$

The phase Φ_{CT} (2) expressed in terms of the action-angle variables through the actions (3) or (4) (standard generating functions) are considered in the mixed representation. The Jacobian $\mathcal{J}(\mathbf{p}_{\perp}'', \mathbf{p}_{\perp}')$ is also transformed to the new variables. We took also into account explicitly that the actions \mathbf{I} ($\{I_r, I_{\theta}, I_{\varphi}\}$ or $\{I_r, L, L_z\}$) are constants of motion for the spherical integrable Hamiltonian omitting the upper subscripts in \mathbf{I} as related to their initial (prime) and final (double prime) values. As usual, one also employs some Jacobian transformations, taking into account that there is no variations in the parallel x direction along the PO. The Jacobian of canonical transformations equals one, and $\partial I_{\theta}/\partial L = 1$ and $dI_{\theta}dI_{\varphi} = dLdL_z$ from the spherical symmetry. The integration limits for L_z are obviously $-L \leq L_z \leq L$, and for L , one has $0 \leq L \leq L_{\text{max}}$ where L_{max} depends of the energy E and will be specified below. Note that, in spite of non-orthogonality of the angle-action coordinate system, there are still the definite relations between the parallel (or perpendicular) components of quantities in actions $S_{\text{CT}}(\mathbf{r}', \mathbf{r}'', E)$ in the Cartesian and the angle-action coordinate system. They serve the conservation of actions I_i for integrable Hamiltonians along the trajectory CT [69]. Therefore, it makes sense to relate x components I_x , Θ_x and corresponding y, z components of actions and angles \hat{q} to the “parallel” and “perpendicular” ones with respect to the reference POs in the trace formula (20), respectively. Similar relations between the corresponding spherical components as r, p_r and Θ_r, I_r can be found too.

The PO solutions to the stationary phase equations (6) and (7) are also invariants with respect to the considered canonical transformation as the Hamiltonian which altogether always can be expressed through both the Cartesian, and the angle-action coordinates, also in the canonical spherical coordinates, by using the suitable transformation equations.

The main strategy in the next derivations of the trace formulas is following. First, for any spherical Hamiltonians one has no dependence of the integrand in the phase space trace formulas (20) on the angular momentum projection L_z and corresponding azimuthal angle φ'' . Then, the integral over L_z is $2L$ and the integral over φ'' equals 2π , except for the diametrical contribution for which $L = 0$, see below. Second, in (20), as in the Cartesian phase-space variables considered above, for

any spherical Hamiltonians we take exactly the integral over the parallel actions, I_r or L , and get $\int d\Theta'_r/\omega_r = T_r$ or $\int d\Theta'/\omega_\theta = T_\theta$ for $\mathcal{K} = 3$ families and diameter $\mathcal{K} = 2$ POs or circle ($\mathcal{K} = 2$) orbits, respectively, because of the δ -function conserving the particle energy E , and the invariance of the action along a PO [69]. The diameter family contribution into the trace formula is exclusive case due to the zero angular momentum, $L = L_z = 0$. This case will be considered separately for the RPLP. Third, we are left with the perpendicular action and angle variables. For the derivation of the leading family ($\mathcal{K} = 3$) terms we have no dependence of the angle variables and obtain the semiclassical Poisson summation trace formula [4, 7]. Then, we shall apply the ISPM for the calculation of the integral over the “perpendicular” action variable with the corresponding stationary phase condition. For the contribution of the circular-orbit families with $\mathcal{K} = 2$, there is the isolated stationary point ($r'' = r''^* = r_c, p'_r = p'_r{}^* = 0$) in one of center planes in the “perpendicular” Θ'_r and I_r integration variables in the spherical phase-space variables r'' and p'_r .

2. Classical dynamics

For any spherical potentials $V(r)$ the Hamiltonian H in the spherical canonical phase-space variables $\{r, \theta, \varphi, p_r, p_\theta, p_\varphi\}$ writes

$$H = \frac{1}{2m} \left(p_r^2 + \frac{p_\theta^2}{r^2} + \frac{p_\varphi^2}{r^2 \sin^2 \theta} \right) + V(r) = E. \quad (21)$$

Here, $p_\varphi = L_z$ is the projection of the angular momentum on arbitrary z axis, $p_\theta = (L^2 - L_z^2 / \sin^2 \theta)^{1/2}$, $L = |\mathbf{L}|$ is the angular momentum, $|L_z| \leq L$, and $p_r(r)$ is defined by

$$p_r(r) \equiv \sqrt{p^2(r) - \frac{L^2}{r^2}}, \quad (22)$$

$$p(r) = \sqrt{2m[E - V(r)]}.$$

As the angular momentum L is conserved for the motion of a particle in a spherically symmetric mean field $V(r)$, all CTs are lying in a plane crossing the center $r = 0$. Integrating the differential equations (A.1), one obtains the radial $r = r(t)$ and the angle $\theta = \theta(t)$ CT, i.e., a CT $r = r(\theta)$ in the azimuthal plane. For one period $t = T$ along the PO at the boundary condition $r = r''$ for $\Theta = \Theta''$, one has (Appendix A5)

$$\theta'' - \theta' = -\pi \frac{\partial I_r}{\partial L}, \quad (23)$$

where I_r is the radial action in the spherical action-angle variables :

$$I_r = \frac{1}{2\pi} \oint p_r dr = \quad (24)$$

$$= \frac{1}{\pi} \int_{r_{min}}^{r_{max}} dr \sqrt{2m[E - V(r)] - \frac{L^2}{r^2}},$$

$$I_\theta = \frac{1}{2\pi} \oint p_\theta d\theta = \frac{1}{\pi} \int_{\theta_{min}}^{\theta_{max}} d\theta \sqrt{L^2 - \frac{L_z^2}{\sin^2 \theta}},$$

$$I_\varphi = \frac{1}{2\pi} \oint p_\varphi d\varphi = L_z.$$

The turning points r_{min} , r_{max} and θ_{min} , θ_{max} are the solutions of equations:

$$p_r^2(r, L) \equiv 2m[E - V(r)] - \frac{L^2}{r^2} = 0, \quad (25)$$

$$L^2 - \frac{L_z^2}{\sin^2 \theta} = 0.$$

The Hamiltonian $H(\mathbf{r}, \mathbf{p})$ (21), as expressed through the spherical action-angle variables, does not depend on the cyclic angle variables. From (A.2) for the frequencies $\omega_\theta = \partial H / \partial I_\theta$ and $\omega_r = \partial H / \partial I_r$, the periodic-orbit equations (6) and (7) take the form of the following resonance conditions:

$$f(L) \equiv \omega_\theta / \omega_r \equiv -\partial I_r(E, L) / \partial L \equiv \quad (26)$$

$$\equiv \frac{L}{\pi} \int_{r_{min}}^{r_{max}} \frac{dr}{r^2 \sqrt{2m[E - V(r)] - L^2/r^2}} =$$

$$= n_\theta / n_r, \quad \omega_\theta / \omega_\varphi \equiv 1,$$

where n_θ and n_r are co-primitive integers. The energy surface $I_r = I_r(E, L)$ (24) is simplified to a function of one variable L for a given energy E of the particle because the second equation for the ratio of frequencies, $\omega_\theta / \omega_\varphi$, is the identity [$I_\theta = L$ for $L_z = 0$, according to (24)]. The solutions to the first PO equation in (26) for $L = L^*(n_r, n_\theta)$ define the three-parametric families ($\mathcal{K} = 3$) of orbits $M(n_\theta, n_r)$. The angular momentum projection L_z , and the two single-valued integrals of motion related to the two fixed rationals for ω_θ / ω_r and $\omega_\theta / \omega_\varphi$ from the PO conditions can be taken as parameters [3, 5].

Except for obvious two-parametric ($\mathcal{K} = 2$) diameter families at $L = 0$, there is also the specific $\mathcal{K} = 2$ family of circle orbits at another edge $L = L_C$ of the energy surface $I_r = I_r(E, L)$. In a fixed plane crossing the center with radius $r = r_{min} = r_{max} = r_c$, one has the isolated circle PO. The first equation in (25) determines the turning points $r_{min}(L)$ and $r_{max}(L)$ as functions of L at the fixed energy E and their cross gives the specific $L = L_C = p(r_C)r_C$.

Note that according to the expression for the radial momentum p_r from (22) which must be real, the maximal angular momentum L is namely this L_C , which is related to the zero p_r . With the zero minimal value of the angular momentum L , one finds $0 \leq L \leq r_C p(r_C) = r_C \sqrt{2m(E - V(r_C))} = L_C$. The maximal value of the angular momentum $L = L_C$ is related to a circular orbit and the minimal one $L = 0$ corresponds to a diameter. The critical values $r = r_C$ and $L = L_C$ are determined as the solution of the system of the two equations with respect to r and L :

$$p_r^2(r, L) = 0, \quad \frac{d}{dr} p_r^2(r, L) = 0, \quad (27)$$

with $d^2 p_r^2(r, L) / dr^2 \neq 0$, as assumed to be the case for the spherical potentials as considered below. The first equation claims that there is no radial velocity, $\dot{r} = 0$, and the next equation is that the radial force is equilibrated by the centrifugal force.

Another general key quantity in the POT is the curvature K of the energy surface $I_r = I_r(E, L)$,

$$K = \frac{\partial^2 I_r}{\partial I_\theta^2} = \frac{\partial^2 I_r(E, L)}{\partial L^2} = -\frac{\partial f(L)}{\partial L}, \quad (28)$$

where $f(L)$ is the ratio of frequencies defined in (26).

F. Symmetry breaking and bifurcations in a non-integrable potential

Recent studies of the POT are focused on overcoming catastrophe problems in the derivation of the semiclassical trace formulae arising in connection with symmetry breaking and bifurcation phenomena, where the standard stationary-phase method fails (see [1]). Semi-analytical uniform approximations solving these problems for the case of well separated pitchfork bifurcations in the non-integrable Hénon-Heiles (HH) potential were suggested in [82, 88], using the normal-form theory of non-linear dynamics [75, 77, 78].

In this subsection, we derive an analytical trace formula for the semiclassical level density of the HH potential, employing the improved stationary-phase method (Section IIB) [69] valid for arbitrarily dense sequences of pitchfork bifurcations near the saddle-point energy and for harmonic-oscillator symmetry breaking in the limit of small energies. In this respect, the regular-to-chaotic transition in Fermi systems becomes important for the understanding of its influence on shell correction amplitudes. Figure 1 shows transparently such a transition through Poincaré Surfaces of Section (PSS) of the non-linear classical dynamics for the HH potential as a simple nontrivial example [7, 89], see also [90–92] for the PSS and Lyapunov exponents in the three-dimensional axially symmetric Legendre-polynomial and spheroidal billiards. The PSS is a successive crossing points of a classical trajectory with a given plane (surface of section) in the phase space. The regular trajectory is confined in a torus, and the crossing points of such a trajectory with the PSS will accumulate on a certain closed curve. On the other hand, the chaotic trajectory will make a scattered plot where a certain area is randomly filled by the crossing points. As shown in this figure, the obvious transition from chaos to order occurs with dimensional decreasing energy e of the particle (in units of the saddle energy) from the saddle ($e = 1$) to a small-energy (harmonic-oscillator) limit $e \rightarrow 0$. We show below the relation of this behavior of the PSS to the amplitudes of oscillations in the level density (density of states) and total energy of fermion systems.

1. Trace formulae, symmetry breaking and bifurcations

The level density $g(E)$ (1) is obtained from the semiclassical Green's function [1] by taking its trace in the phase-space Poincaré variables Q, p [69, 75, 77, 78]:

$$g_{\text{scl}}(E) = \frac{1}{(2\pi\hbar)^2} \text{Re} \sum_{\text{CT}} \int dQ \int dp t_{y\text{CT}} \times \quad (29)$$

$$\times |\mathcal{J}_{\text{CT}}(p, P)|^{1/2} \times$$

$$\times \exp \left\{ \frac{i}{\hbar} \left[\hat{S}_{\text{CT}}(Q, p, E) - Qp \right] - \frac{i\pi}{2} \mu_{\text{CT}} \right\}.$$

Here Q and p are the final x'' and initial p'_x coordinates in the phase-space variables x, y, p_x, p_y perpendicular to a reference classical trajectory in two dimensions, $t_{y\text{CT}} = m \oint dy/p_y$ is the primitive partial period of the y motion along the CT, $\hat{S}_{\text{ct}}(Q, p, E)$ the generating function, μ_{CT} the Maslov phase, and $\mathcal{J}_{\text{CT}}(p, P)$ is the Jacobian for the transformation between the variables shown as its arguments. The ISPM generating function $\hat{S}_{\text{CT}}(Q, p, E)$ is defined by

$$\hat{S}_{\text{CT}}(Q, p, E) = S_{\text{CT}}(Q, p, E) + qp, \quad (30)$$

where $S_{\text{CT}}(Q, p, E)$ is the action $S_{\text{CT}}(\mathbf{r}', \mathbf{r}'', E) = \int_{\mathbf{r}'}^{\mathbf{r}''} \mathbf{p} \cdot d\mathbf{r}$ expressed in terms of the Poincaré variables Q and p through the mapping transformation equations $Q = Q(q, p)$ and $P = P(q, p)$ along a CT (\mathbf{r}' and \mathbf{r}'' are the initial and final spatial coordinates of the CT). It can be replaced by a (truncated) fourth-order expansion around the stationary points Q^*, p^* which correspond to the POs, $Q^* = q$, $p^* = P$ [69]. For pitchfork bifurcations, the expansion of the generating function $\hat{S}_{\text{CT}}(Q, p, E)$ (30) is similar to the normal forms [75, 77, 78] with the following power series in $Q - Q^*$ and $p - p^*$:

$$S_{\text{CT}}(Q, p, E) = S_{\text{PO}}(E) + \epsilon_{\text{PO}}^{(Q)}(Q - Q^*)^2 + \quad (31)$$

$$+ a_{\text{PO}}^{(Q)}(Q - Q^*)^4 + \epsilon_{\text{PO}}^{(p)}(p - p^*)^2 + a_{\text{PO}}^{(p)}(p - p^*)^4,$$

where $S_{\text{PO}}(E)$ is the action along the PO. Performing also more exact integrations over Q and p in (29), one obtains for the case of pitchfork bifurcations

$$\delta g_{\text{scl}}(E) = \frac{1}{(2\pi\hbar)^2} \text{Re} \sum_{\text{PO}} \frac{T_{\text{PO}}}{[\hbar^2 a_{\text{PO}}^{(Q)} a_{\text{PO}}^{(p)}]^{1/4}} \times \quad (32)$$

$$\times \mathcal{A}(\xi_{\text{PO}}^{(Q)}) \mathcal{A}(\xi_{\text{PO}}^{(p)}) \exp \left[\frac{i}{\hbar} S_{\text{PO}}(E) - \frac{i\pi}{2} \sigma_{\text{PO}} - i\phi \right],$$

where T_{PO} is the period for a primitive PO, $S_{\text{PO}}(E)$ is its full action (including repetitions) at energy E , and

$$\mathcal{A}(\xi) = \int_{z_-}^{z_+} dz \exp [i(\xi z^2 + z^4)], \quad (33)$$

$$\xi = \epsilon/(\hbar a)^{1/2},$$

is the amplitude factor; ϵ and a (for $a > 0$) are the coefficients in the power expansion of the generating function $\hat{S}_{\text{CT}}(Q, p, E)$ (30) with (31) in $Q - Q^*$ and $p - p^*$, which are proportional to the 2nd and 4th derivatives of $\hat{S}_{\text{CT}}(Q, p, E)$ at the stationary points Q^* and p^* ; σ_{PO} is the Maslov index related to the turning and caustic points along the POs, ϕ a constant phase independent of the PO. The integration (33) is performed over the finite classically accessible region of the Poincaré variables Q and p , denoted here as

$$z = \frac{Q - Q^*}{(a^{(Q)}/\hbar)^{1/4}}, \quad \text{or} \quad z = \frac{p - p^*}{(a^{(p)}/\hbar)^{1/4}}, \quad (34)$$

i.e. from $z_-^{(Q)}$ to $z_+^{(Q)}$ and from $z_-^{(p)}$ to $z_+^{(p)}$, respectively, with

$$z_{\pm}^{(Q)} = \frac{Q_{\pm} - Q^*}{(a^{(Q)}/\hbar)^{1/4}}, \quad z_{\pm}^{(p)} = \frac{p_{\pm} - p^*}{(a^{(p)}/\hbar)^{1/4}}. \quad (35)$$

In (32), the sum runs over the straight-line orbits A_σ , the rotational orbits R_σ , and the librational orbits L_σ of the standard HH Hamiltonian [7, 81, 82] (here in units with $m = \omega = \hbar = 1$):

$$H = \frac{1}{2}(\dot{x}^2 + \dot{y}^2) + \frac{1}{2}(x^2 + y^2) + \alpha\left(x^2y - \frac{y^3}{3}\right). \quad (36)$$

Using the barrier energy $E_{\text{barr}} = 1/(6\alpha^2)$ as dimensionless energy unit, $e = E/E_{\text{barr}} = 6\alpha^2 E$, and the following scaled variables

$$p_u = \alpha p_x, \quad p_v = \alpha p_y, \quad u = \alpha x, \quad v = \alpha y, \quad (37)$$

$$h = 3(\dot{u}^2 + \dot{v}^2) + 3(u^2 + v^2) + 6vu^2 - 2v^3,$$

one obtains classical dynamic equations independent of the parameter α

$$\ddot{u} = -u - 2uv, \quad \ddot{v} = -v + v^2 - u^2. \quad (38)$$

The scaled HH potential is shown in Fig. 2 as equipotential lines, and the orbits A, B and C (at $e = 1$) are presented, too. The HH potential is invariant under rotations about 120 degrees, which leads to a discrete degeneracy of the orbits. Such a degeneracy can be simply taken into account multiplying the amplitudes in the trace formula (32) by a factor 3. The cut along $u = 0$ (right) shows a barrier at the saddle $e = 1$ with two turning points $v_1 \leq v_2$ at $0 < e < 1$; v_n are the real solutions of the cubic equation $e = 3v^2 - 2v^3 \leq 1$ (A.45).

In order to simplify the amplitude function \mathcal{A} in the ISPM trace formula (32), we note that sufficiently far from the symmetry breaking at $E = 0$, the integration limits in (33) can be extended to $\pm\infty$ (convergence being guaranteed by the finite fourth-order terms). Then, the amplitudes \mathcal{A} (33) can be expressed through integral representations of the Bessel functions $J_{\pm 1/4}(x)$:

$$\mathcal{A}(\xi) = \frac{\pi}{2}\sqrt{\xi} \left\{ \exp\left[-i\left(\frac{\xi^2}{8} - \frac{\pi}{8}\right)\right] J_{-1/4}\left(\frac{\xi^2}{8}\right) - \frac{\xi}{|\xi|} \exp\left[-i\left(\xi + \frac{\pi}{8}\right)\right] J_{1/4}\left(\frac{\xi^2}{8}\right) \right\}. \quad (39)$$

Here we took into account a time-reversal symmetry by inclusion of the factor 2 where necessary. Note that more exact trace formulae (with additional terms proportional to Bessel functions with indices $\pm 3/4$ etc.) can be derived by taking into account higher-order terms in the phase and amplitude factors, respectively. This gives results similar to those obtained in [77] using the normal forms for pitchfork bifurcations.

Using asymptotic forms of the Bessel functions for large arguments ξ in (39), one obtains from (32) (with $\phi = 0$) the standard Gutzwiller trace formula [1, 7] valid for isolated POs:

$$\delta g_{\text{scl}}(E) \rightarrow \sum_{\text{PO}} A_{\text{PO}}^{\text{G}}(E) \cos\left[\frac{S_{\text{PO}}(E)}{\hbar} - \frac{i\pi}{2}\sigma_{\text{PO}}\right], \quad (40)$$

$$A_{\text{PO}}^{\text{G}}(E) = T_{\text{PO}} \left(\pi \hbar \sqrt{|2 - \text{Tr } \mathcal{M}_{\text{PO}}|} \right)^{-1},$$

where \mathcal{M}_{PO} is the stability matrix for the PO (Appendix A7). Numerical and analytical calculations and the remarkable “fan” structure of the pitchfork bifurcations

of the straight-line orbits A_σ were analyzed in the case of the HH potential [81, 85, 93]. Several analytical approximations for $\text{Tr } M_A$ can be derived in terms of the simplest Mathieu functions for smaller energies $e \lesssim 0.8$, and in terms of the improved Legendre solutions for the whole region from the zero energy to the saddle, $0 \leq e \leq 1$, in good agreement with the numerical results [71, 81].

The trace formula (32) also has the correct harmonic-oscillator (HO) limit for $E \rightarrow 0$, where $\text{Tr } \mathcal{M}_{\text{PO}} \rightarrow 2$, and all coefficients in the expansion of the action phase in Q and p go to zero (and $\int dQ dp \rightarrow 2\pi E$). The Poincaré variables Q and p become cyclic in this HO limit. In the spirit of the uniform approximations ([7] and [88]) within the ISPM, we may use a canonical transformation from the variables (Q, p) to new variables (\tilde{Q}, \tilde{p}) in which one has a simple analytical expression for the PO amplitude

$$A_{\text{PO}}^{\text{G}} [1 - \exp(-E/A_{\text{PO}}^{\text{G}})] , \quad (41)$$

instead of A_{PO}^{G} in (40), with the two correct limits to the HO trace formula [7] for $E \rightarrow 0$ and to the Gutzwiller trace formula (40) for large E . We should note that this procedure is not unique, see [71]. On the other hand, within the ISPM, we use as “normal forms” equation (30) for the generating function with expansion (31) near the stationary points rather than near the bifurcations. A similarity to the normal form theory is manifested if we put formally $Q^* = 0$, $p^* = 0$ in (31) in the system of coordinates related to the bifurcation point reducing the non-local ISPM to its local approximation valid nearly the bifurcation points. Moreover, from a more pragmatic point of view, the details of the required canonical transformation do not matter for the SPM approximation in narrow regions of phase space around the critical points: The limit $\hbar \rightarrow 0$ in practice corresponds to large particle numbers N through the Fermi energy E_F at a rather small parameter α and larger averaging width γ of the gross shell structure. We emphasize also a chaos-to-order transition of the PSS in the limit to the symmetry breaking point $e \rightarrow 0$ (Fig. 1). In this limit, the isolated trajectories are transformed into the degenerate PO families.

Expressions found from (32) locally for the separate bifurcations of the rotating (R) or librating (L) orbits are in agreement with the results [75, 77, 78] obtained using the standard normal forms for the pitchfork bifurcations. However, for the full cascade of bifurcations near the saddle energy of the HH potential, our result (32) goes beyond the normal-form theory. It is a continuous function through all bifurcation points near the saddle energy and also down to the limit to the symmetry-breaking point at $E = 0$. The coefficients $\epsilon(E)$ and $a(E)$ in (33) are also continuous functions of the energy E through all stationary points (POs). Note also that our ISPM expression (32) for the shell correction to the level density is a sum of separate contributions of all involved POs, and a coarse-graining over the energy E (cf. below) may therefore be performed analytically. Thus, one has a possibility to study analytically both gross and fine shell structures. This is in contrast to the results [82, 88] using uniform approximations based on the normal-form the-

ory [75, 77, 78], where at each critical point all involved POs give one common contribution.

2. Discussion of results

For the purpose of studying the improved level density around the bifurcation points, we consider a slightly averaged level density, thus avoiding the convergence problems that usually arise when one is interested in a full semiclassical quantization. Such a “coarse-graining” can be done by folding the level density over a Gaussian of width γ [7, 8]. (The particular choice of a Gaussian form of the averaging function is immaterial and guided only by mathematical simplicity.) Applying this procedure to the semiclassical level density (32), one obtains (16) for the averaged level-density shell correction $\delta g_{\Gamma, scl}(E)$ [3, 7, 8].

The averaging of the oscillating level density yields an exponential decrease of the amplitudes with increasing periods t_{PO} and/or Γ . As shown in [69], for γ about $1/3$ (in $\hbar\omega$ units), all large-action paths are strongly damped and only the time-shortest POs contribute to the oscillating part of the level density, yielding its gross-shell structure. For a study of the bifurcation phenomenon, however, we need smaller values of γ . In Fig. 3 we used the coarse-grained Gutzwiller trace formula (16) with (40) including the simplest primitive orbits $A, B = L_4$ and $C = R_3$.

It is interesting that the gross-shell structure manifests itself for the HH parameter $\alpha = 0.04$ even for a relatively small averaging parameter $\gamma = 0.25\hbar\omega$. Therefore, we should expect also a good agreement between semiclassical and quantum results for the shell-correction energy δU as function of the particle numbers $N^{1/2}$ for the same $\alpha = 0.04$ for larger energies (but still far enough from the bifurcation points, cf. Fig. 4).

The shell-correction energy δU , i.e., the oscillating part of the total energy U of a system of N fermions occupying the lowest quantum levels in a given potential, can be expressed in terms of the oscillating components $\delta g_{PO}(E)$ at the Fermi energy $E = E_F$ of the semiclassical level density (32) and (9), as in [3, 5, 7, 8], see also (18) for the shell-correction energy δU . We are taking into account the spin degeneracy factor 2 in (18). The semiclassical representation of the shell-correction energy (18) differs from that of $\delta g_{scl}(E)$ (14) (at $E = E_F$) only by a factor $(\hbar/t_{PO})^2$ under the sum, which suppresses contributions from orbits of larger time periods (actions). Thus the periodic orbits with smaller periods play a dominant role in determining the shell-correction energy [3, 5]. Finally, we should note that the higher the degeneracy of an orbit, the larger the volume occupied by the orbit family in the phase space, and also the smaller its time period (action), the more important is its contribution to the shell-correction energy (18).

Fig. 3 and 4 show a good agreement between the semiclassical and quantum results, in spite of using only the three shortest orbits A , L_4 (B), and R_3 (C). These are seen to yield the correct gross-shell structure for the parameter $\alpha = 0.04$ (and widths for the Gaussian aver-

aging of the level density shell corrections $\gamma = 0.25\hbar\omega$ or, similarly, for $\gamma = 0.6\hbar\omega$) in the energy region below the saddle ($E = E_{barr}$) and above the bottom ($E = 0$). The discrepancies at smaller energies are related to the symmetry breaking at $E = 0$, as discussed above, and will be removed when using our full ISPM trace formula (32). In the quantum-mechanical determination of δU (see [7, 10] for discussions of the Strutinsky averaging method), the plateau condition for the averaged energy was satisfied for a Gaussian width $\tilde{\gamma} \simeq 1.75\hbar\omega$ and a curvature correction parameter $M = 6$.

III. FISSION-CAVITY MODEL AND SHAPE ISOMERS

In this section, we shall present some applications of the POT to nuclear deformation energies and discuss in more detail the relation of the bifurcations of periodic orbits with the pronounced shell effects and fission isomers.

According to the SCM, the oscillating part of the total energy of a finite fermion system, the shell-correction energy δU , is associated with an inhomogeneity of the s.p. energy levels near the Fermi surface. Its existence in dense fermion systems is a basic point of Landau’s quasi-particle theory of infinite Fermi liquids, as extended to self-consistent finite fermion systems by Migdal and collaborators [13, 14]. Depending on the level density at the Fermi energy – and with it the shell-correction energy δU – being a maximum or a minimum, the nucleus is particularly unstable or stable in the case of dense and sparse s.p. spectra, respectively. This situation varies with particle numbers and deformations of the nucleus. In consequence, the shapes of stable nuclei depend strongly on the particle numbers and deformations. This is illustrated in [5, 7]. The shell correction δU of neutrons is shown as a function of the neutron number N and the deformation parameter η of a Woods-Saxon potential with spheroidal shape, η being the ratio of the semi-axes. If we fix the neutron number N , e.g. $N = 150$, and increase the deformation η , we meet the first minimum (ground state) at about $\eta \sim 1.25$ and the next one (isomeric state) at much larger deformations $\eta \sim 1.9 - 2.1$. The experimental data corresponding to these deformations are in good agreement with the semiclassical slopes.

The SCM was successfully used to describe nuclear masses and deformation energies and, in particular, fission barriers of heavy nuclei, see an early review by Strutinsky’s group [10], in which also the microscopic foundations of the SCM are discussed. As shown in [5], the predictions of the POT for a loci of the ground-state minima, using the shortest POs in a spheroidal cavity are basically in agreement with experimental data. Bifurcations of POs under the variation of a deformation parameter or the (Fermi) energy can have noticeable effects for the shell structure [5, 61, 62, 69, 70]. In this section, we review the semiclassical description (see also [60]) of a typical nuclear fission barrier in terms of the shortest periodic orbits, employing a cavity model with the realistic shape parametrization developed in [10]. In particular, the effect of the left-right asymmetric defor-

mations on a height of the outer fission barrier will be discussed. Isochronous bifurcations of the shortest orbits are treated in [60] by using the uniform approximation employing a suitable normal form for the action function. The relation of the bifurcations of POs to the foundation of the local second minima at large isomer deformations will be discussed for the cavity model with the realistic parametrization [10].

One prominent feature in the fission of actinide nuclei (isotopes of U, Pu, etc.) is that their fragment distributions are asymmetric with a most probable ratio of fragment masses of $\sim 1.3 - 1.5$ (cf. [10]). This is an effect that cannot be described within the LDM which always favors the highest possible symmetries. It was one of the big successes of the SCM to explain the mass asymmetry of fission fragments. The fragment distribution is, of course, a result of nuclear dynamics. However, already in static calculations of fission barriers, the onset of the mass (or left-right) asymmetry at an outer fission barrier was found in SCM calculations with realistic nuclear shell models. On the l.h.s. of Fig. 5, we show a schematic picture of the deformation energy of a typical actinide nucleus, as plotted versus suitably a chosen deformation parameter (see below for a specific choice of deformations). The heavy dashed line is the average deformation energy obtained in the LDM; the thin lines are the results obtained when the shell-correction energy δU is included. They exhibit the characteristic deformation effects of the shell structure in these nuclei: a deformed ground state and the characteristic double-humped fission barrier, split by a second minimum corresponding to the fission isomer. The solid line is obtained when only the left-right symmetric deformations are used; the dashed thin line is obtained when one allows for the left-right asymmetric shapes. As we see, the asymmetric shapes are displayed considerably lower the outer fission barrier. All shapes here are taken to be axially symmetric.

The mass asymmetry in nuclear fission was therefore understood as a quantum shell effect. In a detailed microscopical study [94] of the Lund group using the Nilsen model, it was shown that those s.p. states which are most sensitive to the left-right asymmetric deformations are pairs of states with opposite parity, having the nodes and extrema of their wave functions on parallel planes perpendicular to the symmetry axis at and near the waist-line of the fissioning nucleus, as shown on the r.h.s. of Fig. 5. Under the effect of the neck constriction one of these s.p. levels, which for actinides is just lying below the Fermi energy, is further lowered when the mass asymmetry is turned on. As a consequence, the asymmetry leads to a lowering of the total shell-correction energy, and hence of the outer fission barrier, the LDM part of the energy being much less sensitive to the mass asymmetry.

In this section, we want to show that the POT is able to reproduce this quantum shell effect, at least qualitatively, in the semiclassical description using the POT. We will focus here only on the gross-shell structure, like that seen in the qualitative picture of a fission barrier in Fig. 5.

The spheroidal cavity model used in [5] and discussed

in [5, 8, 62] allows one to describe only qualitatively a nuclear fission, since an ellipsoidal deformation is not sufficient to yield a finite barrier towards fission. In [8, 60], a simple but more realistic “fission cavity model” was used. It consists of a cavity with the (c, h, α) shape parametrization that was used both for the LDM and for the deformed Woods-Saxon type shell-model potentials in the SCM calculations of [10]. These axially symmetric shapes are shown in Fig. 6. The parameter c describes the elongation of the nucleus (in units of the radius R_0 of a sphere containing $N = \rho_0 4\pi R_0^3/3$ particles, where ρ_0 is the bulk particle density), h is a necking parameter, and $\alpha \neq 0$ describes the left-right asymmetric shapes shown by the dotted lines. The sequence of shapes with $h = \alpha = 0$ reproduces the optimized shapes of the LDM [11, 95] (see [10] for details). As in [5], the spin-orbit and pairing interactions were neglected in [8, 60] and, for simplicity, only one kind of nucleons (without Coulomb interaction) was used. The only parameter in the fission cavity model, the Fermi wave number $k_F = 12.1/R_0$, was adjusted to yield the second minimum at the deformation $h = \alpha = 0$, $c = 1.42$ which is that of the fission isomer obtained in [10] for the nucleus ^{240}Pu . This corresponds here to a particle number $N \simeq 180$, i.e., to $N^{1/3} \simeq 5.65$ when the spin-orbit interaction is neglected.

This procedure is justified by the observation that, to a first approximation, the spin-orbit and Coulomb interactions essentially lead to a shift of the magic numbers, preserving the relative shell structures in the energy shell-correction. This shift can be simulated by a shift of the Fermi energy as in [5]. The procedure works, however, only locally in a limited region of deformations and particle numbers. The results shown below suggest that it is successful in the region $1.3 \lesssim c \lesssim 1.65$; the ground-state deformations would, e.g., not be reproduced correctly with the same Fermi energy. [Note that, in principle, spin-orbit effects can be included in the POT, see [8] and references cited therein. However, in non-integrable systems one is met with lots of bifurcations under the variation of the spin-orbit strength, which makes the POT with spin-orbit interactions very cumbersome. Similarly, the pairing interactions can also be included in the POT, but this has not been done for the nuclear-deformation energies so far.]

In [60], the shortest POs in the (c, h, α) cavity were found to dominate the gross-shell features of the double-humped fission barrier. For the deformations around the barriers ($c \gtrsim 1.3$), the shortest POs are the primitive diagonal and regular polygonal orbits in planes perpendicular to the nuclear symmetry axis, situated at the extrema of the cavity shape function (seen in Fig. 6). At the onset of the neck ($c = 1.49$ for $h = \alpha = 0$), the orbits in the central equatorial plane become unstable with respect to small perturbations perpendicular to the equatorial plane and give birth to new stable orbits lying in planes parallel to the equatorial plane. In the restricted deformation space with $\alpha = 0$, these bifurcations are of pitchfork type; they are isochronous from the reflection symmetry with respect to the equatorial plane. When the asymmetry $\alpha \neq 0$ is turned on in the presence of a neck, the bifurcation is of a more complicated type. These bifurcations were treated in the uniform approxi-

mation employing a suitable normal form for the action function [60]. (Note that with respect to small perturbations within the equatorial plane, all these orbits are marginally stable, forming degenerate families with the degeneracy $\mathcal{K} = 1$ due to the axial symmetry of the cavity.) Before summarizing the results of [60], let us study the general trends of the shell effects obtained in the fission cavity model and try to understand them in terms of the leading POs.

In Fig. 7 we show a contour plot of the quantum-mechanical shell-correction energy δU calculated from the s.p. energy spectrum of the fission cavity model, shown versus the cube-root of the particle number $N^{1/3}$ and the elongation parameter c along $h = \alpha = 0$ (white: positive values, gray to black: negative values, see [8]). The horizontal dotted line for $N \simeq 180$ (i.e., $k_F = 12.1/R_0$) corresponds to the situation where the isomer minimum lies at $c \simeq 1.4$ and the outer (symmetric) barrier is peaked around $c \simeq 1.55$, as shown explicitly below. The heavy lines give the loci of constant actions of the leading POs (3,1,1)s: meridian triangles (triangle orbits in the meridian plane, i.e., the plane containing the symmetry z axis); (2,1)EQ: equatorial diameters; (2,1)AQ: diameter orbits in planes parallel to the equator plane. As seen, these lines follow the valleys of the minimal shell-correction energy. As shown in Section II, these periodic orbits are dominating in the PO expansion (18) of the shell-correction energy δU . Assuming that a certain PO yields the dominant contribution into the PO sum (18), one can approximate the shell-correction energy by its main term:

$$\begin{aligned} \delta U_{\text{scl}}(N, c) &\approx 2 \left(\frac{\hbar}{t_{\text{PO}}(E_F)} \right)^2 \delta g_{\text{PO}}(E_F, c) = \\ &= 2 \left(\frac{\hbar}{t_{\text{PO}}(E_F)} \right)^2 A_{\text{PO}} \cos \left[\frac{1}{\hbar} S_{\text{PO}}(E_F, c) - \frac{\pi}{2} \mu_{\text{PO}} \right] \\ &\quad \text{with } E_F = E_F(N). \end{aligned} \quad (42)$$

Then, the minima of the shell-correction energy should be distributed along the lines where the phase takes the values $(2n + 1)\pi$ with an integer n . These conditions satisfying along the constant-action lines in the particle number-deformation, N - c , plane take the form as a generalized multi-dimensional quantization rule [3],

$$S_{\text{PO}}(E_F, c) = 2\pi\hbar \left(n + \frac{1}{2} + \frac{\mu_{\text{PO}}}{4} \right), \quad (43)$$

$$n = 0, 1, 2, \dots$$

For the valleys corresponding to the ground-state deformations, the situation is like in [5] obtained for the spheroidal models, but here for the more realistic fission-cavity model; in all cases the meridian orbits dominate the ground-state valleys. The valleys corresponding to the fission isomers, are starting around $c \sim 1.3$. They are determined by the shortest POs in planes perpendicular to the symmetry axis: up to $c \sim 1.5$, these are the equatorial orbits EQ; after their bifurcation at $c = 1.49$, the valleys are seen to curve down towards smaller values of $N^{1/3}$, following the constant-action lines of the stable POs in planes parallel to the equator plane (dashed lines, AQ). The bifurcating AQ POs have larger semiclassical amplitudes than the equatorial orbits (EQ) that

for $c > 1.49$ have become unstable. The fact that the quantum-mechanically obtained stability valleys follow the (dashed) lines AQ after their branching from the lines EQ is a remarkable quantum signature of the classical bifurcation effect as the level-density amplitude enhancement (Section IIB).

The most striking feature of the gross-shell structure (Fig. 7), namely the opposite slopes of the ground-state valleys ($1 \lesssim c \lesssim 1.25$) and the isomer valleys ($c \gtrsim 1.3$), are thus understood semiclassically in terms of the opposite deformation dependence of the dominating meridian POs in the former valleys and the POs in planes perpendicular to the symmetry axis in the latter valleys, respectively.

These results can be further elucidated by looking at the Fourier spectra in Fig. 8 for the five values (from top to bottom) $c = 1.1, 1.2, 1.4, 1.5$, and 1.6 (all for symmetric shapes with $h = \alpha = 0$). The short arrows underneath the Fourier peaks indicate the lengths of the equatorial orbits: diameter (2,1)EQ and its second repetition 2(2,1)EQ, triangle (3,1)EQ, etc., and (for $c = 1.6$) the corresponding orbits AQ in the planes parallel to the equator plane. The long arrows correspond to the meridian orbits: triangle (3,1,1)s and quadrangle (4,1,1)s. For small deformations $c = 1.1$ and 1.2 , the meridian orbits have the strongest amplitudes, and hence, dominate the shell structure in yielding the ground-state deformation valleys (Fig. 7). The equatorial orbits EQ and their bifurcated partners AQ have the largest amplitudes for $c = 1.4 - 1.6$, which explains their dominance in yielding the isomer valleys.

As we discussed in Section IID, the factor $(\hbar/t_{\text{PO}})^2$ in the trace formula (18) brings about a natural suppression of longer orbits contributing to δU . This ensures the convergence of the PO sum, particularly in non-integrable systems (like the one considered here) where the PO sum for the level density (9) usually does not converge [1]. This suppression is particularly effective amongst orbits with comparable amplitudes A_{PO} . It explains why already at $c = 1.4$, where the meridian orbits (3,1,1)s and (4,1,1)s still have similar amplitudes as the EQ orbits,³ the latter dominate the shell structure (by a factor ~ 4 in the case of the EQ2 orbit), as suggested by Fig. 7.

In Fig. 8 we have marked some of the peaks around $7 \lesssim L \lesssim 8.5$ for $c = 1.4$ and around $6.5 \lesssim L \lesssim 8$ for $c = 1.5$ and 1.6 . They correspond to orbits born from the equatorial orbits in the period-doubling bifurcations (similar as discussed for the spheroidal cavity in [8, 62]); some of them are 3-dimensional orbits. Similarly, there are many other peaks at $L \gtrsim 8$, some of which correspond to orbits born in the high m -tupling ($m \geq 3$) bifurcations. The contributions of all these orbits to the gross-shell structure is, however, practically negligible due to their long periods. They have therefore

³ The strong Fourier peak near $L/R_0 \sim 6.3$ for $c = 1.4$ in Fig. 8 contains the combined amplitudes of the meridian quadrangle (4,1,1)s and the second repetition of the equatorial diameter orbit, 2(2,1)EQ. Although the two cannot be disentangled, we estimate that both these orbits have comparable amplitudes (Section II).

not been included in the results presented below. They might, however, become noticeable in POT calculations with higher resolution of the shell structure.

We should also recall the fact that in realistic SCM calculations, the pairing interactions are known to reduce the amplitude of δU by up to $\sim 30\%$ (see, e.g., [10]). In the POT, the pairing effects yield, indeed, an extra smoothing factor in the semiclassical amplitudes, which further suppresses the contributions of longer orbits [8].

Let us now look at the influence of the left-right asymmetric shapes with $\alpha \neq 0$ on the shell-correction energy and, in particular, on the height of the second fission barrier. In Fig. 9, the semiclassical result of δU is shown in a perspective view as a function of the elongation c and left-right asymmetry α , taken along $h = 0$ in the region of the isomer minimum and the outer fission barrier in [60], see also [8]. We see how the outer fission barrier is lowered for the left-right asymmetric shapes. Instead of the higher barrier obtained for these shapes with $\alpha = 0$ (arrow labeled “*symm.*”), the nucleus can go towards fission over a lower saddle when asymmetric shapes are allowed (arrow labeled “*asymm.*”). To the left, we see the shapes corresponding to the three points A (fission isomer), B and C (along the asymmetric fission path) in the deformation energy surface. The vertical lines indicate the planes in which the POs are situated (solid lines for stable and dashed line for unstable POs).

The instability of the outer fission barrier towards the left-right asymmetric deformations, known from the quantum-mechanical SCM calculations, can thus be described semiclassically using the POT, indeed [8]. Hereby only the shortest primitive POs are relevant from the fast convergence of the PO sum for the semiclassical shell-correction energy δU , as discussed above.

The old quantum-mechanical results of SCM calculations [10] with some realistic deformed Woods-Saxon potentials are compared to the semiclassical POT results using the present simple fission-cavity model. Shown are contour plots of δU versus c and α for two values of the neck parameter h . The semiclassical results (r.h.s.) reproduce the gross-shell structure of the quantum results (l.h.s.) very well (Fig. 10). The correct topology is obtained, displaying the lowering of the outer barrier for several left-right asymmetric shapes. Also, the amplitudes of the shell effects on both sides are comparable, which justifies our calculations of only the gross-shell structure by using the shortest periods on a semiclassical level. Of course, a detailed quantitative agreement cannot be expected for the two calculations using such different potentials as the sophisticated smooth Woods-Saxon potential including pairing, spin-orbit, and Coulomb interactions on one side (left), and the simple fission-cavity model without these extra interactions on the other side (right). The more gratifying is the overall good qualitative agreement of the gross-shell structure. This agreement demonstrates, by the way, an experience made from the quantum-mechanical SCM calculations using a realistic nuclear shell-model potential: The gross-shell features of the fission barriers are much less sensitive to the radial dependence of the potential than to its deformation. Hence, the success of a simple cavity model that is very schematic, but uses the realistic c, h, α deforma-

tions.

The white dashed lines in the r.h.s. panels of Fig. 10 shows the loci of constant classical actions S_{PO} of the leading POs. They follow exactly the valleys of minimal energy in the (c, α) planes which define the adiabatic fission paths. Thus, as it was already observed in [5] and seen in Fig. 7, the condition for minimizing the shell-correction energy is semiclassically given by a least-action principle: $\delta S_{PO} = 0$.

We should emphasize that in Figs. 9 and 10 only the shell-correction energy δU is shown. The complete fission barrier is obtained by adding its smooth LDM part (within the SCM) which for ^{240}Pu in the (c, h, α) parametrization occurs [10] at $c \simeq 1.45 - 1.5$, $h = \alpha = 0$. Since the LDM barrier is rather smooth around its maximum, the relative heights of the isomer minimum and the outer barrier are not affected much by it. However, for $c \gtrsim 1.6$ the LDM barrier is already going steeply down. Therefore, in the total energy, the minimum around $c \simeq 1.65 - 1.7$ (Figs. 9 and 10) along $h = 0 = \alpha = 0$ vanishes in the steep slope of the total fission barrier, as shown schematically in Fig. 5.

It is also interesting to note that the quantum-mechanical probability maxima of those s.p. states which microscopically are responsible for the asymmetry effect in the SCM approach (see the schematic plot on the r.h.s. of Fig. 5) lie exactly in the planes perpendicular to the symmetry axis that contain the classical POs. This constitutes a nice quantum-to-classical relationship. The classical dynamics of the nucleons with small angular momenta L_z is more than 90% chaotic in the region of the outer barrier [8]. A very small phase-space region of regular motion is thus sufficient to create the shell effect that leads towards the asymmetric fission of the nucleus.

We emphasize once more that the fission cavity model, in its present form without spin-orbit and Coulomb interactions, is not suitable for predicting fission barriers for a larger range of nuclear isotopes and deformations. The present semiclassical calculation should be taken as a model study of a typical actinide fission barrier, demonstrating that the POT in principle is capable of explaining the existence of a double-humped barrier, and also the onset of mass asymmetry around the outer barrier, in terms of a few short classical POs. It was in no way meant as a substitute for the quantum-mechanical SCM calculations of static-fission barriers. Its aim was rather to provide, as suggested by the late Strutinsky, a qualitative physical understanding of a sophisticated quantum shell effect by means of simple classical pictures.

IV. RADIAL POWER-LAW POTENTIALS

This Section is devoted to the analytical POT derivations for the radial power-law potential (RPLP). The main scaling properties and classical dynamics in the RPLP will be dealt with in Section IVA. The trace formulae for different PO families in this Hamiltonian will be derived (Sections IVB-IVD). In Section IVE, they will be summarized in terms of the total POT sums for the level-density and energy shell corrections, and the Fourier transforms of the quantum level densities and

their relation to the level-density amplitudes for different POs will be obtained. The semiclassical POT and quantum-mechanical results for the RPLP will be compared in Section IVF.

A. Scaling and classical dynamics

The idea of [84, 86] is that the spherical WS potential, known as a realistic mean-field potential model for spherical nuclei and metallic clusters, is nicely approximated (up to a constant shift and without the spin-orbit term) by a significantly simpler RPLP which is proportional to a power of the radial coordinate r^α ,⁴

$$V(r) = V_0(r/R)^\alpha. \quad (44)$$

With a suitable choice of the parameters V_0 and α , for the realistic WS potential $V_{WS}(r)$ the approximate equality,

$$V_{WS}(r) \approx V_{WS}(0) + V_0(r/R)^\alpha, \quad (45)$$

holds up to $r \lesssim R$, where $V_{WS}(0)$ is a WS depth constant. The mean nuclear radius R for a definite mass number N is given by $R = r_0 N^{1/3}$ with $r_0 \approx 1.2$ fm. Thus, one finds a nice agreement of the quantum spectra for the approximation (45) to the WS potential up to and around the Fermi energy E_F .

In the RPLP well (44) [or (45)], there are the obvious two-parametric ($\mathcal{K} = 2$) diameter families, and the specific $\mathcal{K} = 2$ family of circle orbits at edges $L = 0$ and L_C of the energy surface $I_r = I_r(E, L)$ as for any spherical potentials, respectively, see Section IIE and Appendix A1. Again, in a fixed plane crossing the center with radius $r = r_{min} = r_{max} = r_c$, one has the isolated circle periodic orbit. The first equation in (25) determines the turning points $r_{min}(L)$ and $r_{max}(L)$ as functions of L at the fixed energy E , and their cross gives the specific $L = L_C = p(r_C)r_C$. As mentioned in Section IIE2, according to the expression for the radial momentum p_r from (22) which must be real, the maximal angular momentum L is namely this L_C which is related to the zero p_r , and the zero minimal value of the angular momentum L ($0 \leq L \leq L_C$). As for general spherical potentials (Section IIE), the maximal value of the angular momentum $L = L_C$ is related to a circular orbit and the minimal one $L = 0$ corresponds to a diameter. The critical values $r = r_C$ and $L = L_C$ are determined as the solution of system of the two equations (27) with respect to r and L [$d^2 p_r^2(r, L)/dr^2 \neq 0$], as assumed to be the case for the r^α model. The first equation claims that there is no radial velocity, $\dot{r} = 0$, and the next equation is that the radial force is equilibrated by the centrifugal force. For instance, for the potential (45) the solution of the two equations (27) is given by [84, 86, 87],

$$r_C = R \left(\frac{2E}{(2+\alpha)V_0} \right)^{1/\alpha}, \quad L_C = p(r_C)r_C. \quad (46)$$

Another key quantity in the RPLP POT is the curvature K of the energy surface $I_r = I_r(E, L)$, (28).

Using the scale invariance valid for the RPLP,

$$\begin{aligned} \mathbf{r} &\rightarrow s^{1/\alpha} \mathbf{r}, \quad \mathbf{p} \rightarrow s^{1/2} \mathbf{p}, \\ t &\rightarrow s^{1/2-1/\alpha} t \quad \text{for } E \rightarrow sE, \end{aligned} \quad (47)$$

one may factorize the action integral $S_{PO}(E)$ along the PO as

$$\begin{aligned} S_{PO}(E) &= \oint_{PO(E)} \mathbf{p} \cdot d\mathbf{r} = \\ &= \left(\frac{E}{V_0} \right)^{\frac{1}{2} + \frac{1}{\alpha}} \oint_{PO(E=V_0)} \mathbf{p} \cdot d\mathbf{r} \equiv \\ &\equiv \hbar \mathcal{E} \tau_{PO}. \end{aligned} \quad (48)$$

In the last equation, we define the dimensionless variables \mathcal{E} and τ_{PO} , which we call *scaled energy* and *scaled period*, respectively;

$$\begin{aligned} \mathcal{E} &= (E/V_0)^{\frac{1}{2} + \frac{1}{\alpha}}, \\ \tau_{PO} &= \frac{1}{\hbar} \oint_{PO(E=V_0)} \mathbf{p} \cdot d\mathbf{r}, \end{aligned} \quad (49)$$

as classical characteristics of the particle motion. To realize the advantage of the scaling invariance (47), it is helpful to use \mathcal{E} and τ_{PO} in place of the energy E and the period t_{PO} , respectively. In the HO limit ($\alpha \rightarrow 2$), \mathcal{E} and τ_{PO} are proportional to E and t_{PO} ; while in the cavity limit ($\alpha \rightarrow \infty$), they are proportional to the momentum p and length \mathcal{L}_{PO} , respectively.

The PO (resonance) condition (26) determines several PO families in the RPLP well, namely the polygonal-like ($\mathcal{K} = 3$), the circular and diametric ($\mathcal{K} = 2$) POs. Fig. 11 shows these POs in the RPLP (44) in the $\{\tau, \alpha\}$ plane, where $\tau(\alpha, L)$ is the scaled period and $\tau_{PO} = \tau(\alpha, L_{PO})$ at the angular momentum $L = L_{PO} = |\mathbf{r} \times \mathbf{p}|_{PO}$. It is clearly seen from this Figure that at $\alpha \geq \alpha_{bif}$ the polygonal-like orbit $M(n_r, n_\theta)$ appears, and exists, after the bifurcations, from the parent circle orbit MC (M -th repetition of the primitive circle orbit C). The diameter orbits $M(2,1)$ are exclusion because their birth arise exactly at the harmonic oscillator (HO) symmetry-breaking point $\alpha = 2$ and exist for all larger values, $\alpha > 2$.

B. Three-parametric PO families

1. ISPM derivations of the trace formula

For the contribution of the three-parametric ($\mathcal{K} = 3$) families into the trace formula (20) for the shell correction, after the exact integration over L_z , having $2L$; and φ , 2π , for $\mathcal{D} = 3$ one obtains

$$\begin{aligned} \delta g_{scl}(E) &= \frac{4\pi}{(2\pi\hbar)^3} \text{Re} \sum_{CT} \int d\theta'' d\Theta_r'' dI_r \times \\ &\times \int dL L \delta(E - H(I_r, L)) |\mathcal{J}_{CT}(\mathbf{p}_\perp'', \mathbf{p}_\perp')|^{1/2} \times \\ &\times \exp\left(\frac{i}{\hbar} \Phi_{CT} - \frac{i\pi}{2} \mu_{CT}\right). \end{aligned} \quad (50)$$

Taking the integral over I_r exactly by using the δ -function which ensures the energy conservation, one has

$$\begin{aligned} \delta g_{scl}(E) &= \frac{4\pi}{(2\pi\hbar)^3} \text{Re} \sum_{CT} \int d\theta'' \frac{d\Theta_r''}{\omega_r} dL L \times \\ &\times |\mathcal{J}_{CT}(\mathbf{p}_\perp'', \mathbf{p}_\perp')|^{1/2} \exp\left(\frac{i}{\hbar} \Phi_{CT} - \frac{i\pi}{2} \mu_{CT}\right). \end{aligned} \quad (51)$$

⁴ In the following, the parameter α is used for the power parameter and should not be confused with that for reflection-asymmetry in the previous section.

Then, we integrate over the angle variable Θ_r'' accounting for independence of the integrand, in particular, of the action phase Φ_{CT} , on any variations of this angle. With the corresponding time variable, $d\Theta_r''/\omega_r = dt$, along the POs, one finds

$$\int_0^{2\pi} \frac{d\Theta_r''}{|\omega_r|} = \int_0^{T_{r\text{CT}}} dt = T_{r\text{CT}}, \quad (52)$$

where $T_{r\text{CT}}$ is the time duration for a primitive (without repetitions) particle motion along the CT, one obtains

$$\delta g_{\text{scl}}(E) = \frac{4\pi}{(2\pi\hbar)^3} \text{Re} \sum_{\text{CT}} \int d\theta'' dL L T_{r\text{CT}} \times \quad (53)$$

$$\times |\mathcal{J}_{\text{CT}}(\mathbf{p}'_\perp, \mathbf{p}'_\perp)|^{1/2} \exp\left(\frac{i}{\hbar} \Phi_{\text{CT}} - \frac{i\pi}{2} \mu_{\text{CT}}\right).$$

All quantities in the integrand are taken at the energy surface $I_r = I_r(E, L)$, defined by (24).

Applying the SPM conditions (Sections IIA and IIE [69]) for the perpendicular angle θ' , one notes that there is the continuum of the stationary points $\theta'' = \theta''^* = \theta^*$ within $0 \leq \theta^* \leq 2\pi$ as solutions of the SPM equations [69]. Therefore, the phase Φ_{CT} in exponent does not depend on this angle,

$$\Phi_{\text{CT}} = 2\pi [M_r I_r(E, L) + M_\theta L], \quad (54)$$

where M_r, M_θ are integers, $M_r = Mn_r$, $M_\theta = Mn_\theta$, n_r and n_θ are the *positive* co-primitive integers, M is nonzero integer. So, writing exactly 2π for the integral over θ'' in (53), one obtains the semiclassical Poisson summation trace formula which can be derived alternatively from the quantum Poisson summation trace formula by using the EBK quantization rules [4] for the case of the spherical symmetry of the Hamiltonian,

$$g_{\text{scl}}(E) = \frac{2}{\hbar^3} \text{Re} \sum_{M, n_r, n_\theta} \int dL \frac{L}{\omega_r} \times \quad (55)$$

$$\times \exp\left\{\frac{2\pi i}{\hbar} M [n_r I_r(E, L) + n_\theta L] - \frac{i\pi}{2} \mu_{M, n_r, n_\theta}\right\},$$

Formally, before taking the trace integral over the angular momentum L by the SPM in (55), one can consider positive and negative M as related to the two opposite directions of motion along a classical trajectory CT. This yields the equivalent contributions into the trace formula due to a time-reversibility invariance of the Hamiltonian. Therefore, we may write simply the additional factor 2 in (55) but with replacing the summation over M by positive integers ($M > 0$).

We emphasize that for $\mathcal{K} = 3$ families the generating function (2) becomes independent of the perpendicular angle variable θ'' for the integrable Hamiltonian, see (54), in contrast to the Hamiltonian $H(I_r, L)$ itself which always does not depend on the angle variables because of integrability of the system [69]. Exceptions are the complete degeneracy as the HO, see below.

The integration range in (55) taken from the minimal, $L = 0$, to the maximal value, $L = L_+$, covers in the integration variable L the contributions of whole manifold of closed and unclosed trajectories of the tori in the phase space around the stationary point L^* , which corresponds to the periodic orbit. The maximal angular momentum L_+ is restricted by the energy conservation for a given

energy E . By the finite limits for contributions of different orbits they are approximately independent, except for some exclusions [69]. Here, in the case of the spherical Hamiltonians such a relationship between the finite limits for different kind of orbits takes place too and will be discussed later in relation to the HO limit $\alpha \rightarrow 2$. In this limit, the sum of the the trace formulas for the two different kinds of families, with the maximal degeneracy $\mathcal{K} = 3$, and smaller for $\mathcal{K} = 2$ circle and diameter orbits, turns into the spherical HO trace formula. They are assumed naturally to be in different parts of the four parametric ($\mathcal{K} = 4$) continuum of the HO periodic-orbit tori in such a symmetry-breaking limit [69]. The latter is an exclusion because of the bifurcation at $\alpha = 2$ where we meet the maximally degenerated spherical HO. We shall specify the integration limits L_+ for the contribution of the $\mathcal{K} = 3$ families into (55) in relation to the corresponding integration limits for the circular orbits and HO limit below.

We apply then the stationary phase condition with respect to the variable L for the exponent phase Φ_{CT} (54) in the integrands of (55),

$$\left(\frac{\partial \Phi_{\text{CT}}}{\partial L}\right)^* = 0, \quad (56)$$

which is exactly the resonance condition (26) [see (54)]. This condition determines the stationary phase point $L = L^*$ related to the POs $M(n_r, n_\theta)$ of $\mathcal{K} = 3$ families. Note that the semiclassical Poisson-summation formula (55) obtained from the quantum Poisson-summation trace formula with further using the EBK quantization [7, 82] contains the sum over integers for M_r from $-\infty$ to $+\infty$ and independently for M_θ from $-\infty$ to $+\infty$, where $M_r = 0, M_\theta = 0$ is related to TF smooth density. For the derivation of the Gutzwiller trace formula for isolated orbits [96] it was important that M_θ/M_r can be also negative and they can take also zero values, except for simultaneous zeros $M_r = 0, M_\theta = 0$ of the TF component. Another assumption is that the end points are not the stationary points, in contrast to our derivations within the extended Gutzwiller approach (EGA).

We expand now the exponent phase Φ_{CT} (54) in the variable L near the stationary point L^* to second order assuming that there is no singularities in the curvature (28) for the contribution of all $\mathcal{K} = 3$ families,

$$\Phi_{\text{CT}} \equiv 2\pi [M_r I_r(E, L) + M_\theta L] \approx \quad (57)$$

$$\approx S_{\text{MP}}(E) + \frac{1}{2} J_{\text{MP}}^{(\text{L})}(L - L^*)^2,$$

where $S_{\text{MP}}(E)$ is the action along the polygon-like PO families specified by the two integers n_θ and $n_r > 2n_\theta$ from the resonance (PO) condition (26) for such a primitive PO, $\mathbf{P} = (n_r, n_\theta)$, and the number of its repetitions M ,

$$S_{\text{MP}}(E) = 2\pi M [n_r I_r(E, L^*) + n_\theta L^*]. \quad (58)$$

In (57) and (58), $L^* = L^*(n_r, n_\theta)$ is the solution of the PO equation (26). The Jacobian $J_{\text{MP}}^{(\text{L})}$ in (57) is the stability of the PO with respect to the variation of the

angular momentum L at the same energy surface,

$$J_{MP}^{(L)} = \left(\frac{\partial^2 S_{CT}}{\partial L^2} \right)_{L=L^*} = 2\pi M n_r K_P, \quad (59)$$

$$K_P = \left(\frac{\partial^2 I_r}{\partial L^2} \right)_{L=L^*},$$

where K_P is the curvature (28) of the energy surface $I_r(E, L)$, see the first equation in (24).

We substitute now the expansion (57) into the last equation of (55) and take there the pre-exponential factor off the integral at $L = L^*$. For the sake of simplicity, we shall discuss the lowest, i.e., second-order expansion of the exponent phase, and the zero-order expansion of the pre-exponent factor with respect to the L variable in (55). Thus, we are left with the integral over L of a Gaussian-type integrand within the finite limits mentioned above for contributions of the three-parametric polygon-like families, including the contribution of the boundaries for $0 < M_\theta/M_r < 1/2$. The integer numbers $M_r = 2M_\theta = 2M$ and $M_r = M_\theta = M$ are related to the diameter and circle POs.

When the stationary point L^* is far away from the physical integration ends, one can extend the integration limits to the infinity region from $-\infty$ to ∞ , and we arrive asymptotically at the Berry&Tabor result of the standard POT extended to continuous symmetries for the contribution of the families ($\mathcal{K} = 3$) [4] as applied to spherical potentials. If the stationary point is close to these ends of the physical tori, one has to use the finite limits, i.e., within the ISPM of second order for the phase expansion, as the simplest approach. For instance, it is the case near $L = L_C$ where $I_r = 0$, and one has bifurcations of the $\mathcal{K} = 3$ polygon-like from the corresponding $\mathcal{K} = 2$ circle family.

Taking the integral over L within the finite limits, we obtain the trace formula in terms of the error functions. Thus, for the ISPM contributions of families of the three-parametric ($\mathcal{K} = 3$) orbits $\delta g^{(3)}(E)$, one obtains

$$\delta g^{(3)}(E) = \sum_{MP} \mathcal{A}_{MP}^{(3)}(E) \times \exp \left[\frac{i}{\hbar} S_{MP}(E) - i \frac{\pi}{2} \mu_{MP} \right]. \quad (60)$$

Here, the sum is taken over the families of the periodic orbits, MP (with accounting for the repetition number M), in the spherical potential, $S_{MP}(E)$ is the action (58) along the PO, $M(n_r, n_\theta)$ (with $n_r > 2n_\theta$). For the amplitude $\mathcal{A}_{MP}^{(3)}$, one finds

$$\mathcal{A}_{MP}^{(3)} = \frac{L_P T_P}{\pi \hbar^{5/2} \sqrt{M n_r K_P}} \operatorname{erf}(\mathcal{Z}_{MP}^+, \mathcal{Z}_{MP}^-) e^{i\pi/4}, \quad (61)$$

where $T_P = T_{n_r, n_\theta}$ is the period of the primitive ($M=1$) periodic orbit P , (n_θ, n_r) , of the three-parametric families for the stationary point $L = L^*$ determined by the PO equation (26),

$$T_P = \frac{2\pi n_r}{\omega_r} = \frac{2\pi n_\theta}{\omega_\theta}, \quad (62)$$

$L_P = L^*$ is the classical angular momentum for the particle motion along a P PO. The function $\operatorname{erf}(v, u)$ in (61)

is expressed through the standard error function of a complex argument,

$$\operatorname{erf}(v, u) = \frac{2}{\sqrt{\pi}} \int_u^v dz e^{-z^2} = \operatorname{erf}(v) - \operatorname{erf}(u), \quad (63)$$

The complex arguments \mathcal{Z}_{MP}^\pm of the error functions in (61) are expressed in terms of the curvature K_P , see (59) at $L = L^*$, through the Jacobian $J_{MP}^{(L)}$ (59) with the explicit stationary points $L^* = L_P$,

$$\mathcal{Z}_{MP}^- = \sqrt{-i\pi M n_r K_P / \hbar} (L_- - L_P), \quad (64)$$

$$\mathcal{Z}_{MP}^+ = \sqrt{-i\pi M n_r K_P / \hbar} (L_+ - L_P).$$

We used here the simplest approximation for the finite integration limits within the tori, minimal $L_- = 0$ and maximal $L_+ = L_C$ values of the angular-momentum integration variable for the $\mathcal{K} = 3$ family contribution. The phase μ_{MP} in (60) is related to the Maslov index as in the asymptotic Berry&Tabor trace formula.

Note that the family amplitude $\mathcal{A}_{MP}^{(3)}$ (61) is continuous in the HO limit where $K_P \rightarrow 0$, due to cancellation of the singularities in the denominator proportional to $\sqrt{K_P}$, with the same coming from the finite limits (64) (see below in this Section for the total trace formula including the circle orbits). There is no singularity also coming from the separatrix (the potential barrier, for instance) where $K_P \rightarrow \infty$. In this limit one has obviously zero limit as for the integrable Hénon-Heiles potential [69].

2. The SSPM limit

In order to get the standard Berry&Tabor trace formula limit we consider the stationary point being inside of the integration interval asymptotically far from the bifurcation points $L = L^* = L_C$. In this case for the contribution of the ($\mathcal{K} = 3$) families (60), one can transform the error functions to the complex Fresnel functions with the real limits. As noted above, in this case one can extend the upper limit to ∞ and the lower one to $-\infty$ far from the bifurcations of a circular orbit. In this way we arrive at the result (60) with the amplitude $\mathcal{A}_{MP}^{(3)}$ of the standard SPM (SSPM) identical to the Berry&Tabor trace formula [4],

$$\mathcal{A}_{MP}^{(3)} = \frac{2 L_P T_P}{\pi \hbar^{5/2} \sqrt{M n_r K_P}} e^{i\pi/4}. \quad (65)$$

The Maslov phase μ_{MP} (60) is determined in terms of the number of turning and caustic points by using the Maslov&Fedoriuk theory [2, 65–67, 69]. It is different for the smoothed,

$$\mu_{MP} = \sigma_{MP} - 1, \quad (66)$$

$$\sigma_{MP} = 3 M n_r + 4 M n_\theta,$$

and billiard,

$$\mu_{MP} = \sigma_{MP}, \quad (67)$$

$$\sigma_{MP} = 2 (M n_r + M n_\theta),$$

spherical potentials due to a difference in the quantum boundary conditions. The total Maslov phase $\mu_{MP}^{(\text{tot})}$ defined as a sum of the two terms, this asymptotic part (66) and the argument of the complex density amplitude (61), which is additional to the asymptotic one, depends on the energy E and parameters of the spherical potential as α in (44). This total Maslov phase is changed through the bifurcation points smoothly due to the second term.

The amplitude (61) of our solution (60) is regular at the bifurcations which are the end points $L = L^* = L_C$ of the action (L) part of a tori. The essential difference of the ISPM from the Berry&Tabor theory [4] is that the equation (60) for the orbits with the highest degeneracy is one of terms of the total solution of the breaking-of-symmetry problem. Thus, within the SPM of the EGA we have to consider separately the derivations of the other families in the spherical potentials, namely the circle and diameter $\mathcal{K} = 2$ orbits beyond the semiclassical Poisson summation trace formula (55).

The ISPM trace formula (60) for the contribution of the three-parametric MP families contains the *end* contributions related to the finite limits of the integrations in the error functions. This trace formula yields the contribution of the isolated $\mathcal{K} = 3$ families. This essentially was used in the derivation of (60) from the initial trace formula (51) taking 2π for the integral over the perpendicular angle Θ'' . Therefore, in (60), there is no contributions of the both circular and diametric orbits which correspond to the *end* stationary-phase points $L = L_C$ and $L = 0$, respectively.

3. The spherical billiard limit

In this limit [$\alpha \rightarrow \infty$ for the RPLP (44), and $V_0 \rightarrow \infty$ for the WS potential (45)] the action $S_{MP}(E)$ of the general spherical trace formula (55) is given by

$$S_{MP}(E) = p \mathcal{L}_{MP}, \quad p = \sqrt{2mE}, \quad (68)$$

where p is the momentum modulus [$V(r) = 0$ for $r \leq R$ and $V(r) = \infty$ at $r > R$ for $\alpha \rightarrow \infty$], $\mathcal{L}_{MP} = 2Mn_r R \sin \phi$ is the length of the polygonal orbit MP, $M(n_\theta, n_r)$, $R = r_{\max}$, the radius of the billiard, $\phi = \pi n_\theta / n_r$. $L_P = p r_{\min} = p R \cos \phi$ the angular momentum, and $t_{MP} = 2MRm n_r \sin \phi / p$ the period of the periodic orbit $M(n_\theta, n_r)$. The curvature K_P (28) of (59) and (65) can be calculated explicitly in this limit,

$$K_P = (\pi p R \sin \phi)^{-1}. \quad (69)$$

Substituting all of these quantities into (65), one obtains the Balian&Bloch trace formula for spherical billiards [2]:

$$\begin{aligned} \delta g^{(3)}(E) = & \frac{2mR^2}{\hbar^2} \text{Re} \sum_{M_\theta} \sum_{M_r > 2M_\theta} \sin(2\phi) \times \quad (70) \\ & \times \sqrt{\frac{pR \sin \phi}{\pi \hbar M_r}} \exp \left\{ \frac{i}{\hbar} p \mathcal{L}_{PO} - \right. \\ & \left. - \frac{i\pi}{2} \mu_{M_r, M_\theta} - \frac{3i\pi}{4} \right\}, \end{aligned}$$

where $M_r = Mn_r$ and $M_\theta = Mn_\theta$. However, the Maslov phase μ_{M_r, M_θ} is different for a slightly smoothed diffuse edge and strictly cavity potential, according to the Maslov& Fedoriuk catastrophe theory [65–69], see (66) and (67), respectively.

Note that all roots $L = L^* = L_P$ of the stationary phase equation (26) for $\mathcal{K} = 3$ families PO, $M(n_\theta, n_r)$, are in between minimal $L = L^* = 0$ for the diameters and maximal $L = L_C$ for the circular orbits, $0 < L_P < L_C$. The boundary stationary points $L = 0$ and $L = L_C$ are exclusion cases in relation to the derivations of their contributions into the phase space trace formula. The HO limit of the ISPM trace formula (60) is considered below together with the ISPM trace formula for the circular and diametric orbits.

C. TWO-PARAMETRIC CIRCLE FAMILIES

1. ISPM trace formulae for circle orbits

Within the EGA, for the contribution of the $\mathcal{K} = 2$ families of the circle (MC) orbits into the trace formula (20), we first integrate over φ'' and L_z as in Section IVB, see (50). In contrast to the derivations of contribution of the maximally degenerate $\mathcal{K} = 3$ orbits, for the circular orbits we now take into account existence of the isolated stationary point of the phase integral Φ_{CT} (2) in the perpendicular spherical phase-space variables $r'' = r''^* = r_C$, $p'_r = p'_r^* = 0$ in the center plane using the spherical phase-space variables $\{r'', \theta'', \varphi''; p'_r, p'_\theta, p'_\varphi\}$. Integrating exactly over the angular-momentum projection, $p_\varphi = L_z$, in (20), where the integrand is independent of L_z , and also, over p_θ by using the δ -function of the energy conservation, and taking then the integrals over φ'' and θ'' , one obtains

$$\begin{aligned} \delta g_{\text{scl}}(E) = & \frac{1}{2\pi^2 \hbar^3} \text{Re} \sum_{CT} \int_{r_-}^{r_+} dr'' \int_{p_r^-}^{p_r^+} dp'_r L \times \quad (71) \\ & \times T_{\theta, CT} |\mathcal{J}_{CT}(p'_r, p''_r)|^{1/2} \exp \left[\frac{i}{\hbar} \Phi_{CT} - \frac{i\pi}{2} \mu_{CT} \right]. \end{aligned}$$

Here we used the identity $\int d\Theta'' / \omega_\theta = T_{\theta, CT}$ [$T_{\theta, CT}$ is the time of particle motion along a CT] in (50)] as in Section IVB, see (52). The limits r_\pm and p_r^\pm for the remaining integrals in (71) correspond to the interval from the minimal $r_- = 0$ and $p_r^- = -p(r)$ to the maximal $r_+ = r_{\max} = R(E/V_0)^{1/\alpha}$ and $p_r^+ = p(r)$ values.

The stationary phase conditions for the SPM integration over the radial momentum p'_r and coordinate r'' in (71) are given by

$$\begin{aligned} \left(\frac{\partial \Phi_{CT}}{\partial p'_r} \right)^* & \equiv (r' - r'')^* = 0, \quad (72) \\ \left(\frac{\partial \Phi_{CT}}{\partial r''} \right)^* & \equiv -(p'_r - p''_r)^* = 0. \end{aligned}$$

Solutions of these equations are the isolated stationary point $p'_r = p'_r^* = 0$ and $r'' = r''^* = r_C$ related to the stationary point $L = L^* = L_C$ in the L variable.

They are equivalent to the closing (PO) conditions $r' = r'' = r_C$ and $p_r' = p_r'' = 0$ in the phase space. Here and below in this section the upper index star means that the corresponding quantity is taken at the stationary point $p_r' = p_r'' = 0$ of the isolated periodic circular orbit in a center plane. We expand now the phase Φ_{CT} (2) in the momentum p_r' and radial coordinate r'' near this phase-space point $\{p_r' = 0, r'' = r_C\}$. At second order, one has

$$\Phi_{CT} = S_{MC}(E) + \frac{1}{2} \mathcal{J}_{MC}^{(p)} (p_r')^2 + \frac{1}{2} \mathcal{J}_{MC}^{(r)} (r'' - r_C)^2, \quad (73)$$

where $S_{MC}(E)$ is the action along the circular PO, MC with the period number M ($\Phi_{CT}^* = S_{MC}$),

$$S_{MC}(E) = M \int_0^{2\pi} L d\theta = 2\pi M L_C, \quad (74)$$

L_C is the angular momentum of the particle moving along the PO MC , and M its repetition number. For the Jacobians $\mathcal{J}_{PO}^{(p)}$ and $\mathcal{J}_{PO}^{(r)}$, one finds

$$\mathcal{J}_{MC}^{(p)} = \left(\frac{\partial^2 \Phi_{CT}}{\partial p_r'^2} \right)_{MC} = \left(\frac{\partial r''}{\partial p_r'} \right)_{MC}, \quad (75)$$

$$\begin{aligned} \mathcal{J}_{MC}^{(r)} &= \left(\frac{\partial^2 \Phi_{CT}}{\partial r''^2} + 2 \frac{\partial^2 \Phi_{CT}}{\partial r' \partial r''} + \frac{\partial^2 \Phi_{CT}}{\partial r'^2} \right)^* = \\ &= \left(\frac{\partial p_r''}{\partial r''} - 2 \frac{\partial p_r'}{\partial r''} - \frac{\partial p_r'}{\partial r'} \right)_{MC} = \\ &= -F_{MC} \left[\mathcal{J}_{MC}^{(p)} \right]^{-1}, \end{aligned} \quad (76)$$

F_{MC} is the Gutzwiller stability factor,

$$F_{MC} = 2 - \text{Tr } \mathcal{M}_{MC} = 4 \sin^2 \left[\frac{\pi M \Omega_C}{\omega_C} \right], \quad (77)$$

$$\Omega_C = \sqrt{\frac{2\alpha E}{mR^2}} \left[\frac{(2+\alpha)V_0}{2E} \right]^{1/\alpha} > 0, \quad (78)$$

is the radial frequency, ω_C the azimuthal one,

$$\begin{aligned} \omega_C &= \omega_\theta(L = L_C) = L_C / (m r_C^2) = \\ &= \sqrt{\frac{\alpha V_0}{mR^2}} \left(\frac{2E}{(2+\alpha)V_0} \right)^{1/2-1/\alpha}. \end{aligned} \quad (79)$$

r_C is the radius of the C orbit, and L_C the angular momentum for a particle motion along the C PO, see (46). Therefore, for the bifurcation values of α which yield zeros of the Gutzwiller stability factor (77), one has

$$\frac{\Omega_C}{\omega_C} \equiv \sqrt{\alpha+2} = \frac{n_r}{n_\theta}. \quad (80)$$

With the identity in (80), from (77) one explicitly obtains

$$F_{MC} = 4 \sin^2 (\pi M \sqrt{\alpha+2}). \quad (81)$$

For the bifurcation point α_{bif} which turns the stability factor (81) into zero, from (80) one finds [84, 86, 87]

$$\alpha_{\text{bif}} = n_r^2 / n_\theta^2 - 2. \quad (82)$$

At this point, the P families appear and exist at $\alpha \geq \alpha_{\text{bif}}$ with the stationary point $L = L^* \leq L_C$ as the solution L^* of the PO equations (26). There is one specific bifurcation point $\alpha = 2$ which corresponds to the spherical harmonic oscillator (HO) with the frequency $\omega_0 = \sqrt{2V_0/R^2}$. For this α , the ratio ω_r/ω_θ found from (A.2) is identical to 2 at all of accessible L , i.e., one has 4 parametric families with $n_r = 2, n_\theta = 1$ which exist at any L within continuum $0 \leq L \leq E/\omega_0$. In this limit the ($K = 2$) MC family is not isolated but belongs to the four parametric family mentioned above along with diameters (see below). For spherical billiard limit, $\alpha \rightarrow \infty$, the circle orbit ($K = 2$) family disappears as degenerated into the center of billiard ($r_C \rightarrow 0, L_C \rightarrow 0$).

In the last equation of (76) we used the general definitions of the stability matrix (77) and properties of the action phase as a generating function, see also very right of (75) for the Jacobian $\mathcal{J}_{MC}^{(p)}$. Thus, the Jacobian calculations are reduced to those of the Jacobian $\mathcal{J}_{MC}^{(p)}$ (Appendix A4),

$$\mathcal{J}_{MC}^{(p)} = 2\pi(\alpha+2) M K_C r_C^2, \quad (83)$$

where K_C is the curvature for C orbits [87],

$$K_C = -\frac{(\alpha+1)(\alpha-2)}{12(\sqrt{\alpha+2})^3 L_C}. \quad (84)$$

Substituting the expansion (73) into (71) and taking the pre-exponent amplitude factor off the integrals at the stationary point $p_r' = p_r'' = 0$ and $r'' = r''^* = r_C$, one finally arrives at

$$\delta g_{\text{scl},C}^{(2)}(E) = \text{Re} \sum_M A_{MC}^{(2)} \times \quad (85)$$

$$\times \exp \left[\frac{i}{\hbar} S_{MC}(E) - \frac{i\pi}{2} \mu_{MC} \right].$$

The sum is taken over the repetition number M for the circle PO, $M = 1, 2, \dots$; $S_{MC}(E)$ is the action along the orbit MC (74). For amplitudes of the MC orbit contributions, one obtains

$$\begin{aligned} \mathcal{A}_{MC}^{(2)}(E) &= \frac{2iL_C T_C}{\pi \hbar^2 \sqrt{F_{MC}}} \times \\ &\times \text{erf} \left(\mathcal{Z}_{pMC}^+ \right) \text{erf} \left(\mathcal{Z}_{rMC}^-, \mathcal{Z}_{rMC}^+ \right), \end{aligned} \quad (86)$$

where T_C is the period of a particle motion along the primitive (one-repeated, $M = 1$) orbit C, $T_C = 2\pi/\omega_C$ (79), and F_{MC} is the Gutzwiller stability factor (81). The error functions are defined in (63). In these derivations, we used transformations to the new integration variables,

$$z_p = p_r' \sqrt{-\frac{i}{2\hbar} \mathcal{J}_{MC}^{(p)}}, \quad (87)$$

$$z_r = (r'' - r_C) \sqrt{\frac{iF_{MC}}{2\hbar \mathcal{J}_{MC}^{(p)}}}.$$

The finite limits in the error functions of (86), \mathcal{Z}_{pMC}^\pm and \mathcal{Z}_{rMC}^\pm , are given by

$$\mathcal{Z}_{pMC}^- = 0, \quad \mathcal{Z}_{pMC}^+ = \frac{L_C}{r_C} \sqrt{-\frac{i}{2\hbar} \mathcal{J}_{MC}^{(p)}}, \quad (88)$$

$$\mathcal{Z}_{r\ MC}^- = -r_C \sqrt{\frac{F_{MC}}{2i\hbar \mathcal{J}_{MC}^{(p)}}}$$

$$\mathcal{Z}_{r\ MC}^+ = (r_{\max} - r_C) \sqrt{\frac{iF_{MC}}{2\hbar \mathcal{J}_{MC}^{(p)}}},$$

where $\mathcal{J}_{MC}^{(p)}$ is the Jacobian (83). We took into account that the upper limit for the radial momentum p_r' is the momentum modulus $p(r_C) = L_C/r_C$ (lower limit is zero) and the upper limit for the radial coordinate r'' is r_{\max} of (24). Substituting (83) into (88), one finally arrives at the following arguments of error functions,

$$\mathcal{Z}_{p\ MC}^- = 0, \quad \mathcal{Z}_{p\ MC}^+ = L_C \sqrt{-\frac{i\pi}{\hbar}(\alpha + 2)MK_C}, \quad (89)$$

$$\mathcal{Z}_{r\ MC}^- = -\sqrt{\frac{iF_{MC}}{4\pi(\alpha + 2)\hbar MK_C}},$$

$$\mathcal{Z}_{r\ MC}^+ = \left(\frac{r_{\max}}{r_C} - 1\right) \sqrt{\frac{iF_{MC}}{4\pi(\alpha + 2)\hbar MK_C}}.$$

2. The SSPM limit

Asymptotically far from the bifurcations determined by roots of (80) [or (82), also far from the symmetry breaking point $\alpha = 2$] for the RPLP (44), we derive from (86)

$$\mathcal{A}_{MC}^{(2)}(E) = \frac{2L_C T_C}{\pi\hbar^2 \sqrt{F_{MC}}}. \quad (90)$$

The same result can be obtained directly from the initial trace formula (71) far from the symmetry breaking and bifurcation points by applying the SSPM. Indeed, assuming the isolated stationary point, $p_r'^* = 0$ and $r''^* = r_C$, in a plane crossing the center of the spherical symmetry, and expanding the action phase Φ , according to (73), one may extend the upper integration limit p_r^+ to ∞ . The lower integration limit $p_r^- = 0$ can be extended to $-\infty$ if we consider the repetition numbers $M = \pm 1, \pm 2$ and so on assuming the motion of particle in both direction. Then, one may reduce the trace formula to the same result above mentioned multiplying by factor 2 due to the time reversibility symmetry of the Hamiltonian independent of time as in subsection IVA. Taking the pre-exponent amplitudes off the integrals, we calculate explicitly the both integrals over p_r and r , and arrive at (85) with the amplitude $\mathcal{A}_{MC}^{(2)}$, equal exactly to (90). Note also that there is a difference from the standard Gutzwiller trace formula for isolated orbits because (85) with the amplitude (90) is the SSPM trace formula for a $\mathcal{K} = 2$ family of the circle orbits which are isolated in a fixed plane crossing the center.

The Maslov phase μ_{MC} in (85) is given by

$$\mu_{MC} = \sigma_{MC} + 1, \quad \sigma_{MC} = 2M. \quad (91)$$

For the calculation of this asymptotic Maslov index σ_{MC} through the turning and caustic points [see the trace formula (85) with the ISPM (86) and the SSPM (90) amplitudes], one can use the Maslov&Fedoriuk catastrophe

theory ([65–68, 87]). As usual, there is the two components of the Maslov phase in the ISPM trace formula (85) for the circular orbit families as in (60) for $\mathcal{K} = 3$ family. One of them is the asymptotic constant part (91) independent of the energy. Another part changes smoothly (continuously, with no jumps) through the bifurcation points. The total Maslov phase $\mu_{MC}^{(\text{tot})}$ for the family of MC orbits is then given by the sum of these two contributions mentioned above.

3. The harmonic oscillator limit

In the harmonic oscillator limit to the symmetry breaking point ($\alpha \rightarrow 2$) the stability factor F_{MC} (81) and curvature K_C , see (84), tend both to zero. However, there is a finite limit of the amplitude $\mathcal{A}_{MC}^{(2)}$ (86) at $\alpha \rightarrow 2$ because of the exact cancellation of singularities for $K_C \rightarrow 0$ and $F_{MC}/K_C \rightarrow 0$ in the expansion of the product of error functions ($\propto \mathcal{Z}_{p\ MC}^+ \mathcal{Z}_{r\ MC}^-$) with the denominator $\sqrt{F_{MC}}$ of (86). Taking into account the relation between the angular momentum L_C and energy E for this HO limit, $E = \omega_C L_C$, one obtains

$$\mathcal{A}_{MC}^{(2)}(E) \rightarrow \frac{E^2}{2(\hbar\omega_C)^3}. \quad (92)$$

This is a half of the spherical HO density amplitude [7], in addition to another one half coming from the diameters, as shown in the next Section IVD (the repetition number counts rotations along the circular orbit in one direction, $M = 1, 2, \dots$). The limit (92) can be found also directly from the trace formula (71) accounting for constant action phase and finite integration limits $r_- = 0$, $r_+ = r_{\max}$, $p_r^- = 0$, and $p_r^+ = p(r_C) = L_C/r_C$ ($L_C = E/\omega_C$, $T_C = 2\pi/\omega_C$),

$$\mathcal{A}_{MC}^{(2)} \rightarrow \frac{L_C T_C}{4\pi\hbar^3} \int_{r_-}^{r_+} dr \int_{p_r^-}^{p_r^+} dp_r =$$

$$= \frac{L_C^2 T_C}{4\pi\hbar^3} = \frac{E^2}{2(\hbar\omega_C)^3}. \quad (93)$$

Thus, one has a half of the HO trace formula amplitude (independent of M), up to relatively small second order terms in \hbar ,

$$\delta g_{MC}^{(2)}(E) \rightarrow \frac{1}{2} \delta g_{\text{HO}}^{(4)}(E), \quad (94)$$

where

$$\delta g_{\text{HO}}^{(4)}(E) = \frac{E^2}{(\hbar\omega)^3} \sum_{M=1}^{\infty} \cos \left[\frac{1}{\hbar} S_{\text{HO}}(E) - \frac{\pi}{2} \mu_{\text{HO}} \right], \quad (95)$$

$S_{\text{HO}} = 2\pi M E/(\hbar\omega)$ is the action along POs of the 4 parametric family in the HO potential, $\omega = \omega_\theta = \omega_r/2$ is the HO frequency, $\mu_{\text{HO}} = \sigma_{\text{HO}} = 2M$ [7, 64].

4. The bifurcation limit

Taking the limit to the bifurcations $F_{MC} \rightarrow 0$, where $\alpha \rightarrow \alpha_{\text{bif}} = n_r^2/n_\theta^2 - 2$ for the potential (44), see (82),

but far from the HO limit $\alpha = 2$, one finds that the argument of the second error function in (86) coming from the radial-coordinate integration tends to zero as $\sqrt{|F_{MC}|}$ (89). Thus, the singular stability factor F_{MC} of the denominator (86) is exactly canceled by the same from the numerator, and we arrive at the finite result:

$$\mathcal{A}_{MC}^{(2)}(E) = \frac{iL_C}{4\hbar^2 \omega_C} \sqrt{(\alpha+2) M K_C} \times \quad (96)$$

$$\times \operatorname{erf} \left(\mathcal{Z}_p^{(+)} \right).$$

5. The separatrix

At the potential barrier (separatrix) when $K_C \rightarrow \infty$ one has the continuous zero limit. Thus, one finds the continuous transition of the ISPM amplitude $\mathcal{A}_{MC}^{(2)}$ through all bifurcation points and separatrix, including potential barriers. The HO limit will be discussed after derivations of the diameter family contributions.

D. TWO-PARAMETRIC DIAMETER FAMILIES

1. ISPM trace formulae for the diameters

For the diameter-orbit $\mathcal{K} = 2$ family contribution into the trace formula (1) for a spherical potential, we take first the integral over p'_\parallel of the momentum integration by using the energy conservation δ -function,

$$\delta g_{\text{scI}}(E) = \frac{m}{(2\pi\hbar)^3} \operatorname{Re} \sum_{\text{CT}} \int d\mathbf{r}'' \int \frac{d\mathbf{p}'_\parallel}{p'_\parallel} \times \quad (97)$$

$$\times |\mathcal{J}_{\text{CT}}(\mathbf{p}'_\perp, \mathbf{p}''_\perp)|^{1/2} \exp \left[\frac{i}{\hbar} \Phi_{\text{CT}} - \frac{i\pi}{2} \mu_{\text{CT}} \right].$$

We used a local coordinate system with x directed to this diametric orbit, $x_\parallel = x$, and $\mathbf{r}_\perp = \{y, z\}$ perpendicular to it, and similarly, for Cartesian momenta, $p_\parallel = p_x$ and $\mathbf{p}_\perp = \{p_y, p_z\}$. The phase integral Φ_{CT} (2) in the integrand over the perpendicular momentum \mathbf{p}_\perp , has obviously the isolated stationary point, $\mathbf{p}'_\perp = \mathbf{p}''_\perp \equiv \mathbf{p}_\perp^* = 0$, in the subspace of the perpendicular variables in the local Cartesian coordinate system introduced above. This point is the solution of the stationary phase condition:

$$\left(\frac{\partial \Phi_{\text{CT}}}{\partial \mathbf{p}'_\perp} \right)^* \equiv (\mathbf{r}'_\perp - \mathbf{r}''_\perp)^* = 0. \quad (98)$$

The SPM condition determining the isolated stationary point is the closing condition:

$$\mathbf{r}'_\perp^* = \mathbf{r}''_\perp^* \equiv \mathbf{r}_\perp, \quad (99)$$

according to the definition of the phase Φ_{CT} (2) with (3). As the stationary phase conditions for the next integration over the spacial coordinates are identities due to the spherical symmetry, the star means that CT is the periodic orbit (PO) which is now the diameter orbit, $MD = M(2,1)$ (with the M number of periods). Expanding the phase integral Φ_{CT} (2) near the isolated

stationary point at second order, one has

$$\Phi_{\text{CT}} = S_{MD}(E) + \frac{1}{2} J_{yD}^{(p)} (p'_y)^2 + \quad (100)$$

$$+ \frac{1}{2} J_{zD}^{(p)} (p'_z)^2 = S_{MD}(E) + \frac{1}{2} J_{\perp MD}^{(p)} (p'_\perp)^2,$$

where $S_{MD}(E)$ is the diameter action accounting for the period number M , $S_{MD} = M S_D$, S_D is the action along the primitive ($M = 1$) diameter (2,1) ($\Phi_{\text{CT}}^* = S_{MD}$). As shown in Appendix A5 by using the symmetry of Jacobians [taken at the diameter orbit (D), $\mathcal{J}_{yD}^{(p)} = \mathcal{J}_{zD}^{(p)} = \mathcal{J}_{\perp D}^{(p)}$] with respect to rotations around the diameter, one obtains

$$\mathcal{J}_{\perp MD}^{(p)} = \left(\frac{\partial^2 \Phi_{\text{CT}}}{\partial p_y'^2} \right)^* = -2\pi M K_D r^2, \quad (101)$$

where the star means $\mathbf{p}'_\perp = \mathbf{p}_\perp^* = 0$, at the MD PO, and K_D is the diameter curvature [87],

$$K_D = \frac{\Gamma(1 - 1/\alpha)}{\Gamma(1/2 - 1/\alpha) \mathcal{E} \sqrt{2\pi m R^2 V_0}}, \quad (102)$$

where $\Gamma(x)$ is the Gamma function. The last expression was obtained by using the explicit expression of the solution for the trajectory $\theta(r)$ in an azimuthal plane crossing the diameter PO [58]. In this plane, one considers a small variation of the initial momentum $\delta p'_y$ perpendicular to the diameter orbit (D) of a particle moving along a trajectory perturbed near the diameter at its given point $r' = r$ through variations of the perpendicular coordinate $\delta y'$ and the corresponding change of angular momentum δL , see (A.23). We used also the standard Jacobian relations (A.24) to reduce the calculation of the Jacobian $\mathcal{J}_{\perp D}^{(p)}$ to another simpler Jacobian $(\delta\theta''/\delta L)_D$. As shown in Appendix A5, due to the azimuthal symmetry for rotations around the diameter, this intermediate Jacobian $(\delta\theta''/\delta L)_D$ taken at the D is invariant [59] as expressed through the invariant diameter curvature (28) [see (A.27)].

We substitute now the expansion (100) for the phase integral Φ_{CT} and (101) for the Jacobian $\mathcal{J}_{\perp}^{(p)}$ into (97). We use also the cylindrical coordinates for the integration over the perpendicular momentum \mathbf{p}'_\perp , $d\mathbf{p}_\perp = p_\perp dp_\perp d\varphi_p$, and spherical coordinate system for the integration over \mathbf{r}'' , $d\mathbf{r} = r^2 dr \sin\theta d\theta d\varphi$. Taking the integrals over the azimuthal angles φ_p and spherical angles θ, φ (2π and 4π , respectively, because of independence of the integrand on these angles from the spherical symmetry), one obtains

$$\delta g_{\text{scI}D}^{(2)}(E) = \operatorname{Re} \sum_M A_{MD}^{(2)} \times \quad (103)$$

$$\times \exp \left[\frac{i}{\hbar} S_{MD}(E) - \frac{i\pi}{2} \mu_{MD} \right].$$

where

$$A_{MD}^{(2)} = \frac{m}{\pi\hbar^3} \int_0^{r_{\max}} r^2 dr \int_0^{p(r)} \frac{p_\perp dp_\perp}{\sqrt{p^2 - p_\perp^2}} \times \quad (104)$$

$$\times \exp \left(-\frac{i\pi}{\hbar} M K_D r^2 p_\perp^2 \right).$$

(We omitted primes and double primes for the integration variables, for simplicity, $p_{\parallel} = \sqrt{p^2 - p_{\perp}^2} p(r) = \sqrt{2m[E - V(r)]}$ for arbitrary spherical potential. Using the dimensionless variables, $u = r/r_{\max}$, and $t = p_{\perp}/p$, one can re-write (104) in a more convenient form:

$$\mathcal{A}_{MD}^{(2)} = \frac{m}{\pi \hbar^3} r_{\max}^3 \sqrt{2mE} \mathcal{I}(M\zeta), \quad (105)$$

where

$$\mathcal{I}(M\zeta) = \int_0^1 u^2 du \sqrt{1 - u^2} \mathcal{F}(Mq), \quad (106)$$

$$\mathcal{F}(q) = \int_0^1 \frac{tdt}{\sqrt{1 - t^2}} \exp(iqt^2), \quad (107)$$

with

$$q = \zeta u^2 (1 - u^2), \quad (108)$$

$$\begin{aligned} \zeta &= -2\pi K_D r_{\max}^2 mE/\hbar, \\ r_{\max} &= R(E/V_0)^{1/\alpha}. \end{aligned} \quad (109)$$

The internal integral $\mathcal{F}(Mq)$ (107) can be calculated exactly analytically in terms of the error function of a complex argument (63) by using the suitable integration variables

$$w = \sqrt{1 - t^2}, \quad z_w = \sqrt{iMq} w, \quad (110)$$

to arrive at

$$\mathcal{F}(q) = \frac{\sqrt{\pi}}{2} \frac{e^{iq}}{\sqrt{iq}} \operatorname{erf}(\sqrt{iq}). \quad (111)$$

Collecting (111), (106), (109) and (108) for the RPLP (44), one obtains a simple integral representation of the diameter amplitude through the error function,

$$\begin{aligned} \mathcal{I}(M\zeta) &= \frac{\sqrt{\pi}}{2\sqrt{iM\zeta}} \int_0^1 u du \times \\ &\times \exp[iM\zeta u^2 (1 - u^2)] \times \\ &\times \operatorname{erf}[\sqrt{iM\zeta u^2 (1 - u^2)}]. \end{aligned} \quad (112)$$

2. The HO limit

Taking the limit $\zeta \rightarrow 0$ to the spherical harmonic oscillator value $\alpha \rightarrow 2$ ($K_D \rightarrow 0$), one obtains a half of the HO amplitude (accounting negative and positive repetition numbers M and time-reversibility by factor 2 with the summation in positive integers $M = 1, 2, \dots$), one finds for (104)

$$A_{MD} \rightarrow \frac{1}{2} \frac{E^2}{(\hbar\omega)^3}. \quad (113)$$

This limit is a half of the HO shell-correction density amplitude (independent of M) (95).

3. Simplified diameter trace formulae

As usual, in these derivations within the ISPM, the constant ζ , which is proportional to the curvature K_D [see (102)] going to zero, is canceled with that coming from the expansion of the integrand near the catastrophe points. We took also into account that $V_0 = mR^2\omega^2/2$ for the spherical harmonic oscillator ($\alpha \rightarrow 2$). The radial period can be explicitly calculated,

$$\begin{aligned} T_r &= \frac{2\pi}{\omega_r} = 2m \int_0^{r_{\max}} \frac{dr}{p(r)} = \\ &= \frac{2mr_{\max}}{\sqrt{2mE}} \frac{\sqrt{\pi}\Gamma(1 + 1/\alpha)}{\Gamma(1/2 + 1/\alpha)} \rightarrow \\ &\rightarrow \frac{2\pi}{\omega} \quad \text{for } \alpha \rightarrow 2. \end{aligned} \quad (114)$$

$[r_{\max} \rightarrow (2E/m\omega^2)^{1/2}$ for $\alpha \rightarrow 2$ but $\omega_r = 2\omega$].

Within the accuracy of the simplest version of the ISPM (second order expansion of the phase and zero order of the amplitude in the integrand), taking the pre-exponent amplitude factor $\sqrt{p^2 - p_{\perp}^2}$ in the internal integral in (5) over the modulus of the perpendicular momentum p_{\perp} off the integral at the stationary point $p_{\perp} = p_{\perp}^* = 0$, $p_{\parallel}^* = \sqrt{p^2 - (p_{\perp}^*)^2} = p(r)$, one finds that this integral can be calculated analytically with the finite integration limits in terms of the elementary functions. Substituting also the Jacobian expression (101) and using the spherical coordinates for the spacial-coordinate integration variable \mathbf{r} , (r, θ, φ) as above, we calculate the integral over angles θ, φ (just 4π from the spherical symmetry). Then, the diameter contribution (5) into the trace formula (1) for any spherical potentials $V(r)$ can be resulted in (103) but with a much simpler amplitude,

$$\begin{aligned} A_{MD}^{(2)} &= \frac{m}{\pi \hbar^3} \int_0^{r_{\max}} \frac{r^2 dr}{p(r)} \int_0^{p(r)} p_{\perp} dp_{\perp} \times \\ &\times \exp\left(-\frac{i\pi}{2\hbar} M K_D r^2 p_{\perp}^2\right), \end{aligned} \quad (115)$$

where $p(r)$ is the momentum modulus depending on the radial coordinate r through the radial potential, e.g., the RPLP (44). Taking the internal integral explicitly analytically, one finds from (115) for the diameter amplitude $\mathcal{A}_{MD}^{(2)}$ in the case of the RPLP (44) the following simple one-dimensional integral representation:

$$A_{MD}^{(2)} = \frac{mr_{\max}^3 \sqrt{2mE}}{2\pi i \hbar^3 M \zeta} [I(M\zeta) - I(0)], \quad (116)$$

where

$$I(\zeta) = \frac{1}{r_{\max}} \int_{r_{\min}}^{r_{\max}} \frac{dr}{\sqrt{1 - V(r)/E}} \exp[i\zeta \Phi(r)], \quad (117)$$

with the same ζ (109),

$$\Phi(r) = r^2 (1 - V(r)/E) / r_{\max}^2, \quad (118)$$

r_{\min} and r_{\max} are the turning points in the RPLP $V(r)$, $r_{\min} = 0$ for the diameter PO.

Substituting now the RPLP $V(r)$ (44) and using a new radial variable $u = r/r_{\max}$ as above (109), we present the integral $I(M\zeta)$ in the dimensionless form (A.28) with the amplitude $\mathcal{A}(u)$ (A.30) and phase $\Phi(u)$ (A.29). For the RPLP (44), one explicitly finds (A.37), (A.38), (102) and (A.2) (Appendix A6).

For large ζ (109), one can use the SPM evaluation of the integral (117) in terms of the error functions (119). Accounting for the two stationary points u_1 and u_2 (A.32) ($u_2 = 0$) in the phase function $\Phi(u)$ (A.31), one obtains

$$I(M\zeta) \approx \sqrt{\frac{\pi(\alpha+2)}{4iM\zeta\alpha^2}} \times \quad (119)$$

$$\times \operatorname{erf}(\mathcal{Z}_{1MD}^+, \mathcal{Z}_{1MD}^-) e^{iM\zeta\Phi_1} +$$

$$+ \sqrt{\frac{i\pi}{4M\zeta}} \operatorname{erf}(\mathcal{Z}_{2MD}^+).$$

In the contribution of the second stationary point u_2 we have to keep the amplitude u as it is. The arguments of the error functions, \mathcal{Z}_{1MD}^\pm and \mathcal{Z}_{2MD}^+ in (119), are given by

$$\mathcal{Z}_{1MD}^+ = \sqrt{-iM\zeta\Phi_1''/2} (1 - u_1), \quad (120)$$

$$\mathcal{Z}_{1MD}^- = -\sqrt{-iM\zeta\Phi_1''/2} u_1,$$

$$\mathcal{Z}_{2MD}^+ = \sqrt{-iM\zeta\Phi_2''/2},$$

where

$$\Phi_1 = \Phi(u_1) = \frac{\alpha}{\alpha+2} \left(\frac{2}{\alpha+2} \right)^{2/\alpha}, \quad (121)$$

and $\Phi_1'' = \Phi''(u_1)$ and $\Phi_2'' = \Phi''(u_2)$, are curvatures (A.35); see also (A.32) for u_1 . For the limit $|\zeta| \rightarrow \infty$, from (119) one has the same as directly from (116),

$$I(M\zeta) \rightarrow \sqrt{\frac{\pi(\alpha+2)}{iM\zeta\alpha^2}} e^{iM\zeta\Phi_1} + \sqrt{\frac{i\pi}{4M\zeta}}. \quad (122)$$

4. The SSPM and billiard limit

Taking the limit $|\zeta| \gg 1$, from (116) one finally obtains the SSPM trace formula with the same amplitude $\mathcal{A}_{MD}^{(2)}$ as we would get directly from integrations (5) over p'_y and p'_z at the simplest second order in the phase integral and zero order in the amplitude expansion, and extension of the integration limits up to $\pm\infty$ (taking also into account the factor 2 in the trace formula reducing it to the summation over $M = 1, 2, \dots$). Finally, from (116) [or (5)] one finds the SSPM limit:

$$\mathcal{A}_{MD}^{(2)} \rightarrow \frac{1}{i\pi M K_D \omega_r \hbar^2}. \quad (123)$$

With this amplitude for $\alpha \rightarrow \infty$, one then obtains from (103) the Balian-Bloch trace formula [2] for the diameter

orbits in the spherical billiard,

$$\delta g_{D,BB}^{(2)}(E) = -\frac{2mR^2}{\hbar^2} \sum_{M=1}^{\infty} \frac{1}{2\pi M} \sin\left(\frac{4}{\hbar} MpR\right). \quad (124)$$

The Maslov phase μ_{MD} for the diameters in spherical billiard is given by

$$\mu_{MD} = \sigma_{MD} - 1, \quad \sigma_{MD} = 4M. \quad (125)$$

In these derivations of the spherical billiard limit, one should take into account the asymptotics $\alpha \rightarrow \infty$ for the curvature,

$$K_D \rightarrow -\frac{1}{\pi pR} = -\frac{1}{\pi R \sqrt{2mE}}. \quad (126)$$

Thus, from the amplitude in the one-integral representation (112) we obtained the two limits $\alpha \rightarrow 2$ (a half of the HO trace formula (95) [7, 64]) and $\alpha \rightarrow \infty$ (the spherical billiard [2]), and also the standard SSPM approach.

The constant ζ which is proportional to the singular curvature K_D (102) is canceled near the catastrophe points, as usual within the ISPM. In these derivations, one should take into account that $V_0 = mR^2\omega^2/2$ for the spherical harmonic oscillator ($\alpha \rightarrow 2$), and (114) for the diameter period.

E. TOTAL RPLP TRACE FORMULAE

1. Averaged density

The total ISPM trace formula for the RPLP is the sum of the contribution of the $\mathcal{K} = 3$ polygon-like (P) families $\delta g_P^{(3)}(E)$ (60) with (61), the $\mathcal{K} = 2$ circular (C) orbits $\delta g_C^{(2)}(E)$ (85) [with (86)], and the $\mathcal{K} = 2$ diameters (D) $\delta g_D^{(2)}(E)$ [(103) with (116) for larger α and (105) for smaller $\alpha \rightarrow 2$],

$$\delta g_{\text{scl}}(E) = \delta g_P^{(3)}(E) + \delta g_C^{(2)}(E) + \delta g_D^{(2)}(E). \quad (127)$$

This trace formula has the correct finite asymptotic limits to the SSPM, the Berry&Tabor result (60) and (65) for the $\mathcal{K} = 3$ polygon-like; and the $\mathcal{K} = 2$ for the diameter (103) and [(123)]; and the circle [85] and (90)] POs.

According to the general trace formulas (9) and (16) [3, 7, 8, 87], for the averaged density $\delta g_\Gamma(E)$ (with the Gaussian weight function specified by the averaging parameter Γ much smaller than the Fermi energy E_F) in terms of the scaled-energy level density,

$$\mathcal{G}_\gamma(\mathcal{E}) = g_\Gamma(E) \frac{dE}{d\mathcal{E}}, \quad \gamma = \Gamma \frac{d\mathcal{E}}{dE}, \quad (128)$$

as a function of the scaled energy \mathcal{E} (49), one obtains

$$\mathcal{G}_{\text{scl}}(\mathcal{E}) = \mathcal{G}_{\text{ETF}}(\mathcal{E}) + \delta \mathcal{G}_P^{(3)}(\mathcal{E}) + \quad (129)$$

$$+ \delta \mathcal{G}_C^{(2)}(\mathcal{E}) + \delta \mathcal{G}_D^{(2)}(\mathcal{E}).$$

Here, γ is the scaled averaging parameter, $\mathcal{G}_{\text{ETF}}(\mathcal{E})$ is the scaled smooth part obtained within the ETF approximation [7]. Its TF component $\mathcal{G}_{\text{ETF}}(\mathcal{E})$ corresponds to

$$g_{\text{TF}}(E) = \frac{2m}{\pi\hbar^3} \int_0^{r_{\text{max}}} r^2 dr p(r), \quad (130)$$

with $H(p, r) = p^2/2m + V(r)$ and $p(r)$ given by (22). For the scaled TF approach, one obtains explicitly [84],

$$\mathcal{G}_{\text{TF}}(\mathcal{E}) = c_0 \mathcal{E}^2, \quad c_0 = \frac{2\sqrt{2}}{\pi} B\left(1 + \frac{3}{\alpha}, \frac{3}{2}\right), \quad (131)$$

with the Euler beta function $B(s, t)$. The next-order term [7] can be also given analytically [84], and one has the ETF density

$$\mathcal{G}_{\text{ETF}}(\mathcal{E}) = c_0 \mathcal{E}^2 + c_1, \quad (132)$$

$$c_1 = -\frac{\alpha+1}{12\sqrt{2}\pi} B\left(1 + \frac{1}{\alpha}, \frac{1}{2}\right).$$

According to (16), the oscillating terms of (129) take the form:

$$\delta\mathcal{G}_{\gamma, \text{PO}}^{\mathcal{K}}(\mathcal{E}) = \delta\mathcal{G}_{\text{PO}}^{\mathcal{K}}(\mathcal{E}) \exp(-\tau_{\text{PO}}^2 \gamma^2 / 4), \quad (133)$$

where $\tau_{\text{PO}} = t_{\text{PO}} dE/d\mathcal{E}$ is the scaled period (49),

$$\mathcal{G}_{\text{PO}}^{(\mathcal{K})} = g_{\text{PO}}^{(\mathcal{K})}(E) \frac{dE}{d\mathcal{E}}, \quad (134)$$

see (60), (85) and (103).

2. Shell-correction energy

The periodic orbit expansion for the semiclassical shell-correction energy δU is shown by (18) with $\delta g_{\text{PO}}(E)$ given in (127) at $E = E_F$ [3, 7, 62, 70, 87] where $t_{\text{PO}} = Mt_{\text{PO}}^{M=1}(E_F)$ is the time of a particle motion along the PO in the RPLP (taking into account its repetition number M) at the Fermi energy $E = E_F$. The Fermi energy E_F is related to the conservation of the particle number N through the equation (19),

$$N = 2 \int_0^{\mathcal{E}_F} d\mathcal{E} \mathcal{G}(\mathcal{E}). \quad (135)$$

According to [3, 7, 9, 87], for the corresponding dimensionless scaled shell-correction energy,

$$\delta\mathcal{U}_{\text{scl}} = (d\mathcal{E}/dE) \delta U_{\text{scl}}, \quad (136)$$

with (18) for δU_{scl} , one obtains

$$\delta\mathcal{U}_{\text{scl}} = 2 \sum_i \mathcal{E}_i \delta n_i \approx \quad (137)$$

$$\approx 2 \sum_{\text{PO}} \frac{\hbar^2}{\tau_{\text{PO}}^2} \delta\mathcal{G}_{\text{PO}}^{(\mathcal{K})}(\mathcal{E}_F).$$

Here, δn_i is the variation of occupation numbers defined by the Strutinsky smoothing procedure [9, 10], and the sum over PO runs all P, C and D families (with repetitions) [(60), (85) and (103) for $\delta g_{\text{PO}}^{\mathcal{K}}$ components, relatively].

As mentioned in Section IIA3, the scaled shell-correction energy $\delta\mathcal{U}$ (137), which is the observed (dimensionless) physical quantity, does not contain arbitrary averaging parameter γ , in contrast to the oscillating level density $\delta\mathcal{G}_{\gamma}(\mathcal{E})$. The convergence of the PO sum (137) is ensured by the additional factor in front of the density component $\delta\mathcal{G}_{\text{PO}}^{\mathcal{K}}$ which is inversely proportional to the scaled period τ_{PO} squared along the PO. Therefore, we need (scaled) short-time POs in the RPLP if they occupy sufficiently large phase-space volume in terms of the scaled quantities.

3. Fourier transform

The Fourier transform of the semiclassical level density with respect to the scaled-period variable τ is given by

$$F(\tau) = \int d\mathcal{E} g(\mathcal{E}) e^{i\mathcal{E}\tau} e^{-\gamma^2 \mathcal{E}^2 / 2} \approx \quad (138)$$

$$\approx F_0(\tau) + \pi \sum_{\text{PO}} F_{\text{PO}} \delta_{\gamma}(\tau - \tau_{\text{PO}}),$$

$$\delta_{\gamma}(x) \equiv \frac{1}{\sqrt{2\pi}\gamma} e^{-x^2/2\gamma^2},$$

which exhibits peaks at periodic orbits $\tau = \tau_{\text{PO}}$. In (138), $F_0(\tau)$ represents the Fourier transform of the smooth ETF level density and has a peak at $\tau = 0$ related, in the case of the simple TF approach, to the direct (zero-action) trajectory [8, 87]. Thus, from the Fourier transform of the quantum-mechanical level density,

$$F(\tau) = \int \left[\sum_i \delta(\mathcal{E} - \mathcal{E}_i) \right] d\mathcal{E} \times \quad (139)$$

$$\times e^{i\mathcal{E}\tau} e^{-\gamma^2 \mathcal{E}^2 / 2} = \sum_i e^{i\mathcal{E}_i \tau} e^{-\gamma^2 \mathcal{E}_i^2 / 2},$$

$$\psi_i = (E_i/V_0)^{\frac{1}{2} + \frac{1}{\alpha}},$$

one can directly extract information about the amplitudes A_{PO} of the classical PO contributions into the level density (9).

4. The harmonic oscillator limit

In the harmonic oscillator limit [$\alpha \rightarrow 2$ in the RPLP (44)], the energy surface is simplified to the linear function in actions,

$$E = \omega_r I_r + \omega_{\theta} I_{\theta} = \omega_{\theta} (2 I_r + L). \quad (140)$$

In this limit the curvature K_{PO} , see (28), at $L = L_{\text{PO}}$ for all POs including the maximal value $L = L_C = E/\omega_{\theta}$ for circular orbits as well as the Gutzwiller stability factor F_{MC} turn into zero, see also the specific expressions for the diameter curvature K_D (102) and the circle one K_C (84). However, there is no singularities in amplitudes of the ISPM trace formula (85) [with (86)] for $F_{\text{MC}} \rightarrow 0$ and $K_C \rightarrow 0$ because the arguments of all error functions go to zero as explained above, see also a similar

cancellation of the singularities for $K_D \rightarrow 0$ ($\zeta \rightarrow 0$) in (105) with (112).

The contribution of the three-parametric polygonal-like orbits $\delta g_P^{(3)}(E)$ in (127) disappears in the HO limit because the action (time of the particle motion) goes to the infinity for $n_r/n_\theta \rightarrow 2$ when $n_\theta \rightarrow \infty$ and $n_r > 2n_\theta \rightarrow \infty$. Therefore, for any finite averaging parameter Γ , one can neglect their contributions to the averaged level density (16) [or in (129) with (133) and (134)]. These P orbits do not contribute also into the shell-correction energy (18) in this limit $\alpha \rightarrow 2$ due to the factor $\propto 1/t_{PO}^2 \rightarrow 0$ for time-long POs.

Thus, in the HO limit ($\alpha \rightarrow 2$), one can assume that the two kind of other families with $\mathcal{K} = 2$ of the diameter and circular orbits form together the $\mathcal{K} = 4$ family of the HO Hamiltonian. As shown above, in this limit they give the same contributions and their sum is the HO trace formula $\delta g_{HO}^{(4)}(E)$ (95) up to the higher order terms in \hbar which were neglected in our derivations.

As the result, the HO limit of the sum of the circular and diameter orbit contributions is the HO trace formula with the precision of the higher order terms in \hbar .

F. COMPARISON WITH QUANTUM RESULTS

Figure 12 shows the Fourier transform of the quantum-mechanical level density $g(\mathcal{E})$ for the RPLP [see (138)]. For a smaller $\alpha = 2.1$, the diameter (2,1) (D), and circle (1,1) (C) ($M = 1$) orbits yield the dominant contribution to the gross-shell structure as the shortest POs (see the peak at $\tau \sim 5.0$). These primitive diameter D and circle C peaks which appear at almost the same $\tau \approx 5.0$ cannot be distinguished, and they are seen as a common peak of their sum. Other MD and MC orbits with $M > 1$ give smaller contributions at larger τ . With increasing α ($\alpha = \alpha_{\text{bif}} = 4.25$ and 7), the amplitudes of the oscillating level density for these orbits are decreased, and one finds a prominent enhancement around the bifurcation points, $\tau \sim 11.2$ at $\alpha_{\text{bif}} = 4.25$ and $\tau \sim 6.2$ at $\alpha_{\text{bif}} = 7.0$. However, near these bifurcations, the contribution of the newborns star- (5,2) and triangle-like (3,1) families, having a higher degeneracy $\mathcal{K} = 3$, becomes important also for larger $\alpha > \alpha_{\text{bif}}$. The newborn (5,2) and (3,1) peaks cannot be distinguished from the parent circular 2C and C orbits near the corresponding bifurcation points α_{bif} , as in the case of the diameter and circular orbits at α close to the HO limit. Notice, in good agreement with the Fourier transforms (Fig. 12), the remarkable enhancement is found in the oscillating level density amplitude $A_{PO}^{(\mathcal{K})}$ of the PO family having different order of \hbar with respect to the Gutzwiller trace formula for the isolated POs (see 15). However, the phase-space volume occupied by a circular-orbit family at its bifurcation becomes negligible, and all amplitude enhancement becomes inherent to the bifurcating $\mathcal{K} = 3$ family on right of the bifurcation point.

Figs. 13–15 show a nice agreement of the coarse-grained ($\gamma = 0.6$) and fine-resolved ($\gamma = 0.03–0.2$) semiclassical and the quantum level densities $\delta \mathcal{G}_\gamma(\mathcal{E})$ (divided by \mathcal{E}) as functions of the scaled energy \mathcal{E} at $\alpha = 6.0$.

This value of α is remarkable as $\alpha = 2$ and 4 because all classical critical characteristics of all POs can be found explicitly analytically, and therefore, one has a very high precision of the calculations of trace formulas, as shown in [87]. The ISPM results at this value of α are in good agreement with the SSPM ones because α is far away from the main bifurcations of the short-time POs at $\alpha = 4.25$ and 7.0, as well as from the HO symmetry-breaking point $\alpha = 2$. As seen from Figs. 16–18 for the birth of triangle-like (3,1) ($\alpha = 7$) POs in a typical bifurcation scenario, one has also good agreement of the ISPM with quantum results. Note that the SSPM of these PO contributions show a sharply pronounced discontinuity of their amplitudes; and for the 2C and C orbits, one finds a divergent behavior, in contrast to the continuous ISPM PO components. We demonstrate that the ISPM solves successfully these catastrophe problems of the SSPM. For the averaged semiclassical trace formula we used (129). For quantum calculations we employed the standard Strutinsky averaging (over the scaled energy \mathcal{E}), finding a good plateau around the Gaussian averaging width $\tilde{\gamma} = 2–3$ and curvature-correction degree $\mathcal{M} = 6$.

The C and D POs with the shortest (scaled) periods τ are dominating at large averaging parameter $\gamma = 0.6$ (coarse-graining, or gross-shell structure) while much more families with a relatively long period τ at $\gamma = 0.03–0.2$ (fine-resolved shell structure) become significant in comparison with the quantum results [see the panels (b) in Figs. 13–15]. Notice that for the exemplary bifurcation 7.0 at smaller $\gamma \lesssim 0.2$ the dominating orbits become the bifurcating newborn (3,1) of the highest degeneracy $\mathcal{K} = 3$ along with leading (5,2), (7,3), and (8,3) POs which were born at smaller bifurcations. This is in nice agreement with the quantum Fourier transforms shown in Fig. 12. These POs yield more contributions near the bifurcation values of α and even more on their right in a wide region of α . Moreover, the bifurcating parent circular-orbit family MC does not contribute relatively in the bifurcation scenario because the lower, and the upper radial integration limits for the ISPM MC amplitudes (86) coincide at their bifurcation point $\alpha = \alpha_{\text{bif}}$ with the radius $r = r_C$: They occupy the zero phase-space volume at the bifurcation value $\alpha = \alpha_{\text{bif}}$.

Figs. 19 and 20 show the semiclassical shell-correction energy δU_{scl} [(137) in units of $(\mathcal{E} dE/d\mathcal{E})_F$] as function of the particle (neutron or proton) number variable $N^{1/3}$ (19). They were calculated by using the PO sum (137) and the standard relationship $N = N(\mathcal{E}_F)$, see (135), after the scale transformation (136) [87]. The corresponding quantum shell-correction calculations are performed by using the Strutinsky smoothing procedure (see, e.g., [10]). For the sake of convenience, one can use averaging of the level density $g(\mathcal{E})$ with a small parameter $\gamma = 0.1$ in (135) for the relationship between the particle number and the Fermi (scaled) energy \mathcal{E}_F , $N = N(\mathcal{E}_F)$, as this integral characteristics is almost insensitive of variations of $\gamma \approx 0.02 \div 0.1$, at least.

More precised results for the semiclassical shell-correction energy δU as functions of the particle number $N^{1/3}$, especially near its minima, are obtained with using the quantum level density for the re-calculation of

the Fermi energy \mathcal{E}_F to the particle number N through (135). The reason is rather a slow convergence of the semiclassical expansion of the phase integral in terms of the POs in (135) as compared with the PO sum for the shell-correction energy (137) at a given Fermi energy \mathcal{E}_F . A good plateau for the quantum calculations of the scaled shell-correction energy is realized near the same averaging parameters $\tilde{\gamma}$ and \mathcal{M} mentioned above. We have to point out that the quality of the plateau in the SCM calculations is much better with using the scaled-energy variable \mathcal{E} rather than the energy E itself, except for the HO limit $\alpha = 2$, where these energies coincide [87]. For instance, as well-known, for the spherical billiard case $\alpha \rightarrow \infty$, the plateau condition can be obtained in terms of the scaled energy \mathcal{E} which is the wave number $\sqrt{2mE}/\hbar$, instead of the energy E . For the relation $N = N(\mathcal{E}_F)$ we used specifically an averaging in small $\gamma = 0.1$ because there is almost no sensitivity of this integral characteristics within the interval of smaller γ ($\gamma = 0.02 - 0.1$). The PO sum (129) for the level density converges with the averaging width $\gamma = 0.2$ of a fine resolution of the shell structure as well as the shell-correction energy PO sum (137) by taking into account almost the same major simplest POs of a smaller action (scaled period τ_{PO}). For the shell-correction energy at the value 6.0 far from the short-time bifurcating POs, one finds also a good agreement with the both quantum and SSPM results, as for density calculations, cf. Figs. 14 and 17, with Fig. 19. As seen from Fig. 20, we obtain a nice agreement between the semiclassical (ISPM, dashed) and quantum (QM, solid) results at a bifurcation, too. Again, the dominating contribution in the semiclassical results for δU [(136) and (137)] at the bifurcation point 7.0 (Fig. 20) give the bifurcating newborn triangle-like (3,1) POs at $\alpha = 7.0$ together with other newborns (5,2), (7,3) and (8,3) which appear at smaller bifurcation values of α_{bif} (and exist for $\alpha \geq 7.0$) are obviously dominating (cf. lower panels (b) in these Figures).

A nice beating seen in these figures [13–20] is explained by the interference of the leading POs. The bifurcating orbits with the simple diameters of the same order in magnitude but with different phases are responsible for such a beating at the bifurcation points [16–18], and 20]. The ISPM contributions of diameters are close to the SSPM asymptotic ones near the bifurcation points $\alpha = 7$ and 4.25 and in between (e.g. at $\alpha = 6.0$), because they are far away from their symmetry-breaking point at the harmonic-oscillator value $\alpha = 2$.

V. DEFORMED SHELL STRUCTURES AND PERIODIC ORBITS IN THE POWER-LAW POTENTIAL

A. The power-law potential model

In Section III, the deformed shell structure is investigated by using the nuclear fission-cavity model with the potential having the sharp infinite walls. As shown in Section IV, this model corresponds to the $\alpha \rightarrow \infty$ limit of the radial power-law potential (PLP) model. In this

section, we consider a more realistic mean-field PLP by taking the finite values of α for the deformed Fermi systems. We shall investigate the changes of the shell structures with various types of deformations, and examine their relation to the periodic orbits, focusing especially on the role of the periodic-orbit bifurcations.

The general deformed PLP, up to a constant, can be expressed as

$$V(\mathbf{r}) = V_0 \left(\frac{r}{R_0 f(\theta, \varphi; \boldsymbol{\beta})} \right)^\alpha. \quad (141)$$

The function f describes the shape of the equi-potential surface $V(\mathbf{r}) = E$ as

$$r = R(\theta, \varphi; \boldsymbol{\beta}, E) \quad (142)$$

with the effective-surface profile function R in the spherical coordinates,

$$R(\theta, \varphi; \boldsymbol{\beta}, E) = (E/V_0)^{1/\alpha} R_0 f(\theta, \varphi; \boldsymbol{\beta}), \quad (143)$$

where $\boldsymbol{\beta}$ represents the set of deformation parameters. Imposing the conservation of the volume bounded by an equi-potential surface (142) at a given energy E with increasing the deformation from the spherical ($f = 1$) to the deformed [$f = f(\theta, \varphi; \boldsymbol{\beta})$] shape with the deformation parameters $\boldsymbol{\beta}$, the shape profile function f should be normalized to satisfy the equation:

$$\frac{1}{4\pi} \int_0^{2\pi} d\varphi \int_0^\pi d\theta \sin \theta f^3(\theta, \varphi; \boldsymbol{\beta}) = 1. \quad (144)$$

The scaling relation discussed in Section IV is valid independently of the function f . In the following, we shall investigate the deformed shell structures in the PLP versus those in spheroidal cavity.

For the Fermi PLP system with a tetrahedral-like deformation, as a simple and non-trivial exemplary case, the emergence of an unexpectedly strong shell effect at a large deformation with a suitable diffuseness [power parameter α in the PLP (141)] will be shown too in this Section. A study of the anomalous shell effects, and their semiclassical origin with focusing on the role of the periodic-orbit bifurcations will be presented in two next sections.

B. Prolate-oblate deformations

First, we examine the effect of spheroidal deformations in the PLP, and discuss the origin of the asymmetry between the deformed shell structure in the prolate (cigar-like) and the oblate (pan-cake-like) sides.

The deformed shell structures are quite different in the HO potential having a soft surface, and the cavity potential with a sharp surface. The valley lines of the shell-correction energy minima in these potentials have the opposite slopes in the plane of the deformation and particle number for the prolate case at small deformations. As explained in Section III, any valley can be associated with a few constant-action lines of the dominant classical periodic orbits with close (slightly different) actions. Using the scaling rule for the action integral, $S_{PO} = \hbar \tau_{PO} \mathcal{E}$

[see, e.g., (48)], one can present the constant-action condition (43) in a more explicit form:

$$\mathcal{E}_F = \frac{2\pi(n + \frac{1}{2} + \frac{\mu_{\text{PO}}}{4})}{\tau_{\text{PO}}(\beta)} \quad (145)$$

with

$$N \approx \int_0^{\mathcal{E}_F} \mathcal{G}_{\text{ETF}}(\mathcal{E}) d\mathcal{E} = \frac{1}{3} c_0 \mathcal{E}_F^3 + c_1 \mathcal{E}_F. \quad (146)$$

In the second equation, the ETF level density \mathcal{G}_{ETF} was approximated by that for the spherical shape (132).⁵ Equations (145) and (146) give the parametric representation for the constant-action lines in terms of the particle number N as function of the deformation parameters β (η for spheroidal cavity or c for more realistic parametrization of a cavity in Section III) through the Fermi energy \mathcal{E}_F . Strutinsky et al. have shown that the valleys under the consideration (Section III) are successfully explained by the constant-action lines of the dominant classical periodic orbits within the spheroidal-cavity model of the nucleus [5]. In the HO model, a two-parametric family of the shortest POs in the equatorial plane makes the dominant contribution to the periodic-orbit sum (18) for the shell-correction energy δU . Their periods become smaller with increasing prolate deformation, and the valley lines have a positive slope while the two-parametric meridian-orbit family (triangles, quadrangles, ...) play the dominant role in the spheroidal cavity potential for small deformations. Their lengths become larger with increasing prolate deformation and the slopes of the valleys are negative [8, 62].

As shown in Section III for the case of a fission-cavity model, the valleys of the constant-action minima change their slope sign to be positive with increasing deformation (at $c \approx 1.3$ in Fig. 7) because the dominant contributors become shorter equatorial orbits as approaching closer to the necking deformation where they encounter the bifurcation. At these deformations, such bifurcations are responsible for the enhancement of the shell structure through the additional local minima along the basic growing valleys. As noted in Section III and discussed in [8], to some extent, it is similar to the shell structure enhancement in the spheroidal cavity. In case of spheroidal cavity, with increasing deformation, the dominant contributors become the 3D POs which bifurcate from the second repetitions of equatorial orbits around the shape with the axis ratio nearly 2:1, and form pronounced superdeformed shell structures [8, 61, 62].

On the other hand, the issue of prolate-oblate asymmetry is relevant to the shell structures in normal (small-to-medium) deformation regions. In the HO model, slopes of the shell-energy valleys are similar in both prolate and oblate sides. For the spheroidal cavity model,

however, Frisk noticed [97] that the above-mentioned valleys along the constant-action lines of meridian orbits are found to be approximately flat in the oblate-deformation side. Due to this flatness, the gross-shell effects at the oblate deformations is similar to those for the spherical state, and systems will find favorable shapes in the prolate-deformation side when the particle numbers depart from their spherical magic values. This can be regarded as the origin of the famous prolate-shape predominance in the nuclear ground-state deformations.

Here, we are going to generalize Frisk's idea to a more realistic PLP model with spheroidal deformations. In this model, surface diffuseness is controlled by the power parameter α , and one can study the dependence of the deformed shell structure on the surface diffuseness by taking different values of α . The shape function f for the spheroidal deformation is given by

$$f(\theta, \varphi; \delta) = \frac{1}{\sqrt{e^{-4\delta/3} \cos^2 \theta + e^{2\delta/3} \sin^2 \theta}}, \quad (147)$$

where the deformation parameter δ is related to the axis ratio $\eta = R_z/R_\perp$ by $\eta = e^\delta$. This definition of the deformation parameter is useful because one finds the same set of meridian orbits with the same absolute value $|\delta|$ in both the prolate ($\delta > 0$, or $\eta > 1$) and the oblate ($\delta < 0$, $\eta < 1$) shapes.

The spheroidal shapes does not seem to be realistic in the description of nuclei with very large deformations while the gross-shell structures in the normal quadrupole deformation region are not much sensitive to the details of the shape parametrization. For the comparison, one can take a popular axially-symmetric quadrupole deformation with the shape function

$$f(\theta, \varphi; \beta_2) = \frac{1}{(1 + \frac{2}{5}\beta_2^2 + \frac{2}{35}\beta_2^3)^{1/3}} \times (1 + \beta_2 P_2(\cos \theta)). \quad (148)$$

Figure 21 displays the difference of quadrupole and spheroidal shapes. These shapes are close at small deformations while, at large ones, they are essentially different because of the formation of the neck in the case of a quadrupole shape. The necking plays important role in shell structures at large deformations, e.g., in nuclear fission [10] whereas, as usual, it is not so critical in the case of normal deformations. In Fig. 22, we compare the level diagrams for the spheroidal and axially-symmetric quadrupole deformations. These two diagrams have the resemblance and difference with each other, which can be understood from the semiclassical point of view as we shall discuss below.

Classical dynamics in a quadrupole-shape potential at a finite deformation is much more chaotic than that in the spheroidal-shape potential because of the negative curvature of the potential surface, although these two PLP Hamiltonians are both non-integrable. Let us look first at the Poincaré surface of Section to observe the chaoticity of the classical motion. Figure 23 shows the PSS for the shapes given in Fig. 21. Phase space is mostly covered with a tori for the spheroidal shape, while the large part of the phase space is filled with a chaotic sea for the quadrupole shape. Reflecting a strongly chaotic nature of the classical motion,

⁵ The coefficient c_0 in the leading term is independent of the shape under the volume conservation condition. The coefficient c_1 in the next-order term depends on the deformation, but in practice, its influence on the basic shell-structure properties is almost negligible at leading order terms.

the single-particle levels show their remarkable avoided crossings (level repulsions) at a large quadrupole deformation. However, the gross-shell structures in the two level diagrams look quite similar. This might be related to the short periodic orbits which have the dominant contribution to the gross-shell structure. Figure 24 shows some short meridian orbits in the potential (141) with both (147) and (148) for the profile function f . One may find a quite similar set of POs in these potentials. Hence, we adopt the spheroidal shape parametrization in order to understand the gross-shell structures in deformed nuclei through the quantum-classical correspondence in a simple way.

In the axially-symmetric deformed HO limit ($\alpha = 2$) with a generic irrational frequency ratio, all the equatorial orbits are periodic, and they form the two-parametric degenerate families. Another periodic orbit is the isolated diameter along the symmetry axis. At deformations with a rational (resonance) ratio, all the three-dimensional (3D) orbits become periodic, and they are created from the corresponding EQ POs as the four-parametric degenerate families. Let us now consider the system with the power parameter α at a value slightly larger than 2. At the spherical shape, only the diameter and circular POs are remaining to be periodic. With increasing spheroidal deformation, the equatorial and meridian branches cross with each other. In the HO limit, it corresponds to the resonance ratios and families of POs with higher degeneracy are found there. For $\alpha > 2$, one finds no such families but new *bridge orbits* in place of them [83].

Figure 25 shows the scaled period τ of some shortest periodic orbits as function of the deformation parameter δ for the power parameter $\alpha = 3.0$. With increasing δ deformation through the spherical shape ($\delta = 0$), one of the diameter orbits in the equatorial plane, say MX (M stands for the repetition number), bifurcates into itself (long-dashed), and a meridian (thick solid and dotted curves) PO ($M, 1, M'$) at one of the successive bifurcation points marked by heavy dots.⁶ Equatorial polygon-like orbits can also encounter a bifurcation at a certain deformation where they are parents for the newborn 3D bridge orbits. (These orbits are disregarded for simplicity from Fig. 25.) Then, e.g., the meridian PO exists up to the deformation where it submerge into a diameter $M'Z$ (in general, M' can be different from M). This might be also considered as a bifurcation in the opposite direction of the deformation change, namely, when the diameter $M'Z$ bifurcates into itself and the meridian PO ($M, 1, M'$) with decreasing the deformation. Therefore, such a meridian (or 3D) PO, which exists only between the two deformations (bifurcation points) δ and connects for instance the equatorial X diameter (at a smaller deformation) and the MZ diameter along the symmetry axis (at a larger one) PO, can be transparently called as the “*bridge orbit*” [83]. In the PLP model, all the equa-

torial polygon-like POs encounter a bifurcation with increasing the deformation δ , and the new-born meridian, or 3D orbits, make bridges between the equatorial and MZ POs. According to the general POT (Section II), the shortest POs give the most important contributions into the averaged level density (16) and shell-correction energies (18). Moreover, according to the general arguments of the ISPM (Section IIB, III and IV for the specific examples), the amplitudes of the oscillating level density are usually enhanced by the shortest bridge orbits due to their bifurcations [8]. These bridge orbits play a significant role in the deformed shell structure. Superdeformed and hyperdeformed shell structures are associated with the 2:1 and 3:1 bridge-orbits between the 2nd and 3rd repetitions of equatorial orbits and a primitive symmetry-axis orbit Z, respectively. With increasing oblate deformation $|\delta|$, each repeated symmetry-axis orbit encounters the bifurcation with emerging a new bridge orbit, in addition to the parent one, and this bridge orbit is submerged into a certain repeated equatorial orbit at larger $|\delta|$. For the normal deformation region, the most important orbit is the meridian family C which makes a bridge between the primitive equatorial diameter family X in the oblate, and the isolated primitive symmetry-axis diameter orbit Z in the prolate deformation side.

Figure 26 shows the scaled periods of the orbits C, X and Z, which participate in a bridge-orbit bifurcation scenario for some three different values of the power parameter α . For α close to 2, the bridge orbits exist in a very small range of deformations. They travel from the orbit X to Z with only a small change of the deformation, and along their paths in the phase space a family of approximately periodic (quasi-periodic) orbits should be formed. It yields a coherent contribution into the trace integral because of a local effective increase of the phase-space region of more exact integration, that leads, in the semiclassical approximation through the ISPM, to an enhancement of shell effect (Section II, see also Sections III and IV for the specific examples). In the case of the bridge-orbit bifurcations, such a quasi-periodic family acquires approximately an extra degeneracy along the trail of a bridge orbit in between its emerge and submerge deformations, and one will observe in between a more pronounced shell structure enhancement. For the spherical PLP with α slightly larger than 2, the existence of such a quasi-periodic family with the increased degeneracy between the two bifurcation points, in contrast to a local family which is localized at the single bifurcation for a non-integrable Hamiltonian system in the symmetry z axis plane (or in the HO potential with commensurable frequencies) (Section III and [72]), is associated with a weak breaking of the SU(3) symmetry. This is also much in contrast to the PO family which appears at the single bifurcation point and exists for all larger deformations in the integrable (e.g., spheroid cavity and RPLP) systems, see [8, 62] and Section IV. Generally speaking, the emergence of such bridge orbits might be considered as a deep classical sign of the restoration of a certain dynamical symmetry, increased in a finite deformation region in comparison with the local family case discussed in Section III. As α increasing apart from 2, the range of the

⁶ The 3D orbit (M_R, M_φ, M_z) is labeled by the numbers of oscillations (rotations) in the directions of cylindrical coordinates (R, φ, z) with the symmetry z axis.

bridge orbit becomes wider, and the quasi-periodic orbits only exist around both ends of the bridge, where the pronounced shell effect might be observed.

In order to find a quantum-classical correspondence in the deformed shell structures, we compare the Fourier transform of the quantum scaled-energy level density (139) with the scaled periods of the classical POs. Figure 27 displays the Fourier amplitude $|F(\tau; \delta)|$ plotted in the (δ, τ) plane. The scaled periods τ_{PO} of the classical periodic orbits are also plotted as functions of δ . As shown in this Figure, the Fourier amplitude (139) is concentrated along the classical POs and takes especially large values around the bifurcation points of the bridge orbits. Since the gross-shell structure is dominated by the shortest periodic orbits, the primitive bridge orbit C is expected to play the dominant role in the shell structure of nuclei at normal deformations.

Figure 28 shows the contour plot of the shell-correction energies as functions of the deformation δ , and the particle number N . The regular-energy valleys running along the constant-action lines of the bridge orbit C can be observed for $|\delta| \lesssim 0.4$. As clearly seen from this Figure, the contribution of the bridge orbit to the semiclassical shell-correction energies is dominant in a normal deformation region. Since the slopes of the constant-action lines are steep in the right prolate side while they are rather flat in the left oblate one (in accordance with the valleys), the nucleus apart from the spherical magic numbers cannot find the energetically favorable shape in the oblate side. Thus, this isomer shape will tend to be deformed towards the prolate deformation. Obviously, this clearly explains the origin why the prolate-shape is dominant in the nuclear ground-state deformations, in line of the spheroidal-cavity case analyzed by Frisk [97].

The origin of the prolate-shape dominance is also considered by Hamamoto and Mottelson from another point of view [98]. They are focusing on the asymmetric manners of the level splittings in the prolate and oblate deformation cases, and discuss the reason of such an asymmetry. In their model, the spin-orbit coupling was neglected. Tajima et al. have shown that the feature of the prolate-shape dominance is quite sensitive to the spin-orbit coupling [99, 100]. In this sense, our present explanation of basic features of the prolate-shape dominance, without the spin-orbit coupling, is preliminary. The final analysis should be based on a more realistic model with accounting for the spin-orbit coupling for a deep understanding of this long-standing problem in nuclear structure physics whose semiclassical study is in progress [86, 101].

C. Tetrahedral deformed shell structures

Breaking the reflection symmetry, one can also find an exciting subject useful for the nuclear-structure physics [102]. As shown in [102], such a symmetry breaking is experimentally observed through, for instance, the collective low-lying negative-parity states or parity-doublet rotational spectra. It is also significant for describing the asymmetric fission process as discussed in Section III. In the octupole deformation space, there are the 4

types of the octupole deformations. In this subsection, the change of shell structures with respect to octupole shapes and surface diffuseness will be discussed from the semiclassical viewpoint.

With a large octupole deformation, the equi-potential surface has negative curvatures as for a large quadrupole deformation (Section VB), and the classical orbits become chaotic. Significance of the flexible deformed shapes for a deep understanding of the nuclear structure and dynamics were emphasized many times by Strutinsky et al. [5, 8, 10] and Swiatecki et al. [103–105] in different aspects: The nature of the fission isomer shapes and order-chaos transitions from spheroidal (or quadrupole) to the Legendre polynomial high-multipole shapes of the cavity models versus the same but within the quantum-mechanical approach using the realistic deformed Woods-Saxon (WS) potential with the finite surface diffuseness, respectively. Taking their good ideas to use simple analytical approaches (e.g., without the spin-orbit interaction but within the mean-field approximation for understanding the major properties of the shell structure, and chaoticity of the adiabatic to the non-adiabatic nucleon dynamics with increasing the shape multipolarity in heavy deformed nuclei), one should emphasize the diffuseness of the mean-field potentials. Together with other additional degrees of freedom (spin-orbit interaction, for instance), they lead to some new symmetry-breaking and bifurcation phenomena. According to the general semiclassical ISPM arguments (Section IIB), these phenomena are associated with the enhancement of the shell structure, even in the case of a very chaotic nucleon motion inside of a complicate non-integrable shape. This seems to be in contrast to the results expected from [104, 105], however, for the adiabatic approximation. The diffuseness of the mean-field potentials was underestimated in the works [5, 8] supporting the cavity models with realistic surface shapes, too. But, in some another sense that there is no increasing much chaoticity with complexity of the deformed shapes, our results turn to be more in line of [5, 8, 10, 83].

In spite of the chaoticity in internal classical dynamics, it is suggested in several works that the system with Y_{32} -type shape provides a remarkable shell effect at finite deformations [106–109]. To see the case where such enhancement of gross shell effect is especially pronounced, we shall examine now the special-shape parametrization which smoothly connects the sphere and tetrahedron under variations of a single deformation parameter β_{td} . The shape function f of (141),

$$f(\theta, \varphi) = \tilde{f}(\theta, \varphi) \times \left[\frac{1}{4\pi} \int_0^{2\pi} d\varphi' \int_0^\pi d\theta' \sin \theta' \tilde{f}^3(\theta', \varphi') \right]^{-1/3}, \quad (149)$$

can be expressed in terms of an auxiliary function \tilde{f} . This function is given by the largest positive root \tilde{f} of the following quartic equation [110]:

$$\tilde{f}^2 + \frac{\beta_{\text{td}}}{2} \left\{ 1 + u_3(\theta, \varphi) \tilde{f}^3 - u_4(\theta, \varphi) \tilde{f}^4 \right\} = 1, \quad (150)$$

where

$$u_3 = \frac{4}{15} P_{32}(\cos \theta) \sin 2\varphi, \quad (151)$$

$$u_4 = \frac{1}{5} + \frac{4}{5}P_4(\cos\theta) + \frac{1}{210}P_{44}(\cos\theta) \cos 4\varphi.$$

Both functions u_3 and u_4 are invariants under all the symmetry transformations which define a tetrahedral T_d group. The solution \tilde{f} of the equation (150) possesses the same symmetry for any value of β_{td} . Equation (149) for the shape function f satisfies the volume conservation condition (144), as a scaling of the function \tilde{f} . For $\beta_{td} = 0$, one obtains the equi-potential surfaces of the spherical shape ($f = 1$) while, at $\beta_{td} = 1$, one finds those of the shape of tetrahedron. Hence, the transition of the shell structures from the sphere to the tetrahedron can be examined by changing the single tetrahedral-deformation parameter β_{td} continuously from 0 to 1. The shapes of the equi-potential surface at several values of β_{td} are displayed in Fig. 29. The T_d symmetry group consists of the 24 symmetry transformations: The three-fold rotations around the four C_3 axes (there are 8 such transformations); the four-fold rotatory reflections around the three S_4 axes (6 transformations); the two-fold rotations around the C_2 axes, equivalent to the S_4 axes, (3 ones); the reflections about the six symmetry planes σ_d (6 ones); and finally, in addition, the identity (one). This group has five irreps (irreducible representations); the two 1D irreps (A_1, A_2), one 2D irrep (E), and two 3D irreps (F_2, F_1). The quantum levels can be classified in terms of these five irreps. The levels belonging to the n -dimensional irrep have the n -fold degeneracy, and thus, the quantum energy spectrum in the potential with the T_d symmetry generally contains levels with the three-fold degeneracy.

In addition to these geometric degeneracy properties, Hamamoto et al. have found that the Y_{32} deformed system shows a quite strong gross-shell effect as compared to other types of the octupole shapes [106]. With our shape parametrization which connects the sphere and the tetrahedron, one obtains a significantly pronounced shell effect arising at a large tetrahedral deformation. This effect might be related to the stabilities of classical periodic orbits. As shown in Fig. 29, the equi-potential surface for the current shape parametrization (149) is convex everywhere, and the classical trajectory is more stable than in the case of a pure Y_{32} shape.

Figure 30 shows the single-particle level diagram for two values of the power parameter $\alpha = 4.0$ and 6.0 , where the scaled-energy levels $\mathcal{E}_i = (E_i/V_0)^{1/2+1/\alpha}$ are plotted as functions of the tetrahedral parameter β_{td} . One finds the prominent shell effect at a large tetrahedral-like deformation $\beta_{td} \approx 0.6$ and 0.7 for $\alpha = 4.0$ and 6.0 , respectively. It is extremely interesting that the deformed magic numbers are exactly found to be equivalent to those of the spherical harmonic oscillator at such large tetrahedral-like deformations. According to the POT (Section IIB), these HO magic numbers might be explained by the approximate symmetry restoration, specific to the bridge-orbit bifurcation. In a simple bifurcation, the formation of the local quasi-periodic family is limited to the vicinity of the single bifurcating PO, while, in the bridge-orbit bifurcation, the bridge PO family is traveling between the two POs which are close in the deformation but widely separated from each other in the

phase space. Therefore, because of increasing the phase space volume occupied by the bridge PO family, one can find a remarkable enhancement of the bridge PO amplitudes of the oscillating level density, in contrast to the case of simple local bifurcations.

Let us investigate the origin of the unexpectedly strong and regular shell effects which emerge at certain combinations of the surface diffuseness and large tetrahedral deformation. Figure 31 shows some short classical periodic orbits for $\alpha = 6.0$. There are the diameter- and the circle-orbit families in the spherical power-law potential ($\beta_{td} = 0$). With increasing β_{td} , each of these two families triplicate into the three branches. The diameter family triplicate into the linear orbit DA along the C_{2v} axis, the linear orbit DB along the C_3 axis, and the self-retracing planar orbit PA in the σ_d plane. The circle orbit triplicate into the 3D orbit TA having the S_4 and σ_d symmetries with respect to the two symmetry planes containing the common S_4 axis, the 3D TB having the C_3 symmetry, and the planar PB (in the σ_d plane) having the C_2 and σ_d symmetries as related to the two symmetry planes containing the common C_2 axis.

Figure 32 shows the scaled periods of some short periodic orbits as functions of the tetrahedral deformation parameter β_{td} . With increasing β_{td} , the scaled periods of the major four orbits gather around $\beta_{td} = 0.6$, and bifurcations take place almost at the same values of β_{td} . Some of the new-born periodic orbits are bridges between the two crossing orbits. As we discussed above, the emergence of these bridges is a good signature of the restoration of an approximate relatively high dynamical symmetry. A family of the quasi-periodic orbits are formed along the bridge orbits connecting some two distinct periodic orbits in the phase space, and hence, the dynamical symmetry is not localized to a single PO, in contrast to the single local bifurcation [110].

Figure 33 shows the Fourier amplitudes of the quantum scaled-energy level density, which are defined in (139), in the (β_{td}, τ) plane. Scaled periods τ_{PO} of some shortest classical POs are also plotted as functions of β_{td} in the same plane. As seen from this map, the Fourier amplitudes exhibit peaks along the classical periodic orbits, and show remarkable enhancement around the bifurcation points $\beta_{td} = 0.6 \sim 0.8$, where a strong shell effect appears in the quantum spectrum. Again, the gathering of POs and almost the isochronous occurrence of the bridge bifurcations among them can be associated with the restoration of an approximate high dynamical symmetry. As a conclusion, the latter is the origin of the anomalous properties of the shell structure for a large tetrahedral-like deformation. Recalling also the magic numbers equivalent to the spherical harmonic oscillator, one may relate the restored symmetry to that of the $SU(3)$ nature.

Since the tetrahedral-like deformed potential has no continuous symmetries, the Gutzwiller trace formula for the isolated orbits can be applied if all the significant periodic orbits are sufficiently apart from the bifurcation points. In order to compare with the quantum calculations, one can apply the Gutzwiller trace formula for the level density to the semiclassical shell-correction energy

(18) for a given deformation β_{td} ,

$$\delta U(\mathcal{E}_F) = 2 \left. \frac{dE}{d\mathcal{E}} \right|_{\mathcal{E}=\mathcal{E}_F} \times \quad (152)$$

$$\times \sum_{PO} \frac{A_{PO}}{\tau_{PO}^2} \cos\left(\tau_{PO}\mathcal{E}_F - \frac{\pi\mu_{PO}}{2}\right),$$

$$N(\mathcal{E}_F) = 2 \int_0^{\mathcal{E}_F} d\mathcal{E} [\mathcal{G}_{ETF}(\mathcal{E}) + \quad (153)$$

$$+ \sum_{PO} A_{PO} \cos\left(\tau_{PO}\mathcal{E} - \frac{\pi\mu_{PO}}{2}\right)],$$

$$A_{PO} \approx \mathcal{A}_{PO}^G = \frac{\tau_{PO}}{\pi \sqrt{|\det(\mathcal{M}_{PO} - I)|}}, \quad (154)$$

where \mathcal{G}_{ETF} is approximated by the spherical expression (132) (Section IVE1). Equations (152) and (154) provide the parametric representation for the function δU of N through the Fermi scaled energy variable $\mathcal{E}_F = (E_F/U_0)^{1/2+1/\alpha}$, where E_F is the Fermi energy.

The two bottom panels in Fig. 34 show the comparison between the quantum and semiclassical shell-correction energies for $\beta_{td} = 0.1$ and 0.5 . For $\beta_{td} = 0.1$, we take the main 6 shortest periodic orbits DA, DB, PA, PB, TA and TB. The gross structures are successfully described by the Gutzwiller trace formula. Some fine structures might be well approximated semiclassically by the proper treatment of longer periodic orbits. For $\beta_{td} = 0.5$, we include the contribution of the orbit TC, which emerges through the bifurcation of PB at $\beta_{td} = 0.28$, in addition to the six orbits mentioned above. The main oscillating pattern is reproduced well but the semiclassical formula generally overestimate the amplitude of the oscillations. A most probable reason of this discrepancy is that the deformation β_{td} becomes too close to one of the bifurcation points where the loss of accuracy of the standard stationary-phase approximation takes place because of the divergence of the Gutzwiller trace formula.

In the top panel of Fig. 34, we display the quantum shell-correction energies for $\beta_{td} = 0.7$. At this deformation, one finds the most pronounced shell effect with a very strong and regular oscillations in the shell-correction energy, which should be dominated by the bifurcating orbits having almost the same periods. Here, the standard stationary-phase method completely breaks down due to the dense bifurcations, and one cannot certainly apply the Gutzwiller trace formula. As shown in Section IIE, the ISPM is useful also to solve the bifurcation problem in a non-integrable system. Its application to the description of the anomalous behavior in the amplitudes of the oscillating level density and energy at large oblate-prolate and tetrahedral-type deformations should be an interesting and challenging future subject.

VI. CONCLUSIONS

In Section II we have given a short review of the semiclassical theory (POT) accounting for the PO bifurcations and symmetry breaking in different potential wells. A general trace formula for the oscillating level density was derived in the phase space variables (see also Appendix A2). Extensions of the POT to the treatment of the bifurcations and symmetry breaking was presented as the improved stationary phase method in close analogy with the catastrophe theory of Fedoriuk and Maslov,

and hereby, overcoming the divergence of the semiclassical amplitudes of the Gutzwiller theory and discontinuity of them in the Berry&Tabor approach at bifurcations. The improved semiclassical amplitudes within the ISPM typically exhibit an enhancement of the shell structure locally near a bifurcation and on right side of it where new orbits emerge which is of high order in the inverse semiclassical parameter, $1/\hbar$, with respect to the Gutzwiller trace formula amplitude for the isolated orbits. The PO expansions for the averaged level density and the shell-correction energy δU , and their PO convergence were shown too. The semiclassical trace formulae for δU exhibit a rapid convergence of the PO sum, due to an inverse dependence of the individual orbit contributions on the squares of their periods (actions), in addition to the phase-space volume and degeneracy symmetry factors of the oscillating level density. This allows one often to express significant features of the shell structure in terms of a few short periodic orbits. In many cases, the shortest POs are sufficient to describe the gross-shell features in δU . We have obtained an analytical trace formula for the oscillating part of the level density in the H  non-Helies Hamiltonian as a sum over periodic orbits in a non-integrable potential. It is continuous through all critical points, in particular here the harmonic oscillator limit at zero energy and the cascade of pitchfork bifurcations near the saddle energy. We find an enhancement of the semiclassical amplitudes near the most critical points. The numerical agreement with quantum results is good, in spite of a simple uniform ISPM approximation including only the simplest primitive periodic orbits. The quantum-classical correspondence for the chaos-order transitions is shown through the Poincar   surface of sections in the limit from the non-integrable region of the energies to the symmetry breaking point.

In Section III, we have presented a semiclassical calculation of a typical actinide fission barrier using the POT, employing a fission cavity model that uses a realistic description of the three principal axially-symmetric deformations (elongation, neck formation and left/right asymmetry) occurring in the (adiabatic) fission process. The characteristic double-humped barrier and, in particular, the sensitivity of the outer barrier to left/right-asymmetric deformations can be qualitatively well described by the POT. The loci of minimal quantum shell-correction energies δU , both in particle number vs. deformation space and in two-dimensional deformation space, are correctly followed by the constant-action loci of the shortest POs. Hereby we observe a clear signature of period-one bifurcations of the shortest equatorial orbits which were treated semiclassically using normal forms and uniform approximations.

We found that the local minima of the shell-correction energy calculated for the non-integrable (in the symmetry z axis plane) cavity potential with the realistic parametrization of the shapes of the fission cavity model [10] can be associated with the bifurcations of the POs at large deformations as for the spheroidal cavity [8, 62]. The quantum-mechanical Fourier spectra of the corresponding Hamiltonian exhibit a nice quantum-to-classical correspondence, in that the enhanced Fourier signals follow exactly the PO lengths of their semiclass-

sically enhanced amplitudes. This correspondence appears also in the correct description of the loci of large deformations in particle number vs. deformation space by the constant-action lines of the bifurcated period-two and -three orbits. An important reason for their strong enhancement at large deformations, in addition to the general argument given above (and explained in Sec. 2), is also the fact that the new bifurcated orbits have locally a larger classical degeneracy than their parent orbits and the period-one orbits ($\mathcal{K} = 1$) (except near the bifurcations).

In Section IV we presented a class of the radial power-law potentials, $V(r) \propto r^\alpha$, which up to a constant turn out as good approximations to the popular WS potential in the spatial region where the particles are bound. The advantage of the RPLP is that it is capable of controlling surface diffuseness, and in the same time, the classical dynamics scales with simple powers of the energy, that makes the POT calculations greatly easy. It can be done sometimes even explicitly analytically for $\alpha = 4$ and 6 (besides of the well-known HO case $\alpha = 2$) in terms of the simple special functions. The quantum Fourier spectra yield directly the amplitudes of the quantum level density in terms of periods (actions) of the leading classical POs.

We described the main PO properties of the classical dynamics in the RPLP as the key quantities of the POT. We developed semiclassical trace formulae for any power α of this potential and studied various limits of α (the harmonic oscillator potential for $\alpha = 2$ and the cavity potential for $\alpha \rightarrow \infty$). We presented a semiclassical theory of quantum oscillations of the level density and shell-correction energy for RPLPs. It is based upon extended Gutzwiller's trace formula in the convenient phase space variables which connects the oscillating component of the level density for a quantum system to a sum over POs of the corresponding classical system. This POT was applied to express the shell-correction energy of a finite fermion system in terms of POs. We obtained good agreement between the ISPM semiclassical and quantum results for the level densities and shell-correction at several powers of the PRLPs. For the power 6 we found also good agreement of the ISPM trace formulas with the SSPM ones far from the bifurcations of the leading short-time POs of a maximal degeneracy of the classical POs. The strong amplitude enhancement phenomena at a bifurcation point $\alpha = 7$ in the oscillating (shell) components of the level density and energy, due to the bifurcations, and on their right side, were remarkably agreed with the peaks of the Fourier spectra. We found a significant influence of bifurcations of periodic orbits on the main characteristics (oscillating components of the level densities and energy-shell corrections) of a fermionic quantum system. They leave signatures in its energy spectrum (visualized, e.g., by its Fourier transform), and hence, its shell structure.

The trace formulae are in good agreement with the quantum-mechanical level-density oscillations for gross- (larger averaging parameter γ and a few shortest POs) and fine-resolved (smaller γ and time-longer bifurcating POs) shell structures, also for the shell-correction energies independent of γ . We found a similar gross shell

structure in the shell-correction energies with the corresponding densities at $\gamma \approx 0.2$ for $\alpha \gtrsim 6$. The fine-resolved shell structures were found with the corresponding densities at $\gamma = 0.03 - 0.2$ for $\alpha \gtrsim 6$.

Section V is devoted to the extension of the semiclassical POT to a more realistic deformed Fermi systems with their surface diffuseness by using scaling of the power law potentials (PLP) from the RPLP to the superdeformed shapes. We may state that the POT is well capable of explaining the main features of quantum shell structure in terms of a few short classical POs for such deformed PLPs. Bifurcations of POs are not simply an obstacle of the semiclassical theory, but they leave clear signatures both in the quantum Fourier spectra and the locations of minima of the shell-correction energy δU plotted versus particle number and potential parameters such as the power (potential surface diffuseness) and the deformation parameter. As examples of the deformed PLP with the surface diffuseness, we have discussed in Sec. 5 the prolate-oblate asymmetry in shell structures for the quadrupole-type deformations, and anomalous enhancement of shell effects at reflection-asymmetric deformations with the tetrahedral symmetry. In the both cases, the bifurcations of bridge orbits, play the significant role in enhancement of the shell effect through approximate restorations of the dynamical symmetry which depends essentially on the certain combinations of the diffuseness (power) and deformation parameters. Especially, in the latter case of the tetrahedral deformation, one finds unexpectedly remarkable enhancement of the shell effect. It might be explained by the formations of the short bridge PO families: If the two bifurcation points, corresponding to the two ends of the bridge, are close to each other, such PO families are formed along the path of the bridge connecting the two widely separated (in the phase space) POs. These bridge families should occupy larger phase-space volumes as compared to the cases of a simple local bifurcation. Thus, these specific bridge-orbit bifurcations might be responsible for the significant influence on the shell structure in a quantum deformed Fermi system with a finite diffuse edge.

In our future work we intend to further study finer shell structures due to longer orbits, applying both the ISPM and uniform approximations to treat their bifurcations [7, 60, 111]. In particular, we want to understand the “quantization” into isolated minima that occurs along the valleys of both the ground-state and the secondary (isomer) minima and, in particular, we want to better understand the superdeformed shell structure taking into account the diffuseness of the mean-potential edge. In the region of superdeformation in the spheroidal cavity, we found clearly that this is due to the bifurcated period-two and -three orbits. It will be interesting to study the analogue situation in the fission cavity model by investigating the higher-period bifurcations occurring there. One complication in that model is that we have to vary three deformation parameters (c, h, α), instead of only one ($\eta = c^{3/2}$) for the spheroid, in order to fully cover the fission barrier landscape. This will naturally lead to a much larger variety of possible bifurcations. Another object of our studies will be to understand semiclassically the transition regions be-

tween the down-going ground-state valleys and the initially up-going secondary-minimum valleys. They are well described separately by the shortest meridional and equatorial orbits, respectively, but in the transition regions ($1.2 \lesssim c \lesssim 1.35$ and $1.2 \lesssim \eta \lesssim 1.5$, respectively) we expect further bifurcations and corresponding new orbits to play a role. We want to apply the ISPM for deeper studying the enhancement of the shell structure in the PLP due to the new bridge-orbit bifurcations.

On a longer time scale, we intend also to include pairing and spin-orbit interactions into the POT calculations, in order to come closer to a realistic description of nuclei, and to extend the POT towards the collective dynamics [112–114]. We would like to study within the POT the shell corrections to the transport coefficients, such as the inertia, friction [53–57]; and moments of inertia [30–33] for the nuclear collective dynamics, see also [115] for the self-consistency and spin effects included into the ETF component of the moments of inertia. We would like also to extend the POT to the two-component (neutron-proton) Fermion systems as atomic nuclei, see [116–123] for the ETF approach. Our semiclassical analysis may therefore lead to a deeper understanding of the shell structure effects in finite fermionic systems such as nuclei, metal clusters or semiconductor quantum dots whose conductance and magnetic susceptibilities are significantly modified by shell effects.

ACKNOWLEDGMENTS

Authors gratefully acknowledge Ch. Amann, M. Brack, S. N. Fedotkin, F. A. Ivanyuk, Ya. D. Krivenko-Emetov, M. Matsuo, K. Matsuyanagi, A. I. Sanzhur, K. Tanaka and E. E. Saperstein for fruitful collaborations and many useful discussions. One of us (A.G.M.) is also very grateful for a nice hospitality during his working visits of the University of Regensburg in Germany, and Physical Department of the Nagoya Institute of Technology, also the Japanese Society of Promotion of Sciences for the financial support, ID No. S-14130.

Appendix A

A1. TO CLASSICAL DYNAMICS FOR THE RPLP

For any spherical potentials $V(r)$ the Hamiltonian $H(\mathbf{r}, \mathbf{p})$ (21) in the spherical canonical phase-space variables $\{r, \theta, \varphi, p_r, p_\theta, p_\varphi\}$, one has the dynamical equations:

$$p_r(r) \equiv \sqrt{2m[E - V(r)] - \frac{L^2}{r^2}} = m\dot{r}, \quad (\text{A.1})$$

$$\dot{\theta} \equiv \frac{L}{mr^2} \equiv \frac{L}{r^2 p_r} \dot{r}.$$

As the angular momentum L is conserved for a motion of the particle in a central field $V(r)$, all CTs are lying in a plane crossing the center $r = 0$. Therefore, the third equation for $\varphi(t)$, additional to (A.1), is identity $\varphi = \theta$, and the two other equations (A.1) can be considered in an azimuthal plane $\varphi = \text{const}$. As the Hamiltonian (21)

expressed through the spherical action-angle variables does not depend on the angles, i.e., they are cyclic, the frequencies are constants given by

$$\omega_r = \partial H / \partial I_r = (\partial I_r / \partial E)^{-1} = \quad (\text{A.2})$$

$$= \left(\frac{m}{\pi} \int_{r_{\min}}^{r_{\max}} \frac{dr}{\sqrt{2m[E - V(r)] - L^2/r^2}} \right)^{-1},$$

$$\omega_\theta \equiv \omega_\varphi = -(\partial I_r / \partial L) / (\partial I_r / \partial E),$$

where $I_r = I_r(E, L)$ is the surface energy in (24). Thus, the PO equation takes the form of the resonance condition (26). The energy surface $I_r = I_r(E, L)$ is simplified to a function of one variable L for a given energy E of the particle because the second equation for the ratio of frequencies $\omega_\theta / \omega_\varphi = 1$ is identity [$I_\theta = L$ for $L_z = 0$, see (24)].

Integrating the differential equations in (A.1), one obtains the radial trajectory $r = r(t)$ and the angle $\theta(r)$ in an azimuthal plane. For one period $t = T$ along the PO at $\Theta = \Theta''$ ($r = r''$), one has (23). In order to derive the relation (23), one can use (A.2) for the definition of frequencies ω_θ and ω_r through the classical Hamiltonian H , and the Jacobian properties for the frequency ratio ω_θ / ω_r in an azimuthal plane ($I_\theta = L$ for $I_\varphi = L_z = 0$):

$$\frac{\omega_\theta}{\omega_r} = \frac{D(H, I_r)}{D(I_\theta, I_r)} \frac{D(I_r, I_\theta)}{D(H, I_\theta)} = \quad (\text{A.3})$$

$$= - \left(\frac{\partial I_r}{\partial L} \right)_{H=E}.$$

A2. SEMICLASSICAL DERIVATION OF THE PHASE SPACE TRACE FORMULA

For the derivation of the phase-space trace formula (1) we start with the definition of the level density $g(E)$ as the trace of Green's function $G(\mathbf{r}', \mathbf{r}'', E)$ in the Cartesian coordinates [75, 77, 78],

$$g(E) = -\frac{1}{\pi} \text{Im} \int d\mathbf{r}'' \int d\mathbf{r}' G(\mathbf{r}', \mathbf{r}'', E) \times \quad (\text{A.4})$$

$$\times \delta(\mathbf{r}'' - \mathbf{r}') = -\frac{1}{\pi(2\pi\hbar)^D} \text{Im} \int d\mathbf{r}'' \int d\mathbf{r}' \int d\tilde{\mathbf{p}} \times$$

$$\times G(\mathbf{r}', \mathbf{r}'', E) \exp \left[\frac{i}{\hbar} \tilde{\mathbf{p}}(\mathbf{r}' - \mathbf{r}'') \right].$$

The Fourier representation of $\delta(\mathbf{r}' - \mathbf{r}'')$ was used in these derivations. For any fixed integration variables, one has the single CT, and therefore, according to [3, 70], we can apply the standard Gutzwiller's expression for the Green's function related to the isolated paths CT [1, 7],

$$G_{\text{scI}}(\mathbf{r}', \mathbf{r}'', E) = 2\pi (2\pi i \hbar)^{-(D+1)/2} \times \quad (\text{A.5})$$

$$\times \sum_{\text{CT}} |\mathcal{J}_{\text{CT}}(\mathbf{p}' t_{\text{CT}}, \mathbf{r}'', E)|^{1/2} \times$$

$$\times \exp \left[\frac{i}{\hbar} S_{\text{CT}}(\mathbf{r}', \mathbf{r}'', E) - \frac{i\pi}{2} \mu_{\text{CT}} \right].$$

Substituting this approximate expression for the Green's function into the second equation of (A.5) we calculate the integral over \mathbf{r}' by the SPM extended to the continuous symmetries. The stationary phase conditions for the integration over the parallel y' and perpendicular

$\mathbf{r}'_{\perp} = \{x', z'\}$ components of \mathbf{r}' in the 3D case (x' in the 2D Fermi system) are given by

$$\left(\frac{\partial S_{\text{CT}}}{\partial y'}\right)^* = -\tilde{p}_y, \quad \rightarrow \quad p_y'^* = \tilde{p}_y, \quad (\text{A.6})$$

$$\left(\frac{\partial S_{\text{CT}}}{\partial \mathbf{r}'_{\perp}}\right)^* = \tilde{\mathbf{p}}_{\perp}, \quad \rightarrow \quad \mathbf{p}'_{\perp} = \tilde{\mathbf{p}}_{\perp}.$$

Taking the integral over the perpendicular coordinates \mathbf{r}'_{\perp} by the SSPM with the second equation in (A.7) for the stationary points $(\mathbf{r}'_{\perp})^*$, one notes that the first equation for the stationary values of the parallel component y' is the identity. Using the expansion of the action in $y' - y''$ up to the main linear term, and keeping the zero order terms of the pre-exponent factors, we obtain the Fourier integral, which leads to the energy-conservation δ -function,

$$\frac{1}{2\pi\hbar} \int dy' \exp \left[\frac{i}{\hbar} (p - p'_y) (y' - y'') \right] = \delta(p - p'_y) = \frac{p}{m} \delta(E - H(\mathbf{r}', \mathbf{p}')) . \quad (\text{A.7})$$

Applying the Hamilton-Jacobi equations,

$$H(\mathbf{r}', \mathbf{p}') = E, \quad H(\mathbf{r}'', \mathbf{p}'') = E, \quad (\text{A.8})$$

for the calculation of derivatives in the Jacobian $\mathcal{J}_{\text{CT}}(\mathbf{p}', ; t_{\text{CT}}, \mathbf{r}'', E)$ of the semiclassical Green's function (A.5) and using the standard Jacobian transformations, one has [1, 3]

$$\mathcal{J}_{\text{CT}}(\mathbf{p}', t_{\text{CT}}; \mathbf{r}'', E) = - \left(\frac{m}{p} \right)^2 \mathcal{J}_{\text{CT}}(\mathbf{p}'_{\perp}, \mathbf{r}'_{\perp}). \quad (\text{A.9})$$

With further applying the standard Jacobian transformations,

$$\frac{\mathcal{J}(\mathbf{p}'_{\perp}, \mathbf{r}'_{\perp})}{\mathcal{J}(\mathbf{p}'_{\perp}, \mathbf{r}'_{\perp})} = \mathcal{J}(\mathbf{p}'_{\perp}, \mathbf{p}'_{\perp}), \quad (\text{A.10})$$

for the constant $\mathbf{r}'_{\perp} = \mathbf{r}'_{\perp}^*$, one finally arrives at the phase space trace formula (1).

We need also the relation between generating functions Φ_{CT} and \hat{S}_{CT} (Section IIF),

$$\Phi_{\text{CT}} = \hat{S}_{\text{CT}} - \mathbf{p}'(\mathbf{r}' - \mathbf{r}''). \quad (\text{A.11})$$

where

$$\hat{S}_{\text{CT}}(\mathbf{r}'', \mathbf{p}'; E) = S_{\text{CT}}(\mathbf{r}', \mathbf{r}''; E) + \mathbf{p}'\mathbf{r}'. \quad (\text{A.12})$$

A3. SCALING AND UNITS

For convenience, let us consider classical dynamics in terms of the energy \overline{E} , action \mathcal{I}_i , angular momentum Λ , radial coordinate \bar{r} and frequency $\bar{\omega}_r$ and curvature \bar{K} in dimensionless units,

$$\overline{E} = E/V_0, \quad \mathcal{I}_i = I_i/\sqrt{mR^2V_0}, \quad (\text{A.13})$$

$$\Lambda = L/\sqrt{mR^2V_0},$$

$$\bar{r} = r/R, \quad \bar{\omega}_r = \omega_r\sqrt{mR^2/V_0},$$

$$\bar{K} = K\sqrt{mR^2V_0}.$$

Due to a scaling property (47), for the classical dynamics in the potential (44) [84, 86] the energetic dependence of the action \mathcal{I}_r (24), the angular momentum Λ , the frequency $\bar{\omega}_r$ (A.2) and the curvature \bar{K} (28) can be recovered in terms of the “scaled energy” \mathcal{E} ,

$$\mathcal{E} = \kappa \bar{E}^{1/\alpha+1/2}, \quad \kappa = \sqrt{\frac{mR^2V_0}{\hbar^2}}. \quad (\text{A.14})$$

In particular, one can express the classical quantities in (A.13) through their values at $\mathcal{E} = \kappa$ ($E = V_0$, or $\mathcal{E} = 1$) and put $\kappa = 1$ because there is no dependence on κ in all final results for the trace formula,

$$\mathcal{I}_i = \mathcal{I}_i(1)\mathcal{E}, \quad \Lambda = \Lambda(1)\mathcal{E}, \quad (\text{A.15})$$

$$\bar{\omega}_r^{-1} = \bar{\omega}_r^{-1}(1)\mathcal{E}^{(2-\alpha)/(2+\alpha)}, \quad \bar{K} = \bar{K}(1)/\mathcal{E},$$

where $\mathcal{I}_i(1)$, $\Lambda(1)$, $\bar{\omega}_r^{-1}(1)$ and $\bar{K}(1)$ are the corresponding quantities of (A.15) taken at “the scaled energy” $\mathcal{E} = 1$. Therefore, due to the scaling invariance (47) and (A.15) we need to calculate these classical dynamical quantities only at one value of the energy $\mathcal{E} = 1$ or $E = V_0$. In the following, we shall omit the argument $\mathcal{E} = 1$ everywhere for simplicity.

The energy surface \mathcal{I}_r for the potential (44) can be expressed explicitly in terms of the frequencies $\bar{\omega}_r$ and $\bar{\omega}_{\varphi}$ (see left identity in (26)) [69],

$$\mathcal{I}_r = \frac{2\alpha}{\alpha+2} \bar{\omega}_r^{-1} - \Lambda f(\Lambda). \quad (\text{A.16})$$

This relation is useful, in particular, for the derivation of the curvature K_D (102) for diameters as the limit of $\bar{K}(\Lambda)$ (28) at $\Lambda \rightarrow 0$. By differentiating the identity (A.16) term by term over Λ and using the definition for the ratio of frequencies $f(\Lambda)$ (26), for the curvature (28) one finally obtains (102), see [69] for details.

A4. JACOBIAN CALCULATIONS FOR CIRCULAR ORBITS

For the calculation of the Jacobian $\mathcal{J}_{MC}^{(p)}$ (75), one first transforms it to the invariant form. Using the general properties of the Jacobian transformations, for the Jacobian $\mathcal{J}_{MC}^{(p)}$ (75), one obtains

$$\mathcal{J}_{MC}^{(p)} = - \left(\frac{\partial^2 \Phi_{\text{CT}}}{\partial L^2} \right)_{MC} \frac{(\partial I_r / \partial p_r')_{MC}^2}{(\partial I_r / \partial L)_{MC}^2}, \quad (\text{A.17})$$

where

$$\left(\frac{\partial^2 \Phi_{\text{CT}}}{\partial L^2} \right)_{MC} = 2\pi M K_C, \quad (\text{A.18})$$

K_C is the curvature (28) for the circular orbits, see (84) [69]. According to the Legendre transformations (3), as applied for the radial action I_r ,

$$I_r = \int_{r'}^{r''} p_r dr = - \int_{p_r'}^{p_r''} r dp_r + p_r'' r'' - p_r' r', \quad (\text{A.19})$$

for the derivative $(\partial I_r / \partial p_r')_C$, one finds

$$\left(\frac{\partial I_r}{\partial p_r'} \right)_C = \left(r'' \frac{\partial p_r''}{\partial p_r'} \right)_C = r_C. \quad (\text{A.20})$$

Using also the expression (26) for $(\partial I_r / \partial L)_{MC}$, one obtains

$$\left(\frac{\partial I_r}{\partial L}\right)_{MC} = \left(\frac{\omega_\theta}{\omega_r}\right)_{MC} = \frac{\omega_C}{\Omega_C} = \frac{1}{\sqrt{\alpha+2}}, \quad (\text{A.21})$$

see (79) for the frequency of motion of a particle along the C PO ω_C and (78) for the radial frequency Ω_C , also for their ratio. Collecting (A.18), (A.20) and (A.21) in (A.17), for the Jacobian $\mathcal{J}_{MC}^{(p)}$ (75), one results in (83).

The arguments (89) of the error functions in the amplitude (86) in terms of the dimensionless curvature and angular momentum for the C orbits, see (A.13) and (A.15), are given by

$$\begin{aligned} \mathcal{Z}_{pMC}^+ &= \Lambda_C(1) \sqrt{-i\pi(\alpha+2)M\overline{K}_C(1)} \mathcal{E}, \\ \mathcal{Z}_{rMC}^- &= -\sqrt{\frac{F_{MC} \mathcal{E}}{4i\pi(\alpha+2)M\overline{K}_C(1)}}. \end{aligned} \quad (\text{A.22})$$

A5. THE JACOBIAN FOR DIAMETER TRACE FORMULAS

For the calculation of the Jacobian $J_\perp^{(p)}$ (101), we first transform it to the invariant Jacobian $\partial\Theta''/\partial L$ (see [59]) through the relations,

$$\delta y'' = r'' \delta \Theta'', \quad \delta L = r' \delta p_y', \quad (\text{A.23})$$

by using the standard Jacobian transformations as

$$J_\perp^{(p)} = \left(\frac{\delta y''}{\delta p_y'}\right)_{\text{PO}} = \left(\frac{\delta y''}{\delta \Theta''} \frac{\delta \Theta''}{\delta L} \frac{\delta L}{\delta p_y'}\right)_{MD}. \quad (\text{A.24})$$

The Jacobian $(\delta\Theta''/\delta L)_{MD}$ at the closed diameter orbit MD with M repetition number is invariant independent of the spacial coordinates, in particular of the radial coordinate $r' = r'' = r$. In [59] a more general case of the axial symmetrical potential was considered for the calculation of the Jacobian $(\delta\varphi''/\delta L_z)_{\text{PO}}$ at the PO with φ'' being the azimuthal angle and L_z the projection of the angular momentum of the particle onto a symmetry z axis. Using the axial symmetry, it was shown that this Jacobian is invariant independent of the spacial coordinates. The specific expression for $(\delta\varphi''/\delta L_z)_{\text{PO}}$ was obtained for the POs in the spheroidal cavity. In order to derive the specific expression for the Jacobian $(\delta\varphi''/\delta L_z)_{\text{PO}}$ in the middle of (A.24) for $J_\perp^{(p)}$, let us use the solution of the classical equations of motion (23) for $\theta(r)$ and the second identity in the middle of (26),

$$\delta\Theta'' = -2\pi\delta \frac{dI_r(E, L)}{dL} = -2\pi M K_D \delta L, \quad (\text{A.25})$$

where K_D is the curvature (102) for the diameter PO. Factor two takes into account that we have to calculate the Jacobian for the transformation of the variation of the perpendicular momentum $\delta p_y'$ to the variation of the final perpendicular momentum through the period T of the particle motion along the diameter which differs from

the period of the radial motion T_r by the factor 2, $T = 2T_r = 2\pi/\omega_r$:

$$T = \frac{2\pi n_\theta}{\omega_\theta} = \frac{2\pi n_\varphi}{\omega_\varphi} = \frac{2\pi n_r}{\omega_r}. \quad (\text{A.26})$$

For the diameters, one has $n_\theta = n_\varphi = 1$ and $n_r = 2$. Therefore, the Jacobian $(\delta\Theta''/\delta L)_{MD}$ takes the invariant form:

$$\left(\frac{\delta\Theta''}{\delta L}\right)_{MrMD} = -2\pi M K_D. \quad (\text{A.27})$$

From (A.23), (A.24) and (A.27), one finally arrives at (101) for the Jacobian $J_\perp^{(p)}$ (A.24).

A6. AMPLITUDE OF THE DIAMETER CONTRIBUTIONS

The amplitude of the diameter contribution into the PO sum in the trace formula (103) is proportional to the integral given by

$$I(M\zeta) = \int_0^1 du \mathcal{A}(u) e^{iM\zeta\Phi(u)}, \quad (\text{A.28})$$

where

$$\Phi(u) = u^2(1-u^\alpha), \quad (\text{A.29})$$

$$\mathcal{A}(u) = (1-u^\alpha)^{-1/2}. \quad (\text{A.30})$$

Let us evaluate this integral by using the ISPM, i.e. expanding the phase and pre-exponent amplitude factor near the stationary points u_i^* in powers of $u-u_n^*$ (n numbers the stationary points) as solution of the following equation:

$$\Phi'(u) \equiv 2u - (\alpha+2)u^{\alpha+1} = 0. \quad (\text{A.31})$$

For any $\alpha \geq 2$ under our consideration and a finite ζ , one has the two stationary points:

$$u_1 = \left(\frac{2}{\alpha+2}\right)^{1/\alpha}, \quad u_2 = 0. \quad (\text{A.32})$$

Expanding the exponent phase $\Phi(u)$ and the pre-exponent amplitude $\mathcal{A}(u)$ of the integrand (A.28) near the stationary points u_n [$n = 1, 2$, (A.32)] in power Taylor series, one finds

$$\Phi(u) = \Phi(u_n) + \frac{1}{2}\Phi''(u_n)(u-u_n)^2 + \dots, \quad (\text{A.33})$$

$$\mathcal{A}(u) = \mathcal{A}(u_n) + \dots. \quad (\text{A.34})$$

Note that in the limit $\alpha \rightarrow \infty$ one has the two close stationary points, that is for the catastrophe situation like caustic and turning points of Fedoriuk ([65–67, 69]) and the bifurcation points because they are at the boundary of the integration region $u = 1$. Therefore, following mainly [69], we should expand the phase and amplitude

up to higher order terms keeping the final integration limits.

According to the simplest ISPM, one can evaluate the integral (A.28) for large values of $|\zeta|$ through the error functions (63). Then, we arrive at (119). In these derivations, we used

$$\Phi_1'' = \Phi''(u_1) = -2\alpha, \quad \Phi_2'' = \Phi''(u_2) = 2. \quad (\text{A.35})$$

We transformed the integration variable u to z_1 for the evaluation of the contribution of the stationary point u_1 and to z_2 for u_2 by

$$\begin{aligned} z_1 &= \sqrt{-iM\zeta\Phi_1''/2}(u - u_1), \\ z_2 &= \sqrt{-iM\zeta\Phi_2''/2}u. \end{aligned} \quad (\text{A.36})$$

The integral $I(M\zeta)$ (A.28) can be expressed in terms of the error functions (63) by (119) with the arguments (120).

We show also several other helpful expressions derived as explained in the text through the dimensionless quantities:

$$r_{\max} = R(E/V_0)^{1/\alpha} = R\mathcal{E}^{2/(\alpha+2)}, \quad (\text{A.37})$$

$$\begin{aligned} \zeta &= -2\pi\overline{K_D}(1)\mathcal{E}, \\ (\kappa &= \sqrt{mR^2V_0/\hbar^2} = 1), \end{aligned} \quad (\text{A.38})$$

$$\begin{aligned} \frac{1}{\omega_r} &= \frac{1}{\overline{\omega}_r(1)} \sqrt{\frac{mR^2}{V_0}} \mathcal{E}^{(2-a)/(2+a)}, \\ \frac{1}{\overline{\omega}_r(1)} &= \frac{\Gamma(1+1/\alpha)}{\sqrt{2\pi}\Gamma(1/2+1/\alpha)}. \end{aligned} \quad (\text{A.39})$$

The trace formula (103) with the amplitude (116) can be written also in terms of the scaled quantities by using Appendix A6,

$$\mathcal{A}_{MD}^{(2)} = -\frac{mR^2\mathcal{E}^{4/(\alpha+2)}\sqrt{2}}{2\pi^2 i\hbar\overline{K_D}(1)M} [I(M\zeta) - I(0)], \quad (\text{A.40})$$

$$I(0) = \int_0^1 \frac{du}{\sqrt{1-u^\alpha}} = \frac{\sqrt{\pi}\Gamma(1+1/\alpha)}{\Gamma(1/2+1/\alpha)}. \quad (\text{A.41})$$

A7. STABILITY MATRIX FOR THE A ORBIT

For small energies e , the trace $\text{Tr } \mathcal{M}_A$ can be expressed through Mathieu functions by using a general method of solving Hill's equation for the Poincaré coordinate $x(t)$ perpendicular to the A orbit directed along the y axis. The perturbation $x(t)$ (in scaled variables (47)) near the A orbit is determined by Hill's equation (38) for the HH Hamiltonian (47),

$$\ddot{x}(t) + [1 + 2y_A(t)]x(t) = 0, \quad (\text{A.42})$$

where $y_A(t)$ is the periodic solution for the A orbit [81, 82, 85],

$$\begin{aligned} y_A &= y_1 + (y_2 - y_1)\text{sn}^2(z, k), \\ z &= a_k t + F(\varphi, k), \end{aligned} \quad (\text{A.43})$$

$\text{sn}(z, k)$ is the Jacobi elliptic function [124] with argument z ; its modulus k and the constant a_k are given by

$$k = \sqrt{\frac{y_2 - y_1}{y_3 - y_1}}, \quad a_k = \sqrt{\frac{y_3 - y_1}{6}}; \quad (\text{A.44})$$

y_1 and y_2 are the lower and upper turning points,

$$\begin{aligned} y_1 &= \frac{1}{2} - \cos\left(\frac{\pi}{3} - \frac{\phi}{3}\right), \\ y_2 &= \frac{1}{2} - \cos\left(\frac{\pi}{3} + \frac{\phi}{3}\right), \\ y_3 &= \frac{1}{2} + \cos\left(\frac{\phi}{3}\right), \quad \cos\phi = 1 - 2e. \end{aligned} \quad (\text{A.45})$$

$F(\varphi, k)$ is the incomplete elliptic integral of first kind as a function of

$$\begin{aligned} \varphi &= \arcsin\{[(y_0 - y_1)/(y_2 - y_1)]^{1/2}\}, \\ y_0 &= y_A(t=0) \end{aligned} \quad (\text{A.46})$$

is the initial value. Using the Fourier expansion of $\text{sn}^2(z, k)$, one has [125]

$$\begin{aligned} \text{sn}^2(z, k) &= \frac{K(k) - E(k)}{k^2 K(k)} - \frac{2\pi^2}{k^2 K^2(k)} \times \\ &\times \sum_{n=1}^{\infty} \frac{n s^n}{1 - s^{2n}} \cos\left(\frac{\pi n z}{K(k)}\right), \end{aligned} \quad (\text{A.47})$$

where $s = \exp[-\pi K(\sqrt{1-k^2})/K(k)]$ is Jacobi's Nome [124], $K(k)$ and $E(k)$ are the complete elliptic integrals of first and second kind, respectively.

For small energies e where Jacobi's Nome s is small, $s \rightarrow k^2/16 \approx \sqrt{e}/(12\sqrt{3})$ for $e \rightarrow 0$ [$k \rightarrow 0$, see (A.44)], the convergence of the Fourier series (A.47) is fast even for $e \lesssim 0.8$ ($s \lesssim 0.04$). For such energies, we may truncate the Fourier series approximately, keeping only the first ($n=1$) harmonic term. After substitution of (A.43) with the expansion (A.47), a simple transformation of the time variable and the parameters in (A.42) leads to the standard Mathieu equation:

$$\frac{d^2}{d\tau^2}x(\tau) + [a - 2b \cos(2\tau)]x(\tau) = 0, \quad (\text{A.48})$$

with

$$\begin{aligned} \tau &= \pi z/[2K(k)], \\ a &= \left(\frac{2K}{\pi a_k}\right)^2 \{1 + 2[y_1 + (y_2 - y_1)\frac{K-E}{k^2 K}]\}, \\ b &= 8s(y_2 - y_1)/[k^2 a_k(1 - s^2)]. \end{aligned} \quad (\text{A.49})$$

The solution of this second-order ordinary differential equation can be sought as a linear superposition of the fundamental set of the even $M_C(a, b, \tau)$ and odd $M_S(a, b, \tau)$ Mathieu functions with arbitrary constants C_1 and C_2 :

$$x(\tau) = C_1 M_C(a, b, \tau) + C_2 M_S(a, b, \tau). \quad (\text{A.50})$$

Applying to (A.50) the boundary conditions for calculations of the stability matrix elements \mathcal{M}_{xx} and $\mathcal{M}_{\dot{x}\dot{x}}$ as in [85], one obtains the constants C_1 and C_2 and the following diagonal matrix elements:

$$\mathcal{M}_{xx} = \frac{x(T)}{x(0)} \Big|_{\dot{x}(0) \rightarrow 0} = \frac{M'_{S,0} M_{C,T} - M'_{C,0} M_{S,T}}{M_{C,0} M'_{S,0} - M_{S,0} M'_{C,0}}, \quad (\text{A.51})$$

$$\mathcal{M}_{\dot{x}\dot{x}} = \frac{\dot{x}(T)}{\dot{x}(0)} \Big|_{x(0) \rightarrow 0} = \frac{M'_{S,T} M_{C,0} - M'_{C,T} M_{S,0}}{M_{C,0} M'_{S,0} - M_{S,0} M'_{C,0}},$$

where primes means the partial derivatives of the Mathieu functions $M_C(a, b, \tau)$ and $M_S(a, b, \tau)$ with respect to τ . The lower indices 0 and T show the values at the initial $t = 0$ and final $t = T$ times, and $T = T_A = 2K(k)/a_k$ is the period of motion of the particle along the A orbit. For the trace $\text{Tr } \mathcal{M}_A$, one finally finds

$$\text{Tr } \mathcal{M}_A = \mathcal{M}_{xx} + \mathcal{M}_{\dot{x}\dot{x}}, \quad (\text{A.52})$$

with the diagonal matrix elements given in (A.51).

For comparison, we recall the solution for the trace $\text{Tr } \mathcal{M}_A$ near the saddle $e \rightarrow 1$ obtained in [85, 93] in terms of the Legendre functions by using in (A.43) the approximation of the Jacobi elliptic function, $\text{sn}(z, k) \approx \tanh(z)$, i.e., by the zero-order term of its expansion near the saddle in powers of $1 - k^2$:

$$\begin{aligned} \text{sn}(z, k) &\approx \tanh z \times \\ &\times \left[1 + \frac{1}{4}(1 - k^2) \left(1 - \frac{z}{\sinh z \cosh z} \right) \right]. \end{aligned} \quad (\text{A.53})$$

As shown in [85, 93], the trace $\text{Tr } \mathcal{M}_A$ is in this approximation in good agreement with the numerical results [81] near the saddle $e \rightarrow 1$.

Generally speaking, for a more general solution, it is difficult to take into account exactly the next term of the expansion (A.53) to get a simple analytical result similar to that presented explicitly in [85]. However, we may use the approximate constant r for the square brackets in (A.53), which effectively takes into account the correction to $\tanh z$,

$$r \approx 1 + r_{\text{corr}}(1 - k^2), \quad r_{\text{corr}} = 1/4. \quad (\text{A.54})$$

Within this approximation, one has again the result in terms of the Legendre functions P_ν^μ and Q_ν^μ with complex indices ν and μ depending on the energy e

$$\mu = i\sqrt{A+B}, \quad \nu = (-1 + i\sqrt{4A-1})/2, \quad (\text{A.55})$$

where B is the same as in [85] but A contains the additional constant factor r :

$$A = 12rk^2, \quad B = (1 + 2y_1)/a_k^2, \quad (\text{A.56})$$

corresponding at $r=1$ (or $r_{\text{corr}} = 0$ in our notations) to the results in [85].

The comparison of numerical calculations [81, 88] with our analytical results for the trace of the stability matrix $\text{Tr } \mathcal{M}_A$ in the case of the A orbit was presented in [71]. The solution for $\text{Tr } \mathcal{M}_A$ in terms of the Mathieu functions is in good agreement with the exact numerical results even at energies $e \lesssim 0.8$. We show in [71] also another approximation in terms of Legendre functions with the indices (A.55), improved at finite and small energies e through the constant A (A.56) with r given in (A.54) as compared to the result ($r = 1$) obtained earlier near the saddle [i.e., using only the leading term in the expansion (A.53) for $e-1 \ll 1$] [85]. Through a modification of only one constant r (A.54), one has a remarkable agreement between this improved Legendre approximation and the numerical results everywhere from the saddle point e to the harmonic oscillator limit $\text{Tr } \mathcal{M}_A \rightarrow 2$ for $e \rightarrow 0$.

This approximation can be slightly improved changing the constant r_{corr} in (A.54) from $r_{\text{corr}} = 1/4$ ($z \rightarrow \infty$) to about $2/9$ of finite values of z . For small energies e ($k \rightarrow 0$), one can, again, formally use (A.53): the correction to $\tanh z$ can be neglected for small times ($z \ll 1$) because it gives the dominating contribution to $\text{Tr } \mathcal{M}_A$ [equation (A.42) with (A.43) becomes approximately the same at small z], and $\text{Tr } \mathcal{M}_A \rightarrow 2$ in all analytical approximations, in agreement with the numerical results. In the limit $e \rightarrow 0$ the Legendre function approximation converges, indeed, to the analytical Mathieu function solution. Note also that this agreement with the numerical results is not sensitive to a variation of the constant r_{corr} around the analytical value (A.54). The particle moving near the A orbit spends much more time near the saddle where the function of $z \propto t$ in the circle brackets (A.53) is almost constant with respect to the remaining part of the trajectory. However, at small energies $e \rightarrow 0$, one finds a smaller time region ($z \ll 1$) where the correction in (A.53) becomes negligible for $\text{Tr } \mathcal{M}_A$, such that all approximations have the same correct harmonic-oscillator limit 2. Thus, a rather complicated function of time in the correction to the leading (hyperbolic tangent) term of the expansion of the Jacobi function (A.53) can be reduced to a form involving the same Legendre functions as in [85], but with modified indices by the constant r (A.54) through (A.56).

-
- [1] M. Gutzwiller, J. Math. Phys. **12**, 343 (1971); *Chaos in Classical and Quantum Mechanics* (Springer-Verlag, N.Y., 1990).
 - [2] R. B. Balian and C. Bloch, Ann. Phys. (N.Y.) **69**, 76 (1972).
 - [3] V. M. Strutinsky, Nucleonika **20**, 679 (1975); V. M. Strutinsky and A. G. Magner, Fiz. Elem. Chast. At. Nucl. **7**, 356 (1976) [Sov. J. Part. Nucl. **7**, 138 (1976)].
 - [4] M. V. Berry and M. Tabor, Proc. R. Soc. Lond. A **349**, 101 (1976); **356**, 375 (1977).
 - [5] V. M. Strutinsky, A. G. Magner, S. R. Ofengenden, and T. Døssing, Z. Phys. A **283**, 269 (1977).
 - [6] S. C. Creagh, J. M. Robbins, and R. G. Littlejohn, Phys. Rev. A **42**, 1907 (1990); S. C. Creagh, R. G. Littlejohn, Phys. Rev. A **44**, 836 (1991); J. Phys. A **25**, 1643 (1992).

- [7] M. Brack and R. K. Bhaduri, *Semiclassical Physics* (revised edition: Westview Press, Boulder, USA, 2003).
- [8] A. G. Magner, I. S. Yatsyshyn, K. Arita, and M. Brack, *Yad. Fiz.* **74**, 1 (2011) [*Phys. Atom. Nucl.* **74**, 1445 (2011)].
- [9] V. M. Strutinsky, *Nucl. Phys. A*, **95**, 420 (1967); **122**, 1 (1968).
- [10] M. Brack, J. Damgaard, A. S. Jensen *et al.*, *Rev. Mod. Phys.* **44**, 320 (1972).
- [11] W. D. Myers and W. J. Swiatecki, *Ann. Phys. (N.Y.)* **55**, 395 (1969); **84**, 186 (1974).
- [12] M. Brack, C. Guet, and H.-B. Hakransson, *Phys. Rept.* **123**, 275 (1985).
- [13] A. B. Migdal, *The Finite Fermi-System Theory and Properties of Atomic Nuclei* (Interscience, New York, 1967; Nauka, Moscow, 1983).
- [14] V. A. Khodel, E. E. Saperstein, *Phys. Rep.* **5**, 183 (1982).
- [15] L. D. Landau, *Zh. Eksp. Teor. Fiz.* **30**, 1058 (1956) [*Sov. J. Exp. Theor. Phys.* **3**, 920 (1957)]; **35**, 97 (1958); [*Sov. J. Exp. Theor. Phys.* **8**, 70 (1959)];
- [16] A. A. Abrikosov and I. M. Khalatnikov, *Rept. Prog. Phys.* **22** 329 (1959).
- [17] A. Bohr and B. Mottelson, *Nuclear structure*, Vol. 2 (Benjamin, New York, 1975).
- [18] P. Ring and P. Schuck. *The Nuclear Many-Body Problem*, (Springer-Verlag, New York, Heisenberg, Berlin, 1980).
- [19] H. Hofmann, *The Physics of warm nuclei with analogies to mesoscopic systems*, (Oxford, University Press, 2008).
- [20] V. V. Pashkevich and S. Frauendorf, *Yad. Fiz.* **20**, 1122 (1974) [*Sov. J. Nucl. Phys.* **20**, 588 (1974)].
- [21] I. N. Mikhailov, K. Neergard, V. V. Pashkevich, and S. Frauendorf, *Fiz. Elem. Chast. At. Nucl.* **8**, 1338 (1977) [*Sov. J. Part. Nucl.* **8**, 550 (1977)].
- [22] S. Frauendorf, arXiv: 1209.5816 [nucl-th], 2012; *Pairing at High Spins*: In book R. A. Broglia and V. Zelevinsky, *Fifty Years of Nuclear BCS: Pairing in Finite Systems*, (World Scientific, Singapore, 2013).
- [23] A. G. Magner, V. M. Kolomietz, V. M. Strutinsky, *Yad. Fiz.* **28**, 1487 (1978) [*Sov. J. Nucl. Phys.* **28**, 764 (1978)].
- [24] V. M. Kolomietz, A. G. Magner, and V. M. Strutinsky, *Yad. Fiz.* **29**, 1478 (1979) [*Sov. J. Nucl. Phys.* **29**, 758 (1979)].
- [25] A. G. Magner, V. M. Kolomietz, and V. M. Strutinsky, *Izvestiya Akad. Nauk SSSR, Ser. Fiz.* **43**, 2408 (1979) [*Bull. of the Academy of Science of SSSR, Ser. Fiz.* **43**, 142 (1979)].
- [26] K. Richter, D. Ulmo, and R. A. Jalabert, *Phys. Rept.* **276**, 1 (1996).
- [27] S. Frauendorf, V. M. Kolomietz, A. G. Magner, and A. I. Sanzhur, *Phys. Rev. B* **58**, 5622 (1998).
- [28] M. A. Deleplanque, S. Frauendorf, V. V. Pashkevich, S. Y. Chu, and A. Unzhakova, *Phys. Rev. C* **69**, 044309 (2004).
- [29] A. G. Magner, A. S. Sitdikov, A. A. Khamzin, J. Bartel, and A. M. Gzhebinsky, *Nucl. Phys. and At. Energy* **10**, 239 (2009); *Int. J. Mod. Phys. E* **19**, 735 (2010); *Phys. Atom. Nucl.* **73**, 1398 (2010).
- [30] A. G. Magner, A. S. Sitdikov, A. A. Khamzin, and J. Bartel, *Phys. Rev. C* **81**, 064302 (2010).
- [31] A. G. Magner, D. V. Gorpichenko, and J. Bartel, *Phys. Atom. Nucl.* **77**, 1229 (2014) [*Yad. Fiz.* **77**, 1 (2014)].
- [32] D. V. Gorpichenko, A. G. Magner, J. Bartel, and J. P. Blocki, *Phys. Scr.* **90**, 114008 (2015).
- [33] D. V. Gorpichenko, A. G. Magner, J. Bartel, and J. P. Blocki, *Phys. Rev. C* **93**, 024304 (2016).
- [34] S. T. Belyaev, V. G. Zelevinsky, *Niels Bohr and Physics of Atomic Nuclei*, *Usp. Phys. Sci.* **147**, 210 (1985) [*Sov. Phys. -Usp.* **147**, 854 (1985)].
- [35] V. G. Solovjov, *Fiz. Elem. Chast. At. Nucl.* **9**, 580 (1978).
- [36] V. G. Solovjov, *Fiz. Elem. Chast. At. Nucl.* **11**, 301 (1980).
- [37] V. G. Solovjov, *Theory of Atomic Nucleus. Nuclear Models (Teoriya atomnogo yadra. Yadernyye modeli*, Energoizdat, Moscow, 1981).
- [38] V. G. Solovjov and A. I. Vdovin, *Fiz. Elem. Chast. At. Nucl.* **14**, 237 (1983).
- [39] V. G. Solovjov and V. V. Voronov, *Fiz. Elem. Chast. At. Nucl.* **14**, 1380 (1983).
- [40] V. G. Solovjov, A. I. Vdovin, V. V. Voronov, Ch. Stojanov, *Fiz. Elem. Chast. At. Nucl.* **16**, 245 (1985).
- [41] V. G. Solovjov, *Theory of Atomic Nuclei: Quasiparticles and Phonons* (Institute of Physics, Bristol and Philadelphia, 1992).
- [42] V. G. Solovjov, *Structure of even deformed nuclei (Struktura chiotnykh deformirovannykh yader*, Nauka, Moscow, 1974).
- [43] V. G. Solovjov, *Theory of Complex Nuclei* (Pergamon Press, Oxford, N.Y., Sydney, Paris, 1976).
- [44] V. G. Solovjov, *Nucl. Phys. A* **9**, 655 (1958).
- [45] S. T. Belyaev, *Zhur. Eksptl' i Teoret. Fiz.*, **40**, 672 (1961).
- [46] V. G. Solovjov, *Effect of Superconducting Pairing Correlations on Nuclear Properties*; in: *Selected Topics in Nuclear Theory* (IAEA, Vienna, 1963).
- [47] S. T. Belyaev, V. G. Zelevinsky, *Yad. Fiz.* **11**, 416 (1970) [*Sov. J. Nucl. Phys.* **11**, 416 (1970)]. **16**, 1195 (1972) [*Sov. J. Nucl. Phys.* **16**, 416 (1972)]. **17**, 525 (1973) [*Sov. J. Nucl. Phys.* **17**, 269 (1973)].
- [48] D. Vautherin and D. M. Brink, *Phys. Rev. C* **5**, 626 (1972).
- [49] M. Brack and P. Quentin, *Nucl. Phys. A* **361**, 35 (1981).
- [50] V. I. Abrosimov, D. M. Brink, A. Delafiore, and F. Matera, *Nucl. Phys. A* **864**, 38 (2011); and the works cited therein.
- [51] H. Hofmann, F. A. Ivanyuk, and J. Yamaji, *Nucl. Phys. A* **598** 187 (1996).
- [52] F. A. Ivanyuk, H. Hofmann, V. V. Pashkevich, and J. Yamaji, *Phys. Rev. C* **55**, 1730 (1997).
- [53] A. G. Magner, S. Vydrug-Vlasenko, and H. Hofmann, *Nucl. Phys. A* **524**, 31 (1991); *Izv. Akad. Nauk SSSR, Ser. Fiz.* **54**, 148 (1990).
- [54] A. M. Gzhebinsky, A. G. Magner, and S. N. Fedotkin, *Phys. Rev. C* **76**, 064315 (2007).
- [55] A. G. Magner, A. M. Gzhebinsky, S. N. Fedotkin, *Phys. Atom. Nucl.* **70**, 647 [*Yad. Fiz.* **70**, 677 (2007)]; 1859 (2007).
- [56] J. P. Blocki, A. G. Magner, and I. S. Yatsyshyn, *Int. Journ. Mod. Phys. E* **21**, 1250034 (2012).
- [57] J. P. Blocki and A. G. Magner, *Phys. Scr. T* **154**, 014006 (2013).
- [58] G. Lazari, H. Nishioka, E. Vigezzi, R. A. Broglia, *Phys. Rev. B* **53**, 1064 (1996).
- [59] A. G. Magner, S. N. Fedotkin, F. A. Ivanyuk *et al.*, *Ann. Physik* **509**, 555 (1997).
- [60] M. Brack, S. M. Reimann and M. Sieber, *Phys. Rev. Lett.* **79**, 1817 (1997).
- [61] A. G. Magner, S. N. Fedotkin, K. Arita, K. Matsuyanagi, and M. Brack, *Phys. Rev. E* **63**, 065201(R)

- (2001).
- [62] A. G. Magner, K. Arita, S. N. Fedotkin, and K. Matsuyanagi, *Prog. Theor. Phys.* **108**, 853 (2002).
 - [63] A. G. Magner, *Nucl. Phys. At. Energy* **11**, 227 (2010).
 - [64] A. G. Magner, *Yad. Fiz.* **28**, 1477 (1978) [*Sov. J. Nucl. Phys.* **28**, 764 (1978)].
 - [65] M. V. Fedoryuk, *Sov. J. Com. Math. Math. Phys.* **2**, 145 (1962); **4**, 671 (1964).
 - [66] M. P. Maslov, *Theor. Math. Phys.* **2**, 30 (1970).
 - [67] M. V. Fedoriuk, *The saddle-point method (Metod perevala)*, Nauka, Moscow, 1977).
 - [68] C. Chester, B. Friedmann, F. Ursell, *Proc. Cambridge Philos. Soc.* **53**, 599 (1957).
 - [69] A. G. Magner, K. Arita, and S. N. Fedotkin, *Prog. Theor. Phys.* **115**, 523 (2006).
 - [70] A. G. Magner, S. N. Fedotkin, K. Arita, T. Misu, K. Matsuyanagi, T. Schachner, and M. Brack, *Prog. Theor. Phys.* **102**, 551 (1999).
 - [71] M. V. Koliesnik, Ya. D. Krivenko-Emetov, A. G. Magner, K. Arita, and M. Brack, *Phys. Scr.* **90**, 114011 (2015).
 - [72] A. M. Ozorio de Almeida: *Hamiltonian Systems: Chaos and Quantization* (Cambridge University Press, Cambridge, 1988).
 - [73] D. Ullmo, M. Grinberg, and S. Tomsovic, *Phys. Rev. E* **54**, 136 (1996).
 - [74] S. C. Creagh, *Ann. Phys. (N.Y.)* **248**, 60 (1997).
 - [75] M. Sieber, *J. Phys. A* **30**, 4563 (1997).
 - [76] M. Brack, J. Blaschke, S. C. Creagh *et al.*, *Z. Phys. D* **40**, 276 (1997).
 - [77] H. Schomerus and M. Sieber, *J. Phys. A* **30** (1997), 4537; M. Sieber and H. Schomerus, *J. Phys. A* **31**, 165 (1998).
 - [78] H. Schomerus, *J. Phys. A: Math. Gen.* **31**, 4167 (1998).
 - [79] M. Brack, P. Meier, and K. Tanaka, *J. Phys. A* **32**, 331 (1999).
 - [80] M. Brack, *Foundations of Physics* **31**, 209 (2001) (see also arXiv:nlin.CD/0006034).
 - [81] M. Brack, M. Mehta, and K. Tanaka, *J. Phys. A: Math. Gen.* **34**, 8199 (2001).
 - [82] J. Kaidel, M. Brack, *Phys. Rev. E* **70**, 016206 (2004).
 - [83] K. Arita and M. Brack, *J. Phys. A* **41**, 385207 (2008).
 - [84] K. Arita, *Phys. Rev. C* **86**, 034317 (2012).
 - [85] S. N. Fedotkin, A. G. Magner, and M. Brack, *Phys. Rev. E* **77**, 066219 (2008).
 - [86] K. Arita, *Int. J. Mod. Phys. E* **13** 191 (2004).
 - [87] A. G. Magner, A. A. Vlasenko, K. Arita, *Phys. Rev. E* **87**, 062916 (2013).
 - [88] M. Brack and K. Tanaka, *Phys. Rev. E* **77**, 046205 (2008).
 - [89] M. Brack, R. K. Bhaduri, J. Law and M. V. N. Murthy, *Phys. Rev. Lett.* **70** 568 (1993).
 - [90] J. P. Blocki, A. G. Magner, and I. S. Yatsyshyn, *Nucl. Phys. At. Energy* **11**, 239 (2010).
 - [91] J. P. Blocki, A. G. Magner, and I. S. Yatsyshyn, *Int. J. Mod. Phys. E* **20**, 292 (2011).
 - [92] J. P. Blocki and A. G. Magner, *Phys. Rev. C* **85**, 064311 (2012).
 - [93] M. Brack, J. Kaidel, P. Winkler, and S. N. Fedotkin 2006, *Few-Body Syst.* **38**, 147 (2006).
 - [94] C. Gustafsson, P. Möller, and S. G. Nilsson, *Phys. Lett.* **34 B**, 349 (1971).
 - [95] S. Cohen and W. J. Swiatecki, *Ann. Phys. (N. Y.)* **22**, 406 (1963).
 - [96] P. T. Richens, *Journ. Phys. A: Math. and Gen.* **15**, 2101 (1982).
 - [97] H. Frisk, *Nucl. Phys. A* **511**, 309 (1990).
 - [98] I. Hamamoto and B. R. Mottelson, *Phys. Rev. C* **79**, 034317 (2009).
 - [99] N. Tajima and N. Suzuki, *Phys. Rev. C* **64**, 037301 (2001); N. Tajima, Y. R. Shimizu, and N. Suzuki, *Prog. Theor. Phys. Suppl.* **146**, 628 (2002).
 - [100] S. Takahara, N. Onishi, Y. R. Shimizu, and N. Tajima, *Phys. Lett. B* **702**, 429 (2011); S. Takahara, N. Tajima, and Y. R. Shimizu, *Phys. Rev. C* **86**, 064323 (2012).
 - [101] K. Arita, to appear in *Phys. Scr.* (2016).
 - [102] P. A. Butler and W. Nazarewicz, *Rev. Mod. Phys.* **68**, 349 (1996).
 - [103] J. Blocki *et al.*, *Ann. Phys. (N.Y.)* **113**, 330 (1978).
 - [104] J. Blocki, J. Skalski, and W. J. Swiatecki, *Nucl. Phys. A* **594**, 137 (1995); J. Blocki, J.-J. Shi, W. J. Swiatecki, *Nucl. Phys. A* **554**, 387 (1993); C. Jarzynski and W. J. Swiatecki, *Nucl. Phys. A* **552**, 1 (1993); P. Magierski, J. Skalski, and J. Blocki, *Phys. Rev. C* **56**, 1011 (1997).
 - [105] J. P. Blocki, A. G. Magner, and I. S. Yatsyshyn, *Nucl. Phys. and At. Energy* **11**, 239 (2010); *Int. J. Mod. Phys. E* **20**, 292 (2011); **21**, 1250034 (2012).
 - [106] I. Hamamoto, B. R. Mottelson, H. Xie, and X. Z. Zhang, *Z. Phys. D* **21**, 163 (1991).
 - [107] S. M. Reimann, M. Koskinen, H. Häkkinen, P. E. Lindelof, and M. Manninen, *Phys. Rev. B* **56**, 12147 (1997).
 - [108] S. Takami, K. Yabana, and M. Matsuo, *Phys. Lett. B* **431**, 242 (1998).
 - [109] J. Dudek, A. Goźdź, N. Schunck, and M. Miśkiewicz, *Phys. Rev. Lett.* **88**, 252502 (2002).
 - [110] K. Arita and Y. Mukumoto, *Phys. Rev. C* **89**, 054308 (2014).
 - [111] M. Brack, M. Ögren, Y. Yu, and S. M. Reimann, *J. Phys. A* **38**, 9941 (2005).
 - [112] H. Frisk and T. Guhr, *Ann. Phys. (N. Y.)* **221**, 229 (1993).
 - [113] Ch. Amann and M. Brack, *J. Phys. A: Math. Gen.* **35** 6009 (2002).
 - [114] M. Brack, Ch. Amann, M. Pletyukhov, and O. Zaitsev, *Int. J. Mod. Phys. E* **13** 19 2(004).
 - [115] K. Bencheikh, P. Quentin, and J. Bartel, *Nucl. Phys. A* **571**, 518 (1994).
 - [116] V. M. Strutinsky and A. S. Tyapin, *Zh. Eksp. Teor. Fiz.* **45**, 960 (1963) [*Sov. J. Exp. Theor. Phys.* **18**, 664 (1964)].
 - [117] V. M. Strutinsky, A. G. Magner, and M. Brack, *Z. Phys. A* **319** 205 (1984).
 - [118] V. M. Strutinsky, A. G. Magner, and V. Yu. Denisov, *Z. Phys. A* **322**, 149 (1985); *Yad. Fiz.* **42**, 1093 (1985) [*Sov. J. Nucl. Phys.* **42**, 690 (1985)].
 - [119] A. G. Magner, A. I. Sanzhur, and A. M. Gzhebinsky, *Int. J. Mod. Phys. E* **18**, 885 (2009).
 - [120] J. P. Blocki, A. G. Magner, P. Ring, and A. A. Vlasenko, *Phys. Rev. C* **87**, 044304 (2013).
 - [121] J. P. Blocki, A. G. Magner, and P. Ring, *Phys. Scr.* **89**, 054019 (2014).
 - [122] J. P. Blocki, A. G. Magner, and P. Ring, *Phys. Scr.* **90**, 114009 (2015).
 - [123] J. P. Blocki, A. G. Magner, and P. Ring, *Phys. Rev. C* **92**, 064311 (2015).
 - [124] P. F. Byrd and M. D. Friedman, *Handbook of Elliptic Integrals for Engineers and Scientists* (2nd ed, Springer-Verlag New York, Heidelberg, Berlin, 1971).
 - [125] S. C. Milne, *Infinite Families of Exact Sums of Squares Formulas Jacobi Elliptic Functions, Continued Fractions, and Schur Functions* (Kluwer Academic Publishers); the Ramanujan Journal **6** 7 (2002).

CAPTIONS TO FIGURES:

Fig. 1. Poincaré surfaces of sections (PSS) of the scaled Hénon-Heiles Hamiltonian h (47); left column: (a), (b) and (c) plots show the PSS at $u = 0$ for the energies $e = 0.5, 0.75$ and 1.0 , respectively; right column: (d), (e) and (f) graphics are given for $v = 0$ at the same energies.

Fig. 2. The scaled Hénon-Heiles potential of the Hamiltonian (47). *Left:* Equipotential contour lines are given in scaled energies e in the plane (u, v) . The dashed lines are the symmetry axes. The three shortest orbits A, B, and C (evaluated at the energy $e = 1$) are shown by the heavy solid lines. *Right:* Cut along $u = 0$ shows a barrier. (After [7, 89].)

Fig. 3. Quantum-mechanical (QM, solid), semiclassical (ISPM, dashed), and Gutzwiller (GUTZ, dots) shell-corrections level density versus energy E (in units of $\hbar\omega$). Only the primitive POs A, B and C are included in the semiclassical calculations, the Gaussian averaging width is $\gamma = 0.25\hbar\omega$.

Fig. 4. Quantum and semiclassical shell-correction energy δU (18) (in units of the Fermi energy E_F) versus particle number parameter $N^{1/2}$, with $N = 2 \int_0^{E_F} dE g(E)$. The same primitive POs are included as explained in the text.

Fig. 5. *Left:* Schematic double-humped fission barrier of a typical actinide nucleus. Note the lowering of the outer barrier due to left-right asymmetric shapes. *Right:* Maximum probability amplitudes (schematic) of the two leading s.p. states responsible for the asymmetry effect (after [94]).

Fig. 6. Axially symmetric nuclear shapes in the (c, h, α) parametrization of [10]. Dashed lines for $\alpha \neq 0$; the sequence with $h = \alpha = 0$ corresponds to the shapes obtained in the LDM [95].

Fig. 7. Plot of quantum-mechanical shell-correction energy δU versus cube-root of particle number, $N^{1/3}$, and elongation c (along $h = \alpha = 0$) in the cavity model. The contours lines are for constant values of δU (*white:* positive values, *gray to black:* negative values). The heavy lines indicate the loci of constant actions of the leading POs. *Dashed-dotted lines:* meridional triangular orbits (3,1,1)s; *narrow lines:* diameter orbits in equatorial planes (2,1)EQ (solid) and in parallel perpendicular planes (2,1)AQ (dashed); *broad lines:* triangular orbits in equatorial planes (3,1)EQ (solid) and in parallel perpendicular planes (3,1)AQ (dashed). The horizontal dotted line at $N \simeq 180$ corresponds to the situation with the isomer minimum at the correct deformation [10] $c \simeq 1.42$ of the real nucleus ^{240}Pu .

Fig. 8. Fourier spectra of the fission cavity model with $h = \alpha = 0$ for five values of c : amplitude of Fourier transform of the quantum spectrum versus length L (in units of R_0) of the classical POs. *Short arrows:* POs lying in planes orthogonal to symmetry axis; *long arrows:* POs lying in meridional planes

containing the symmetry axis (labels as in Fig. 7; see text for more details).

Fig. 9. Perspective view of the semiclassical outer fission barrier versus elongation c and left-right asymmetry α for $h = 0$. To the left, the shapes corresponding to the points A, B and C in the deformation energy surface are displayed; the vertical solid (dashed) lines indicate the planes containing the stable (unstable) POs.

Fig. 10. Contour plots of the shell-correction energy δU versus c and α . *Upper panels:* for $h = 0$, *lower panels:* for $h = -0.075$. *Left panels:* results of quantum-mechanical SCM calculations with realistic nuclear shell model potentials [10] (shown is the shell correction of the neutrons); *right panels:* semiclassical POT results with the fission cavity model described above.

Fig. 11. The scaled periods τ_{PO} (horizontal axis) of some short periodic orbits PO plotted as functions of the power parameter α (vertical axis). Thin solid curves are circle orbits MC , dashed green curves are diameter orbits $M(2,1)$, and thick solid curves are polygon-like orbits $M(n_r, n_\varphi)$ ($n_r > 2n_\varphi$) which bifurcate from the circle orbits MC at the bifurcation points indicated by open circles.

Fig. 12. Moduli of the Fourier transform $|F(\tau)|$ of the quantum scaled-energy level density (138) plotted for several values of α .

Fig. 13. Comparison of the quantum-mechanical (QM, solid) and semiclassical [ISPM (dashed) and SSPM (dots)] shell-correction scaled-energy level density $\delta\mathcal{G}_\gamma(\mathcal{E})$, see (128) and (127), divided by \mathcal{E} [see (129)], as function of the scaled-energy \mathcal{E} for $\alpha = 6.0$ and averaging parameter $\gamma = 0.6$ [upper panel (a)]; contributions of the $\mathcal{K} = 3$ (PISP, thick solid), circular (CISP, dots), and diameter (DISP, approximately DSSP, dashed) POs [lower panel (b)].

Fig. 14. Same as in Fig. 13 at $\alpha = 6.0$ but for the averaging parameter $\gamma = 0.2$.

Fig. 15. Same as in Fig. 13 at $\alpha = 6.0$ but for the averaging parameter $\gamma = 0.03$.

Fig. 16. Same as in Fig. 13 at $\alpha = 7.0$ but for the averaging parameter $\gamma = 0.6$ (without CISP POs).

Fig. 17. Same as in Fig. 13 at $\alpha = 7.0$ but for the averaging parameter $\gamma = 0.2$ (without CISP POs).

Fig. 18. Same as in Fig. 13 at $\alpha = 7.0$ but for the averaging parameter $\gamma = 0.1$ (without CISP POs).

Fig. 19. Shell-correction energy $\delta\mathcal{U}$ (scaled and divided by \mathcal{E}_F) as function of the particle number parameter $N^{1/3}$ at $\alpha = 6.0$ [upper panel (a)]; contributions of the $\mathcal{K} = 3$ (PISP, thick solid), circular (CISP, dots), and diameter (DISP, approximately DSSP, dashed) POs [lower panel (b)].

Fig. 20. Same as in Fig. 19 but at $\alpha = 7.0$ [upper panel (a)]; [lower panel (b)]: same as Fig. 19 but without CISP POs.

Fig. 21. The equi-potential surfaces of the spheroidal ($\delta = 0.5$, solid curve) and quadrupole ($\beta_2 = 0.4$, broken curve) deformations in the meridian plane.

Fig. 22. Single-particle level diagrams of the power-law potential model with $\alpha = 5.0$. Scaled energy eigenvalues ε_i in the PLP potential (141) are plotted as functions of the deformation parameters: (a) for the spheroidal deformation δ (147) and (b) for the quadrupole deformation β_2 (148). Solid and broken lines represent positive and negative parity levels, respectively.

Fig. 23. Poincaré surfaces of section (x, p_x) of the meridian-plane trajectories in the power-law potential (141) with $\alpha = 5.0$ and deformations shown in Fig. 21.

Fig. 24. Some short meridian-plane orbits in the power-law potential (141) with $\alpha = 5.0$ and deformations shown in Fig. 21.

Fig. 25. PO scaled periods as functions of the deformation parameter δ for the power parameter $\alpha = 3.0$; *MX* (long-dashed lines) are those of the equatorial diameter POs, *MZ* (short-dashed ones) are symmetry-axis diameter PO. Dots indicate the bifurcation points of the meridian bridge orbits, and their scaled periods are shown by solid and dotted lines for *MC* and for the other meridian bridges *MB*, respectively. *MEC* (dash-dotted lines) are equatorial circular orbit, whose bifurcations are omitted to avoid complication.

Fig. 26. Illustration of the growth of the bridge orbit C with increasing power parameter α . Scaled periods of the periodic orbits C (meridian oval), X (equatorial diameter) and Z (symmetry-axis diameter) are plotted as functions of deformation parameter δ for $\alpha = 2.5, 3.0$ and 5.0 . Bifurcation points are indicated by the dots.

Fig. 27. Color map of the Fourier amplitude $|F(\tau; \delta)|$ as function of δ and τ . Lines represent the scaled periods τ_{PO} of the classical periodic orbits as functions of the deformation parameter δ . Dots indicate the bifurcation points.

Fig. 28. Contour map of the shell-correction energies in the $(\delta, N^{1/3})$ plane. The negative and positive

shell-correction energies are shown by the red (solid) and blue (broken) contour lines, respectively. The thick lines are the constant-action lines of the bridge orbit C.

Fig. 29. Shapes of the equi-potential surfaces for three values of the tetrahedral deformation parameter $\beta_{td} = 0.1, 0.5$ and 0.9 . The tetrahedron corresponding to $\beta_{td} = 1$ is also drawn with dotted lines in all panels.

Fig. 30. Single-particle level diagram of power-law potential model for the tetrahedral deformation (a) $\alpha = 4.0$ and (b) 6.0 . Scaled energy levels \mathcal{E}_i are plotted as functions of the tetrahedral deformation parameter β_{td} . Dotted, dashed and solid lines represent the levels belonging to the A, E and F irreps of the T_d group.

Fig. 31. Some short periodic orbits in the tetrahedral-like deformed power-law potential model with $\alpha = 6.0$. The top and middle 6 panels are for $\beta_{td} = 0.3$, and the bottom 3 panels are for the written values of β_{td} . Thick solid lines represent the orbits and the thick dashed lines represent their projections onto (x, y) , (y, z) and (z, x) planes. Thin dotted lines represent the tetrahedron which has the same symmetry of the equi-potential surface.

Fig. 32. The scaled periods τ_{PO} of the classical periodic orbits for the power parameter $\alpha = 6.0$ as functions of the tetrahedral-deformation parameter β_{td} . Dots indicate the bifurcation points. The bottom panel is the enlargement of the top panel in the region indicated by the dotted rectangle.

Fig. 33. Color map of the Fourier amplitude $|F(\tau; \beta_{td})|$ of the quantum scaled-energy level density in the (β_{td}, τ) plane. Solid lines represent the scaled periods τ_{PO} of the classical periodic orbits as functions of β_{td} . Dots indicate their bifurcation points.

Fig. 34. Shell-correction energies δU plotted in units of V_0 as functions of the cubic root of the particle number $N^{1/3}$. Solid lines represent quantum mechanical results. Dashed lines in the two bottom panels represent the semiclassical results based on the Gutzwiller trace formula.

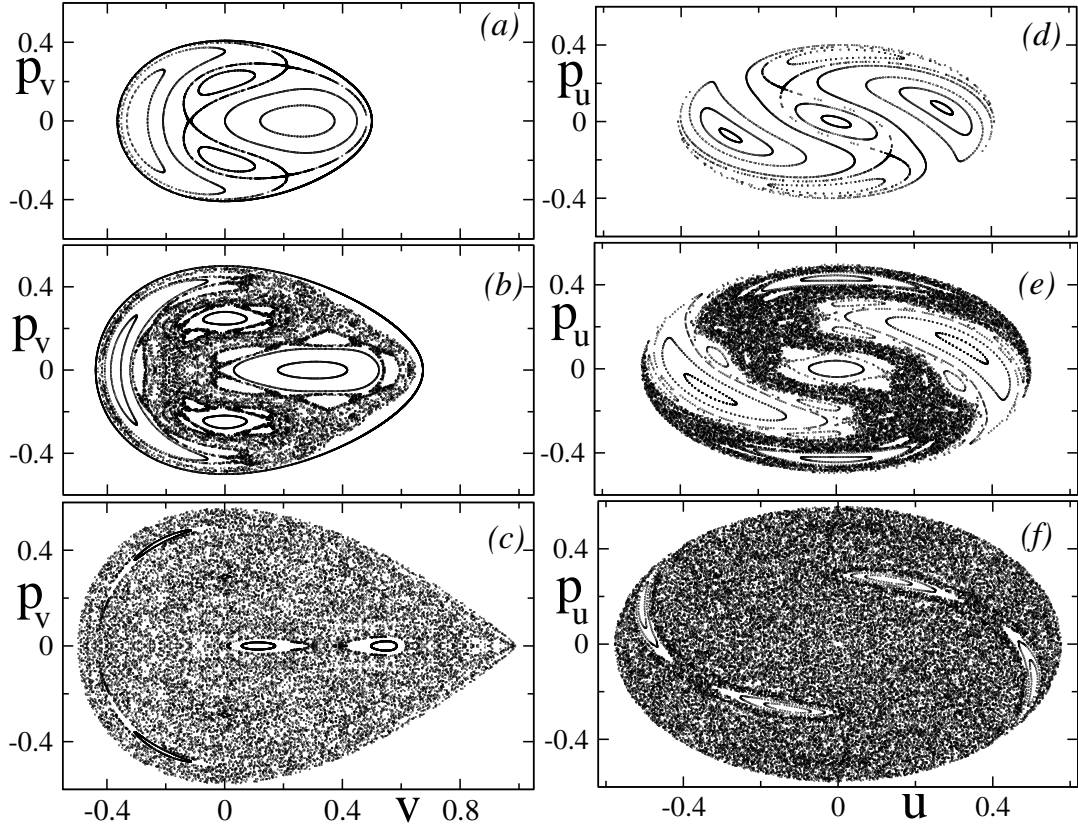


FIG. 1.

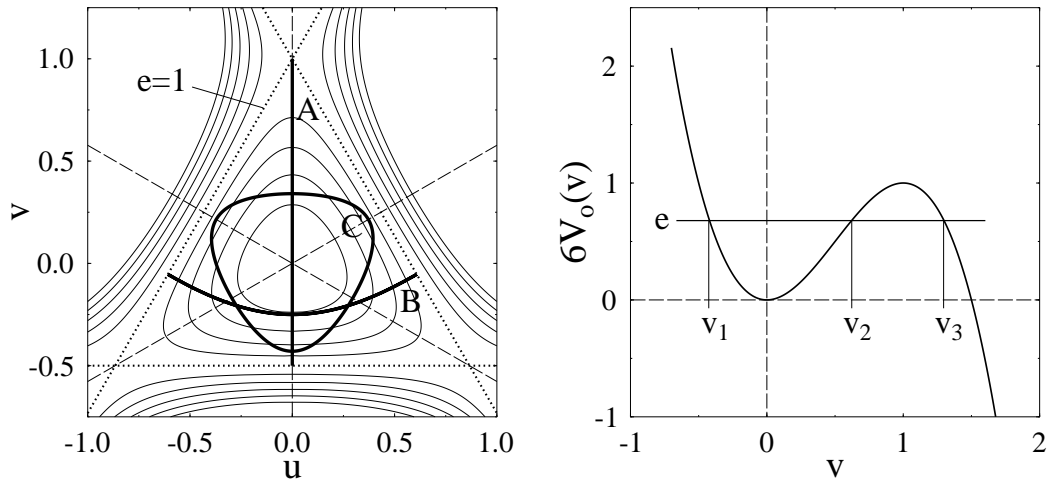


FIG. 2.

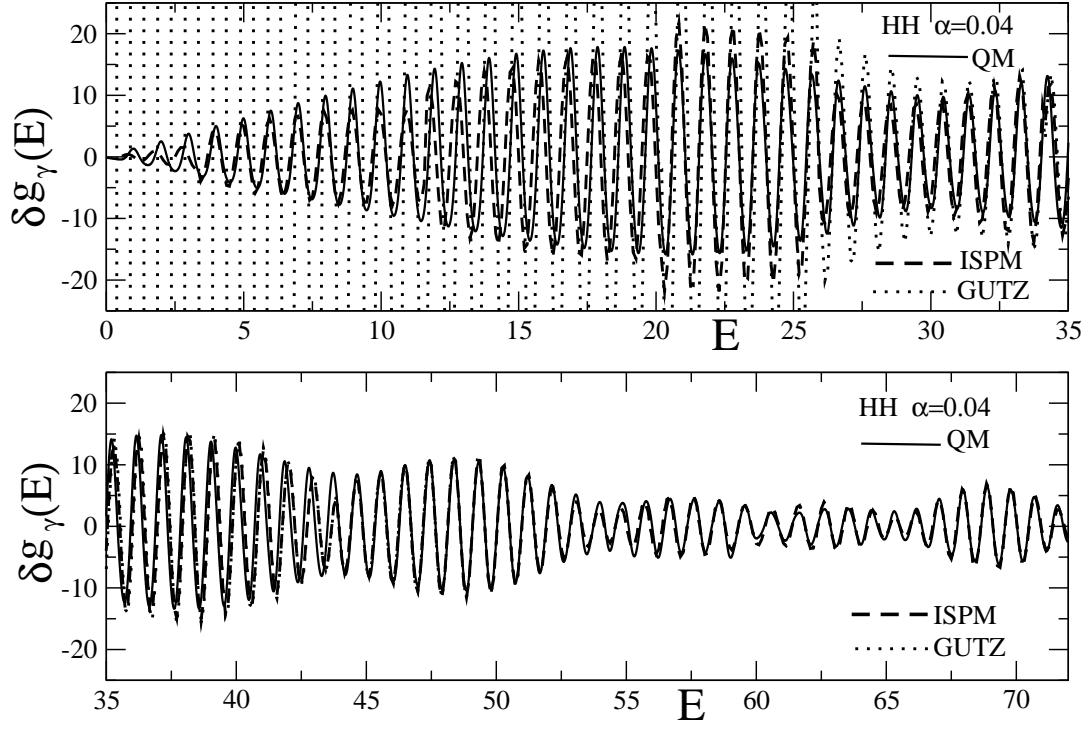


FIG. 3.

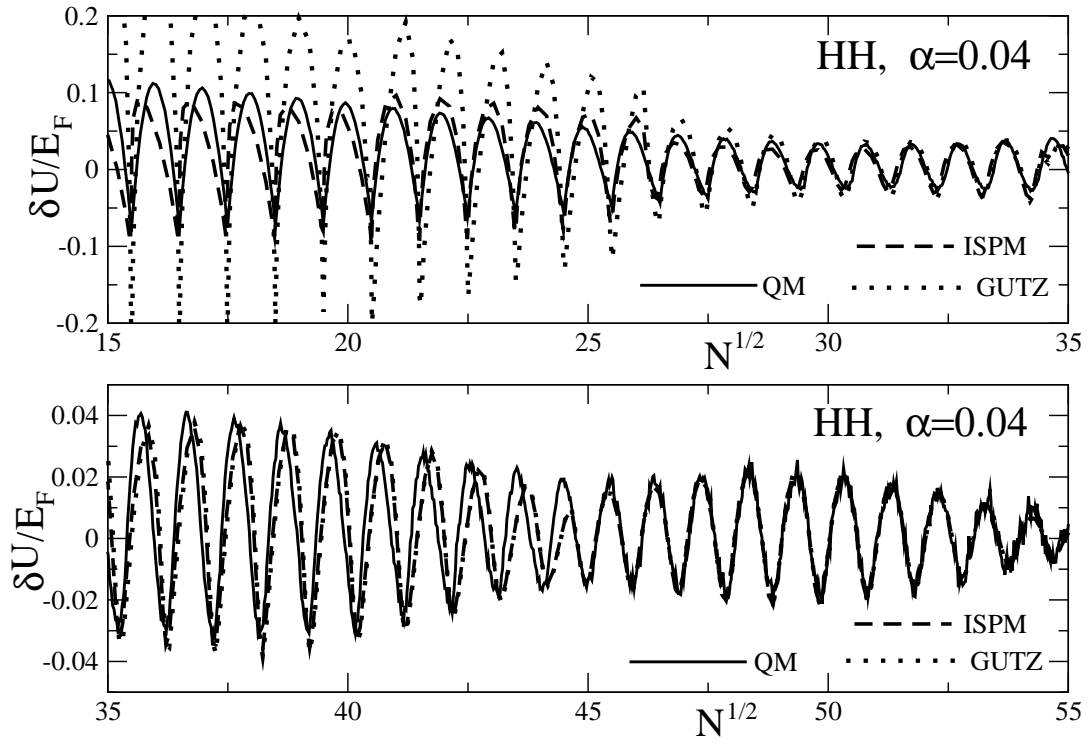


FIG. 4.

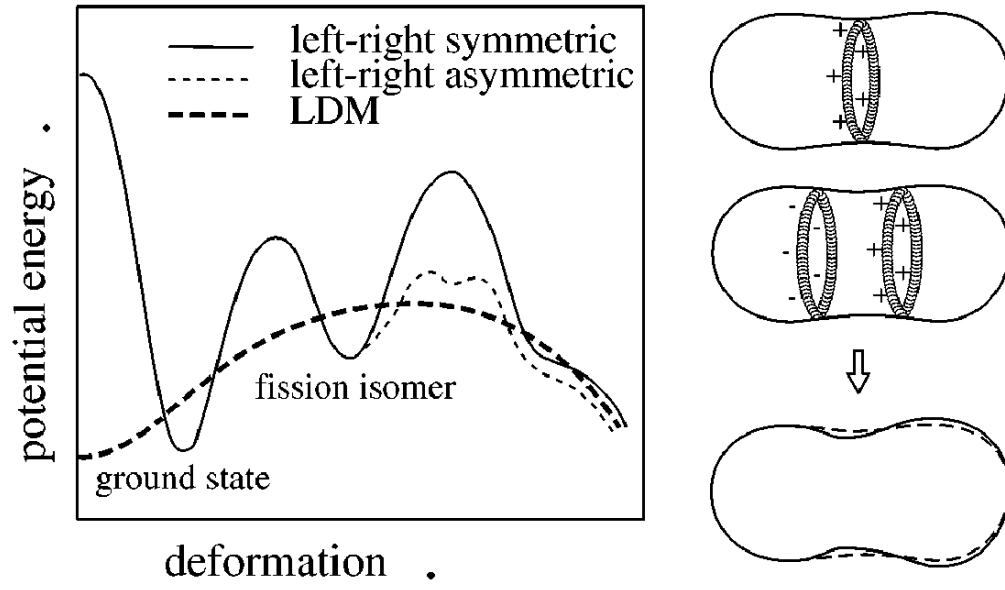


FIG. 5.

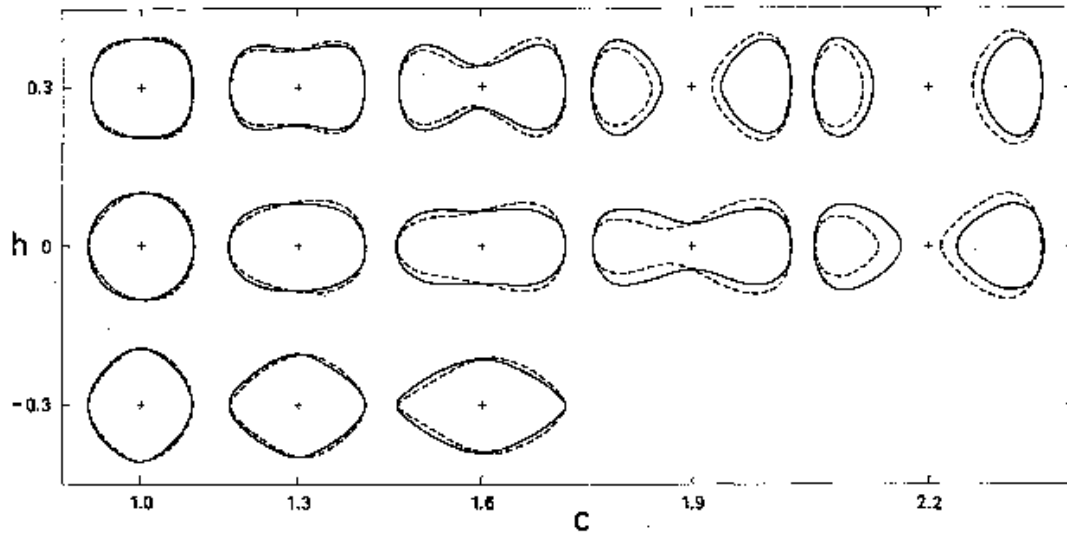


FIG. 6.

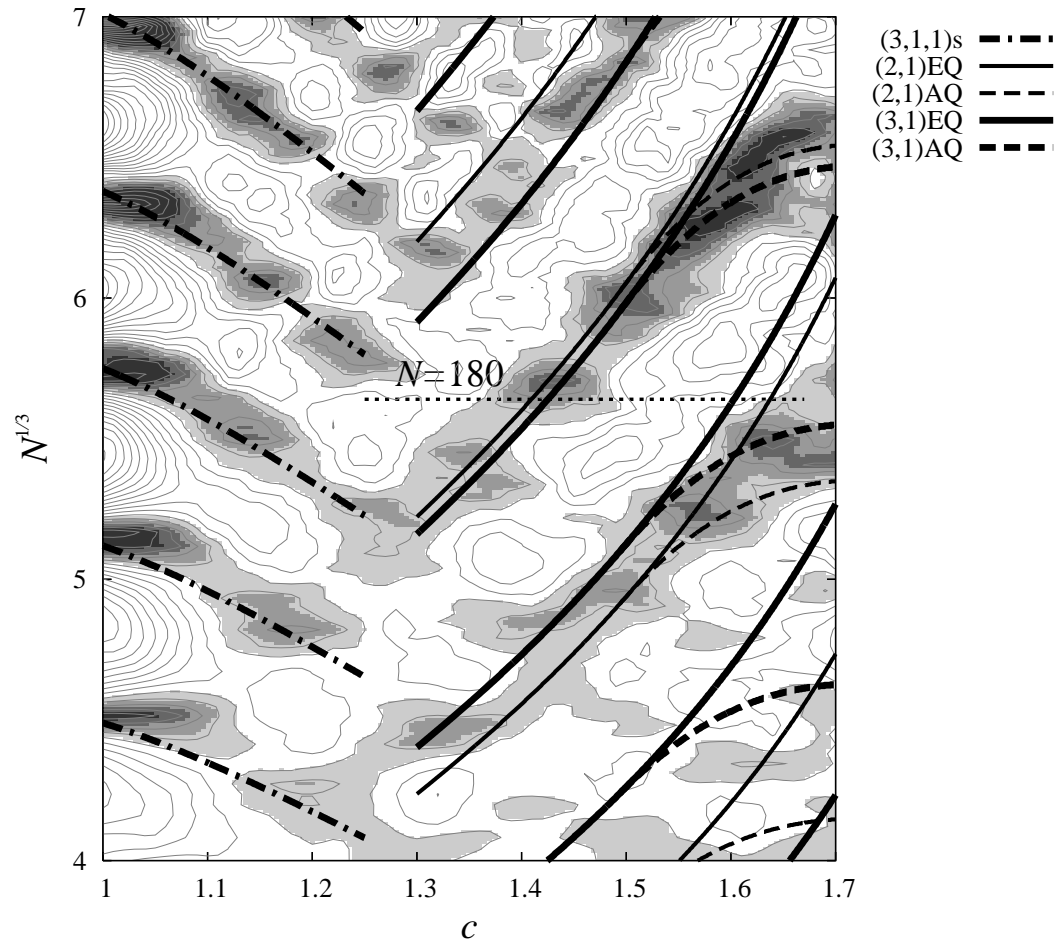


FIG. 7.

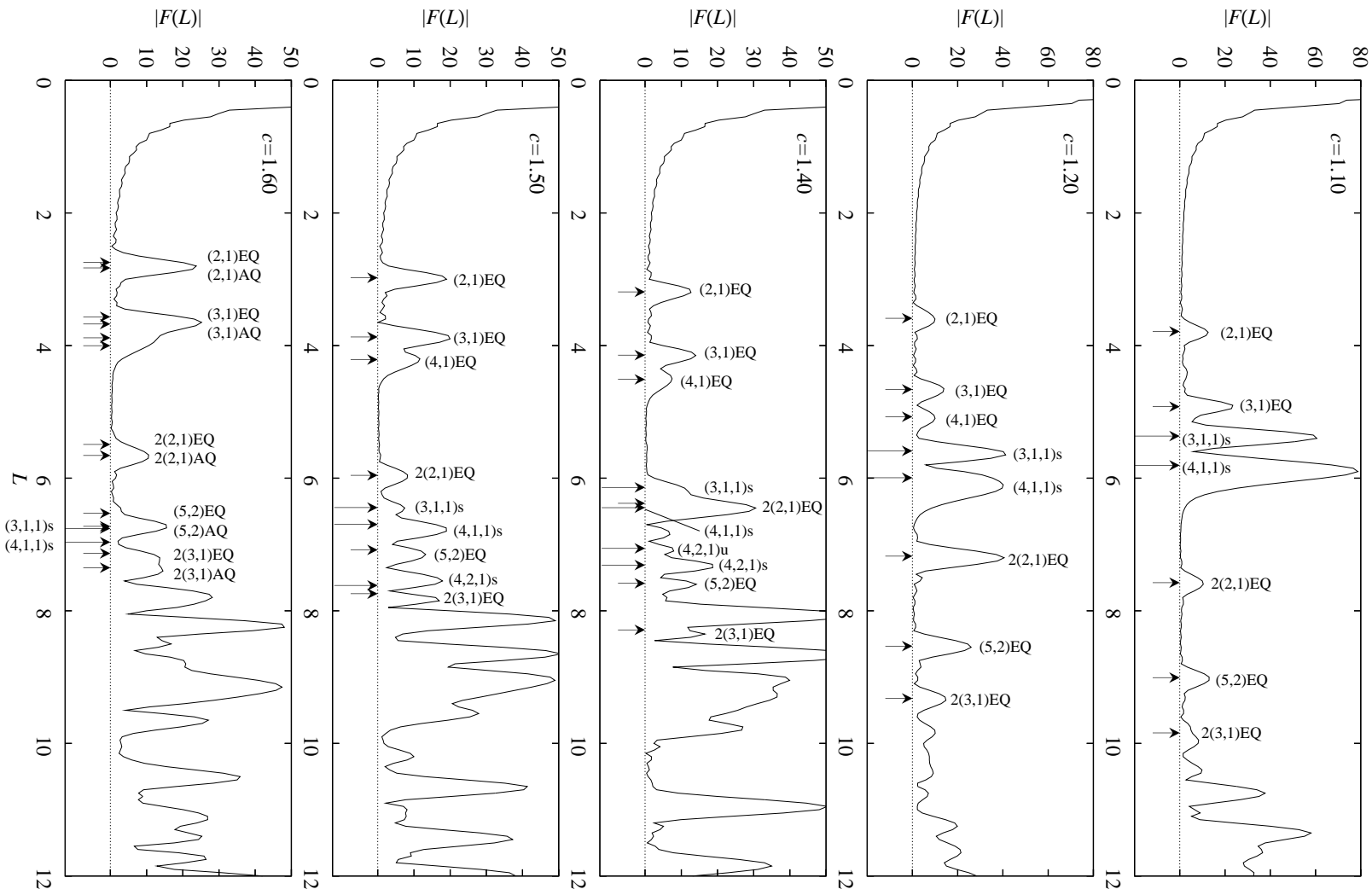


FIG. 8.

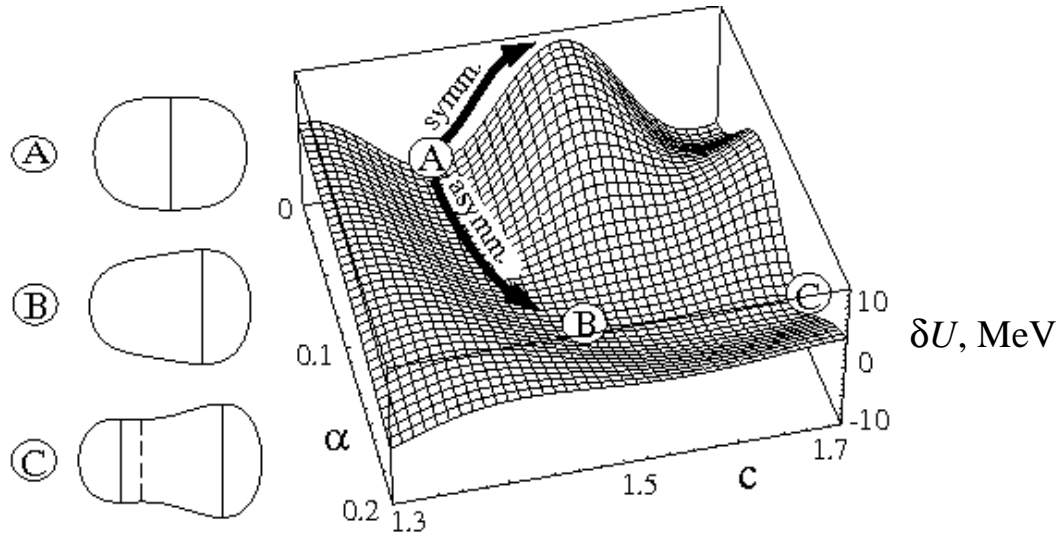


FIG. 9.

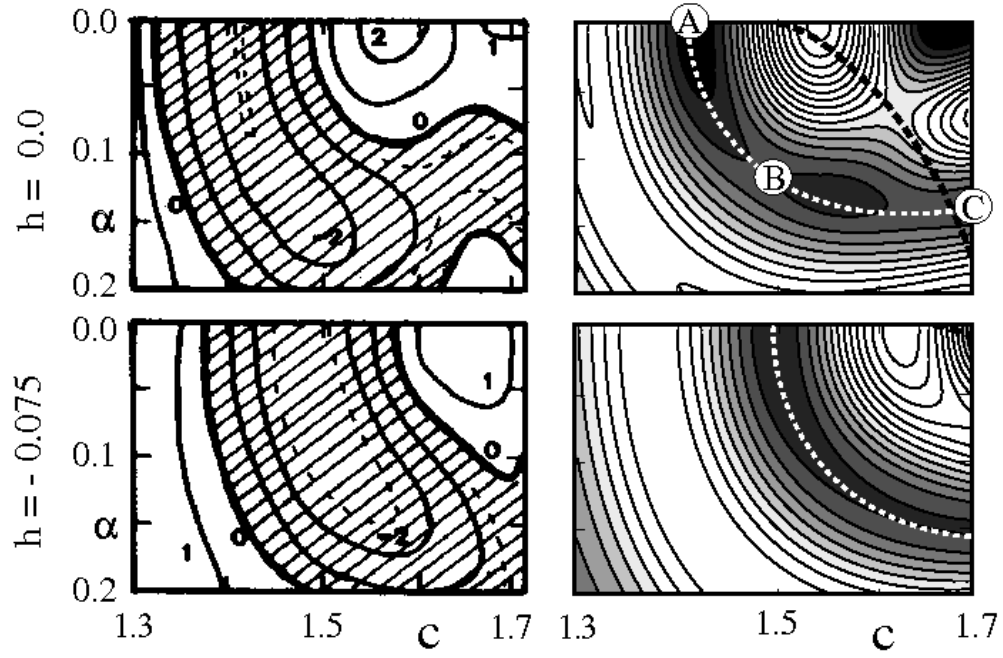


FIG. 10.

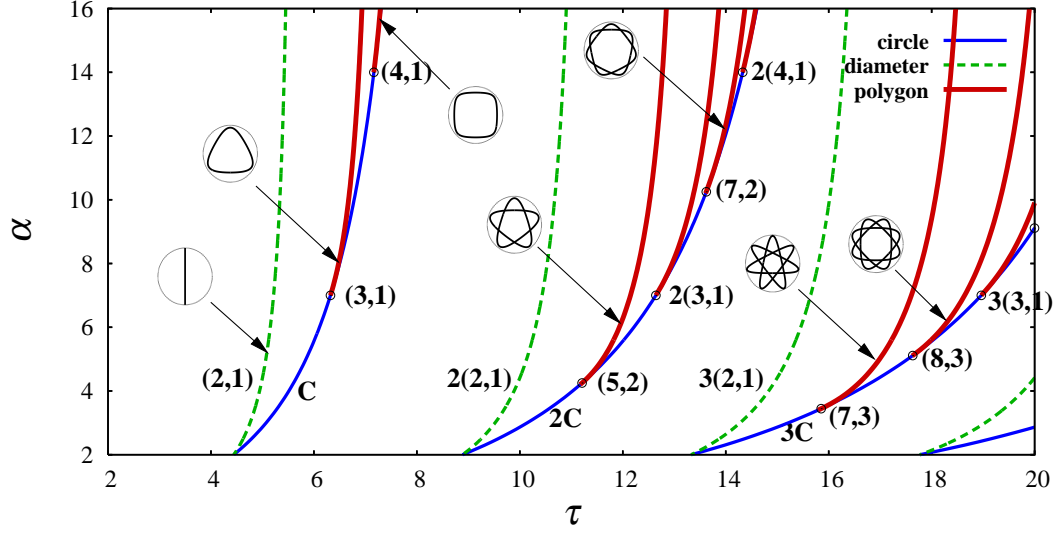


FIG. 11.

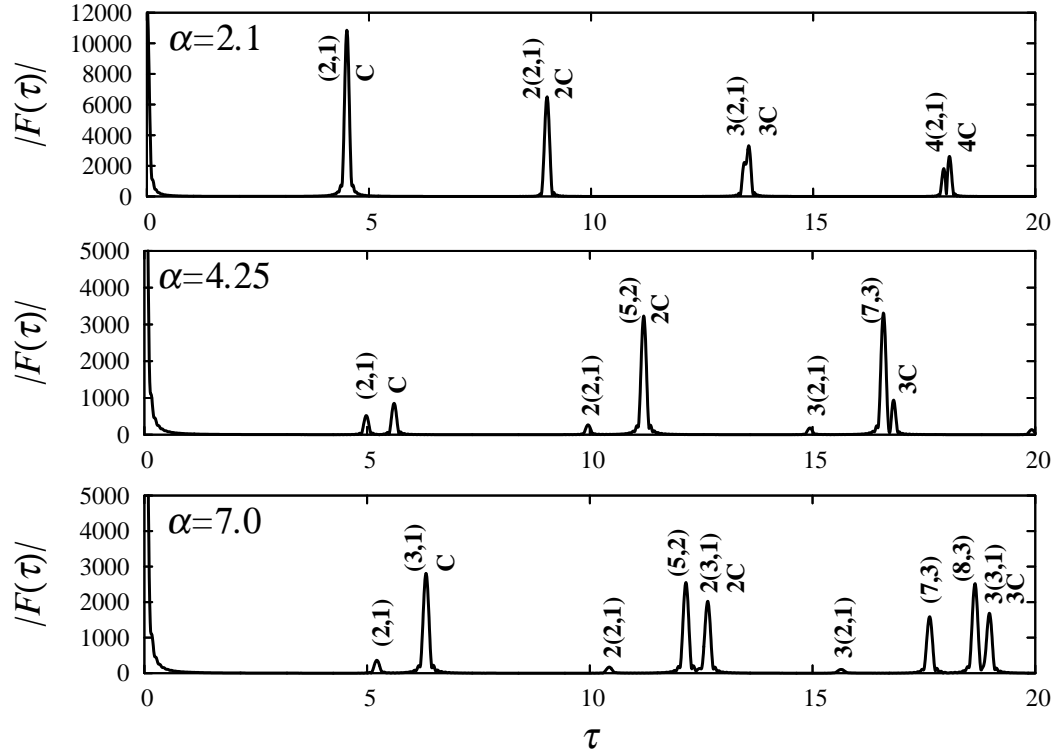


FIG. 12.

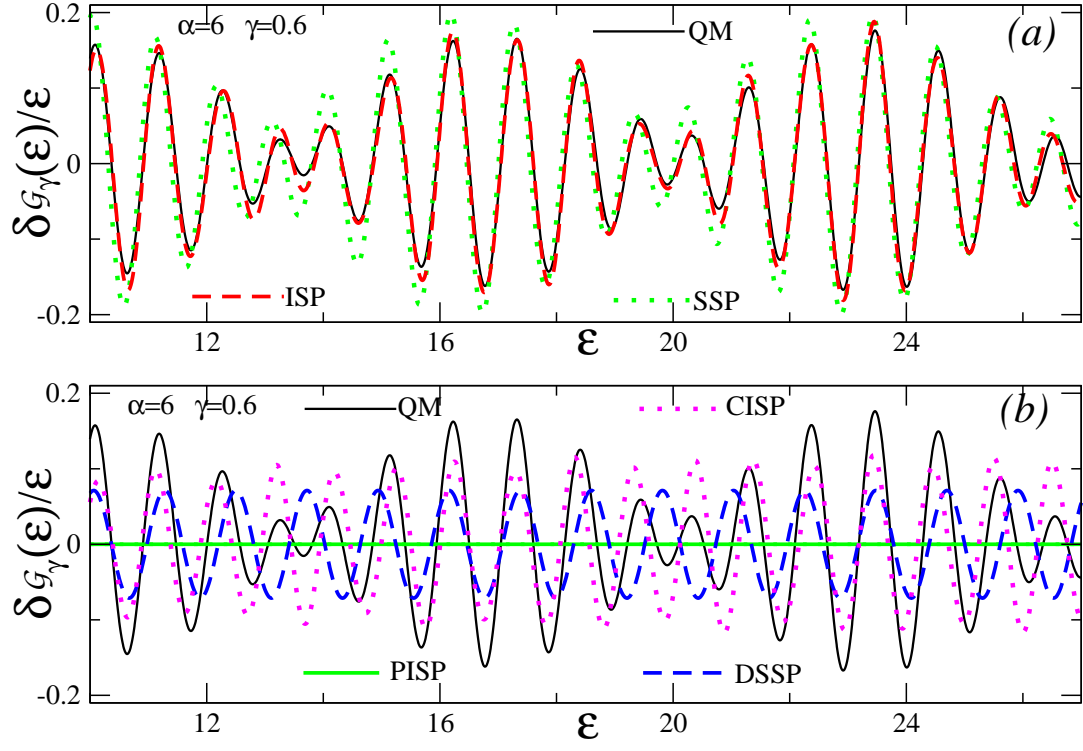


FIG. 13.

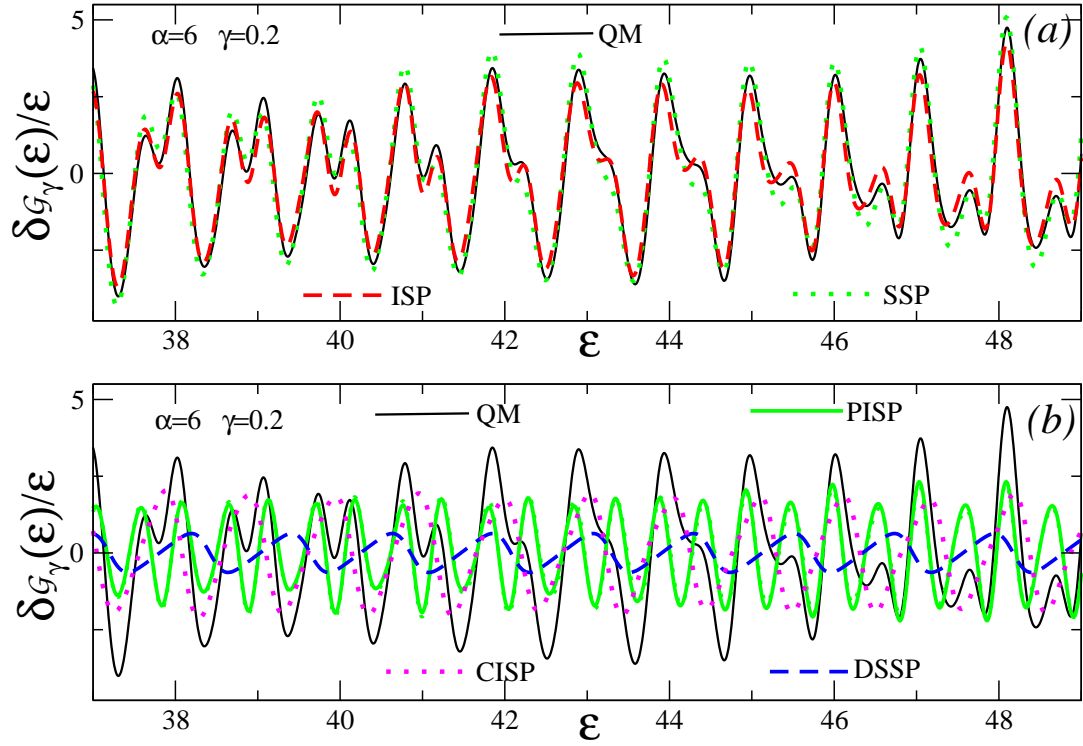


FIG. 14.

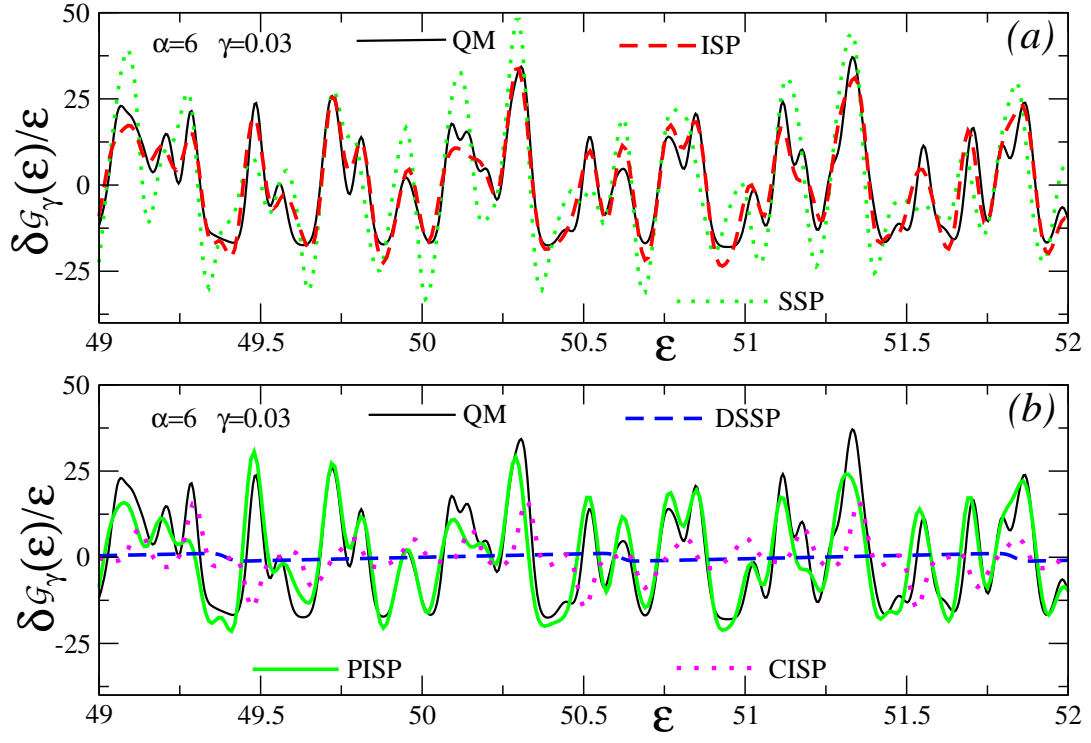


FIG. 15.

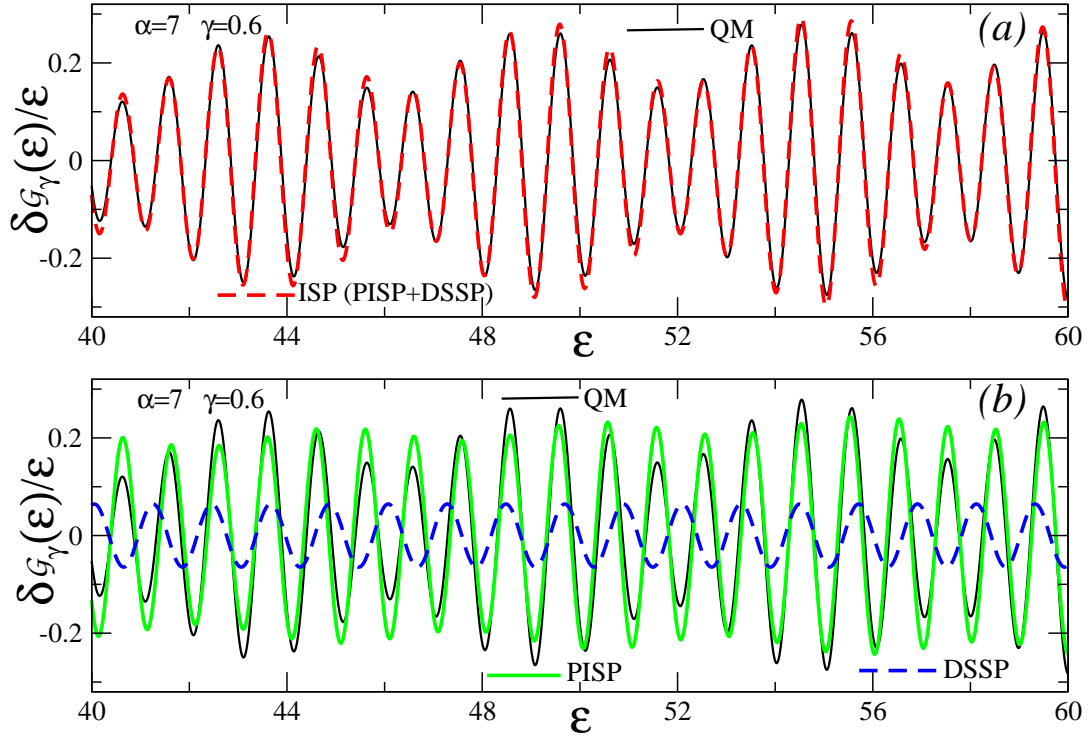


FIG. 16.

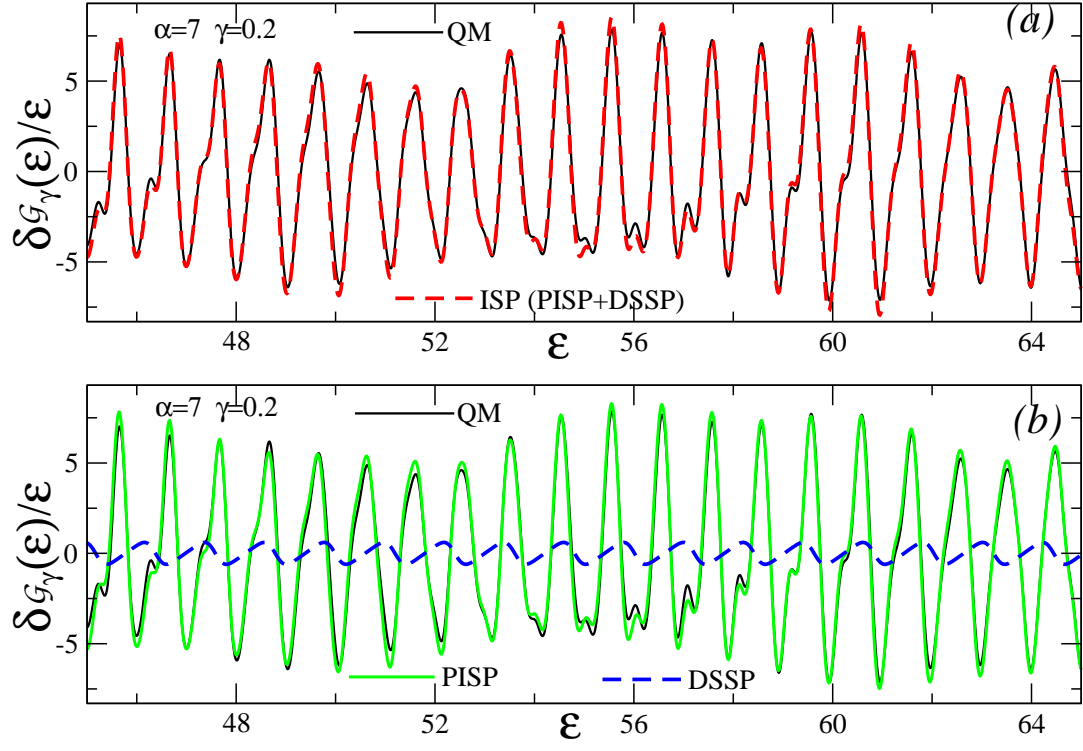


FIG. 17.

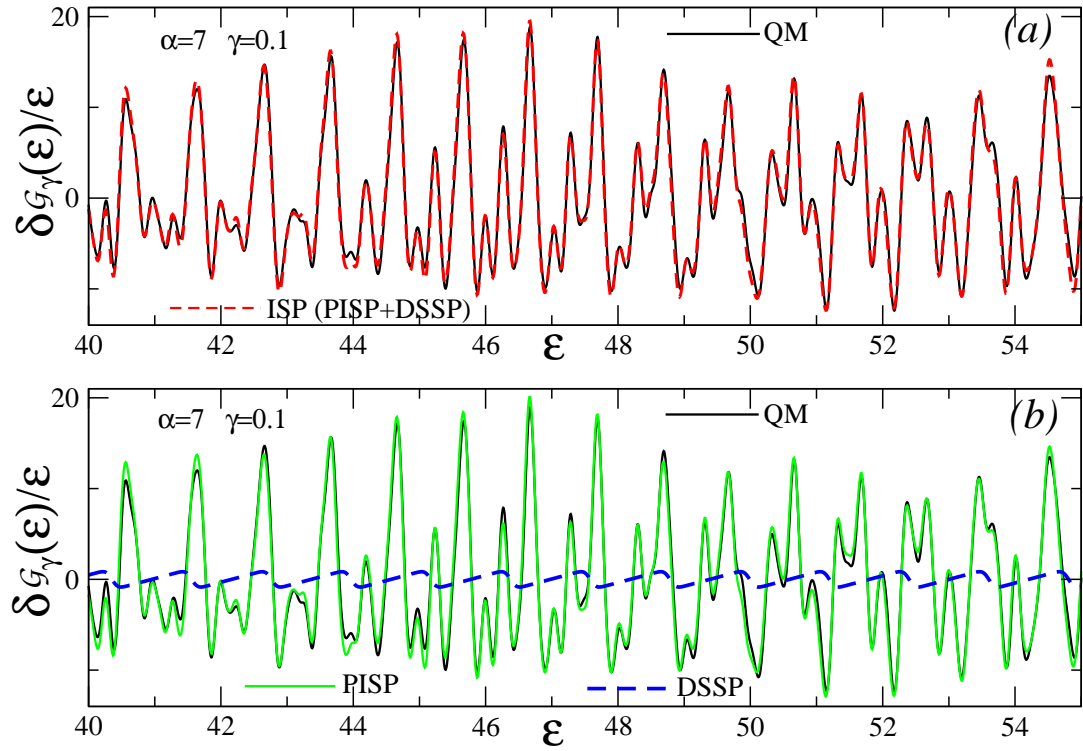


FIG. 18.

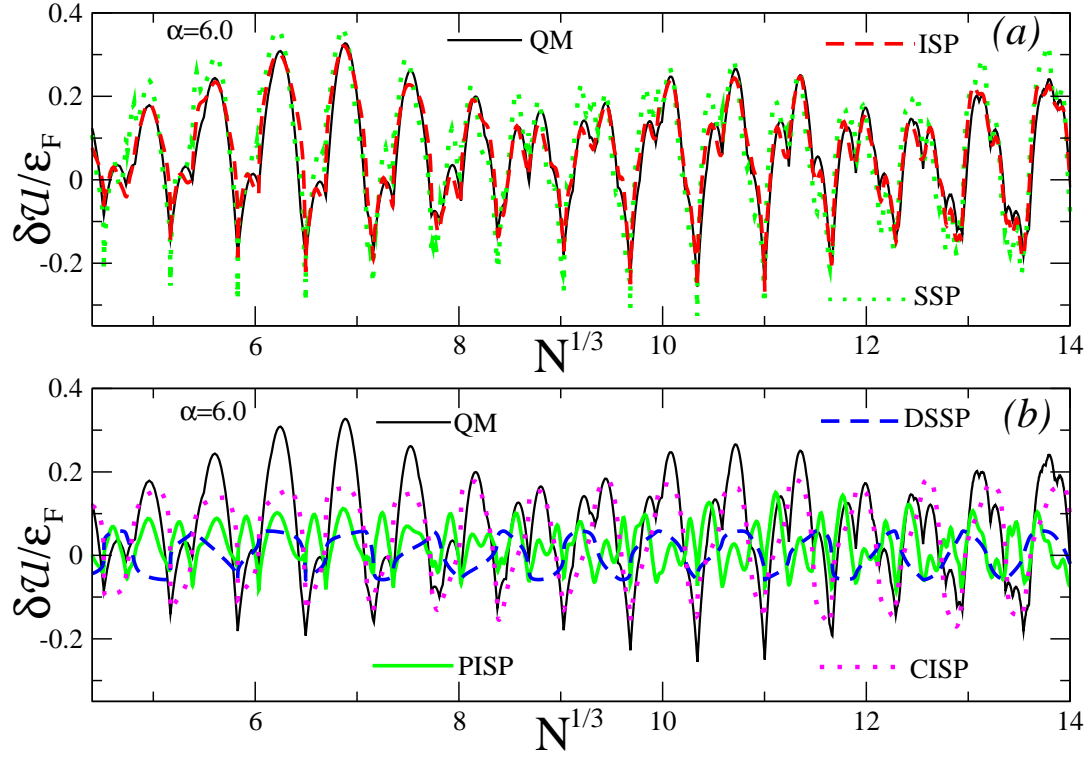


FIG. 19.

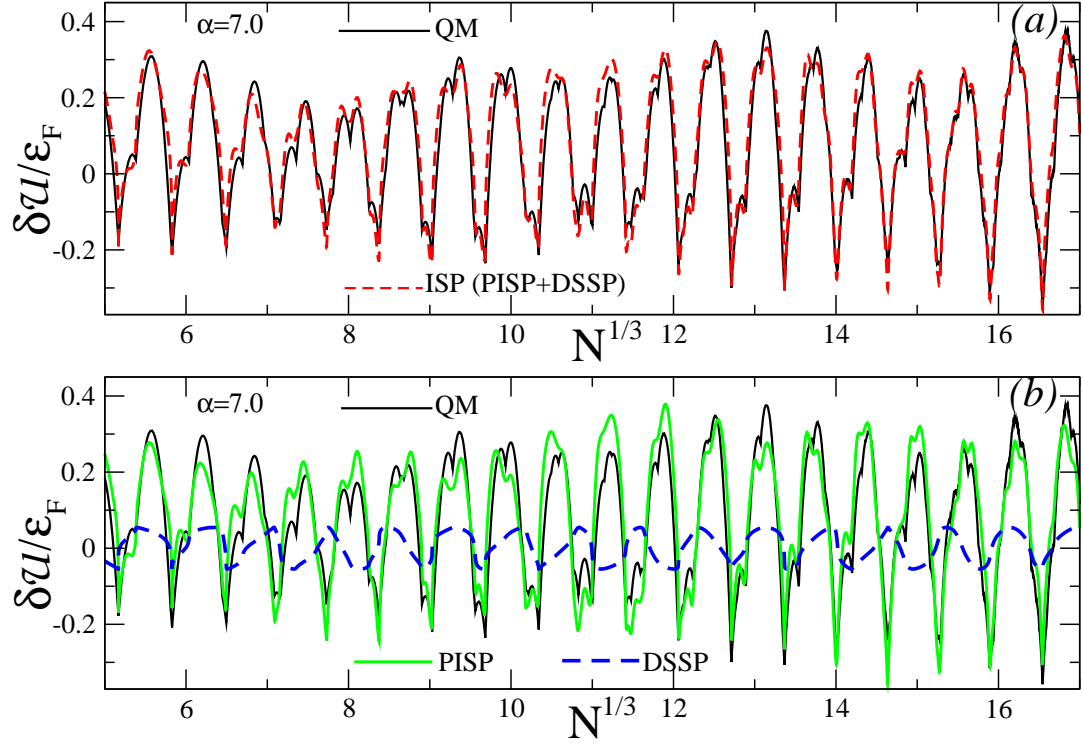


FIG. 20.

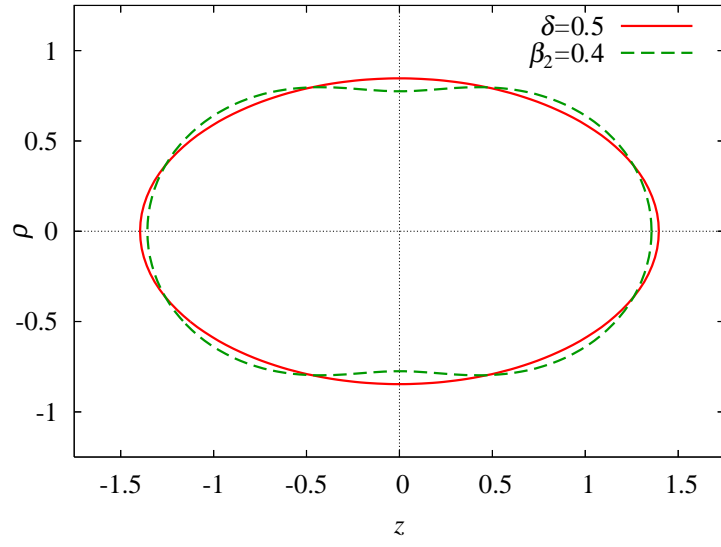


FIG. 21.

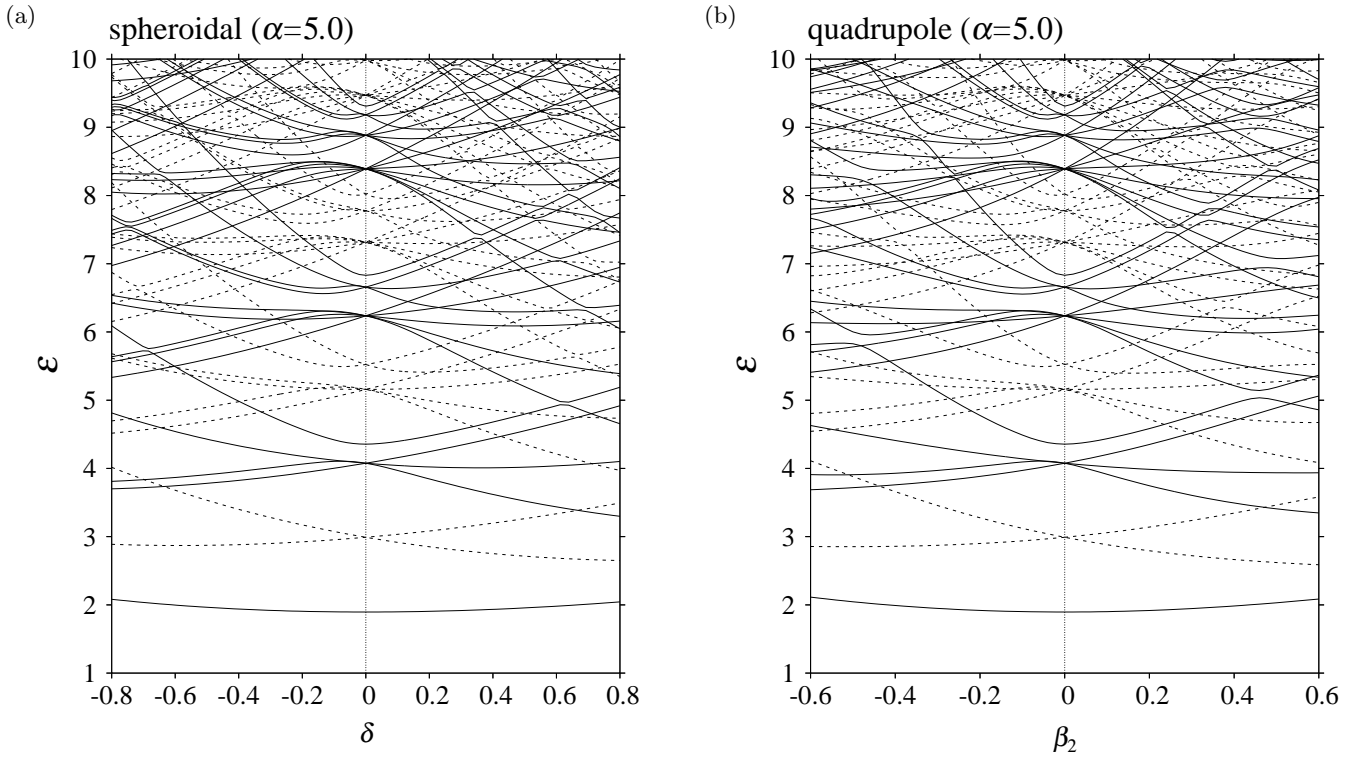


FIG. 22.

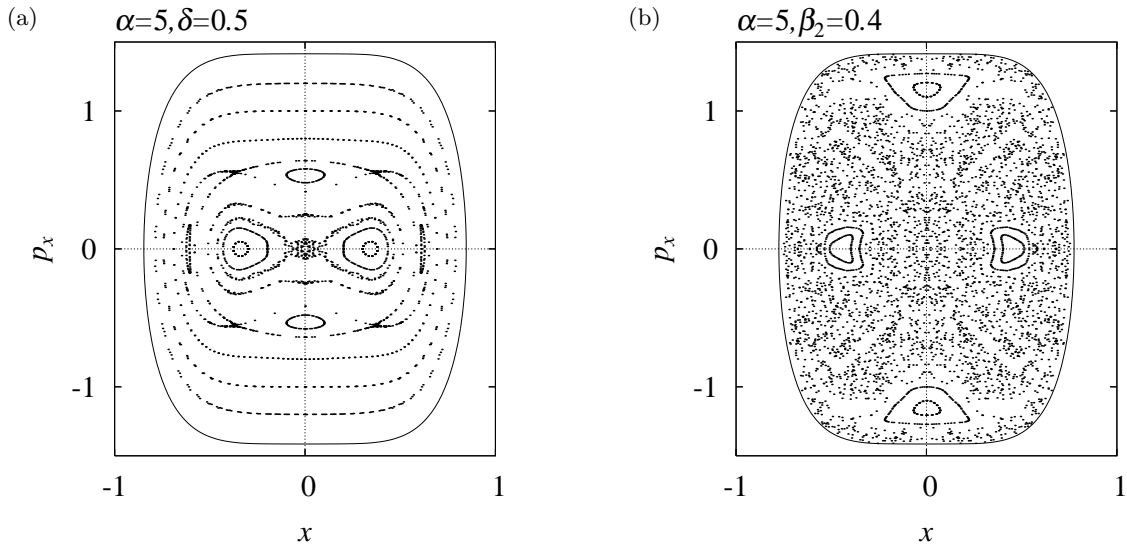


FIG. 23.

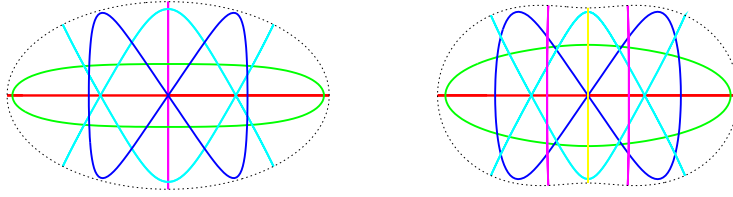


FIG. 24.

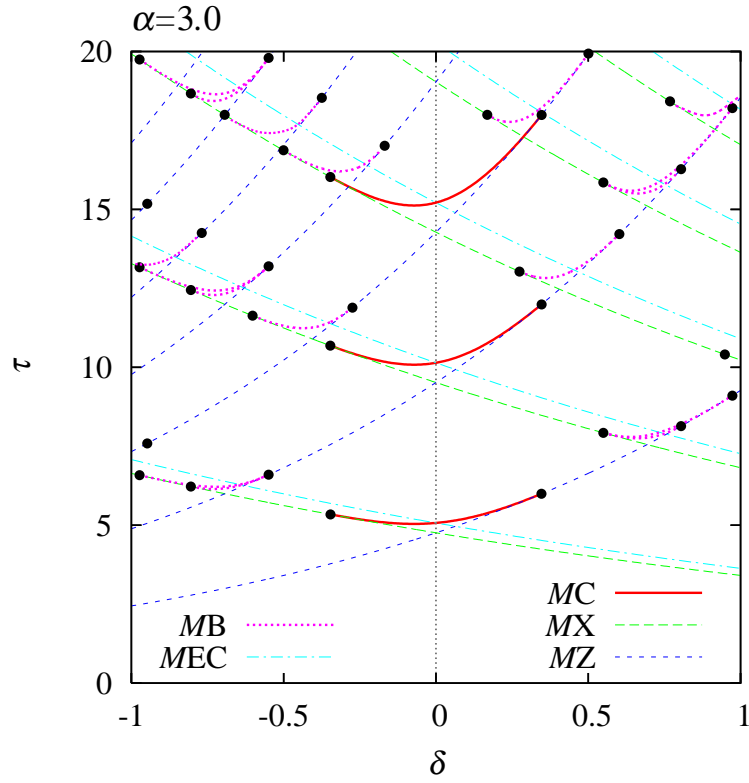


FIG. 25.

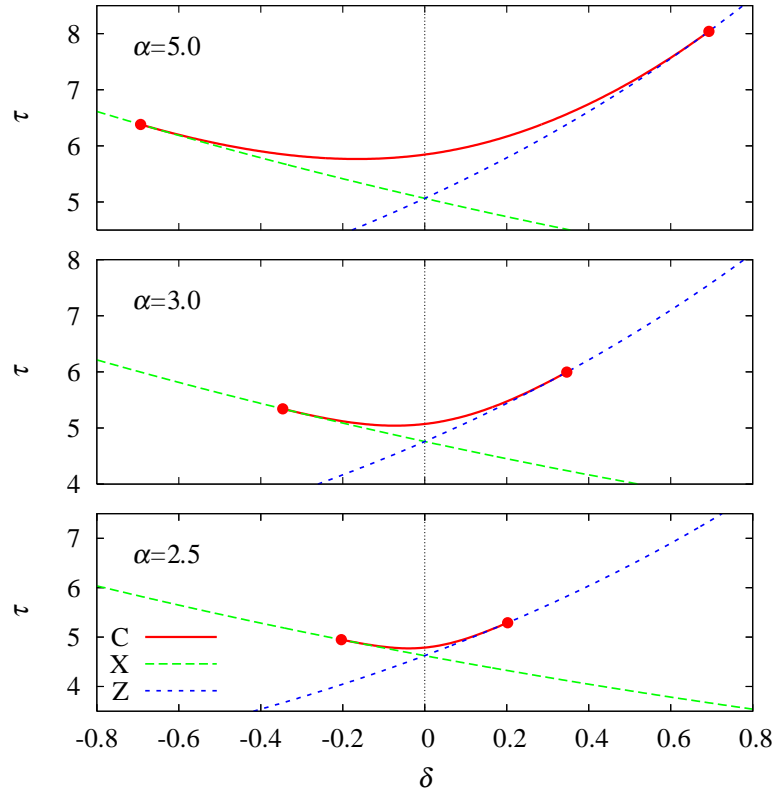


FIG. 26.

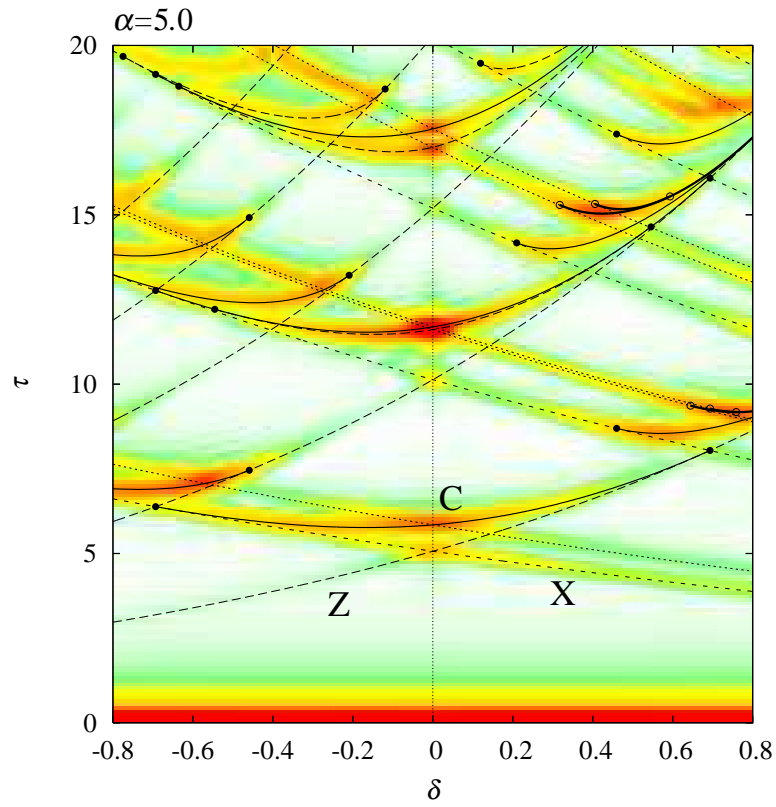


FIG. 27.

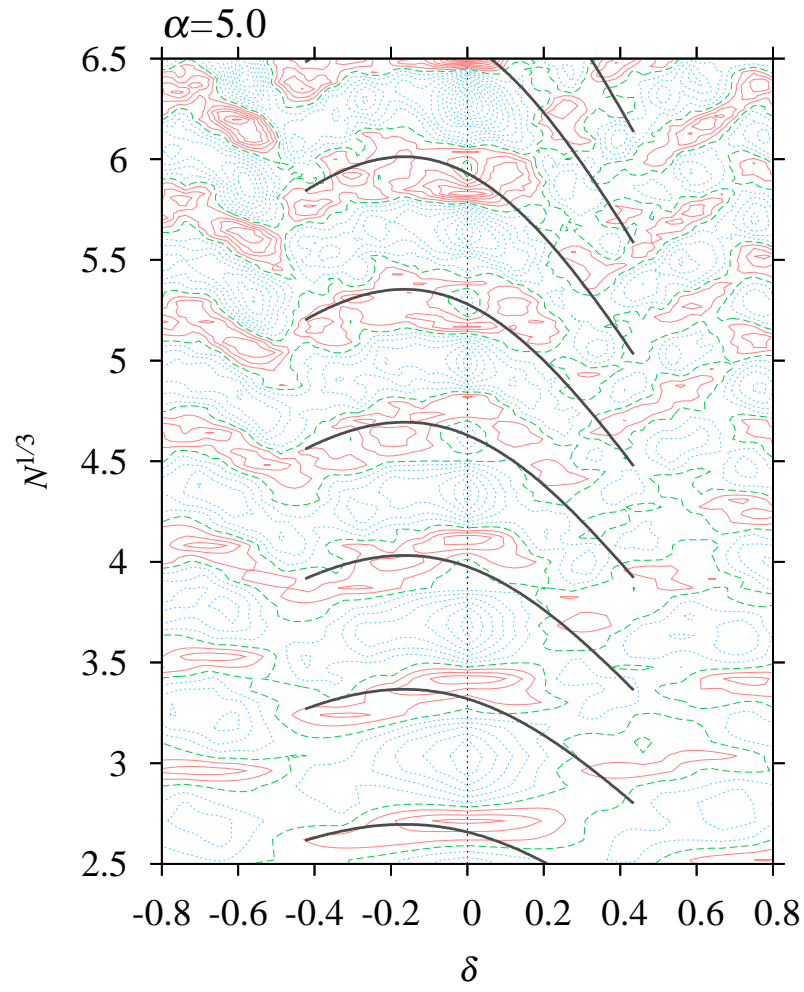


FIG. 28.

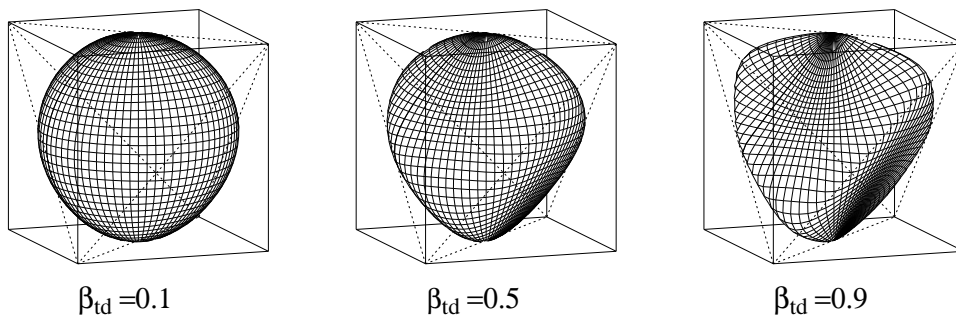


FIG. 29.

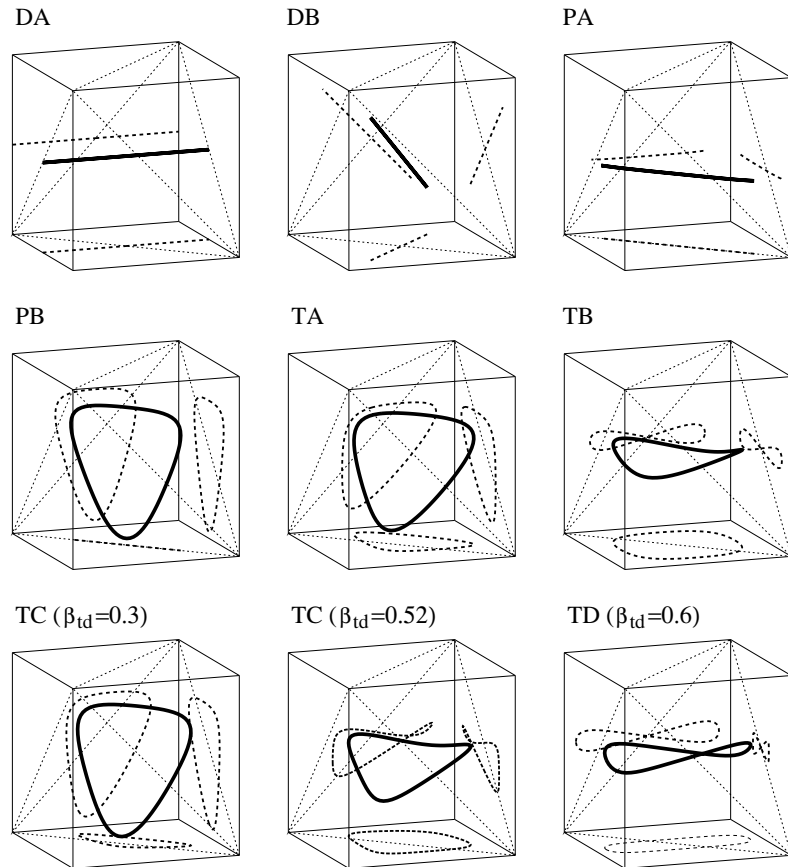
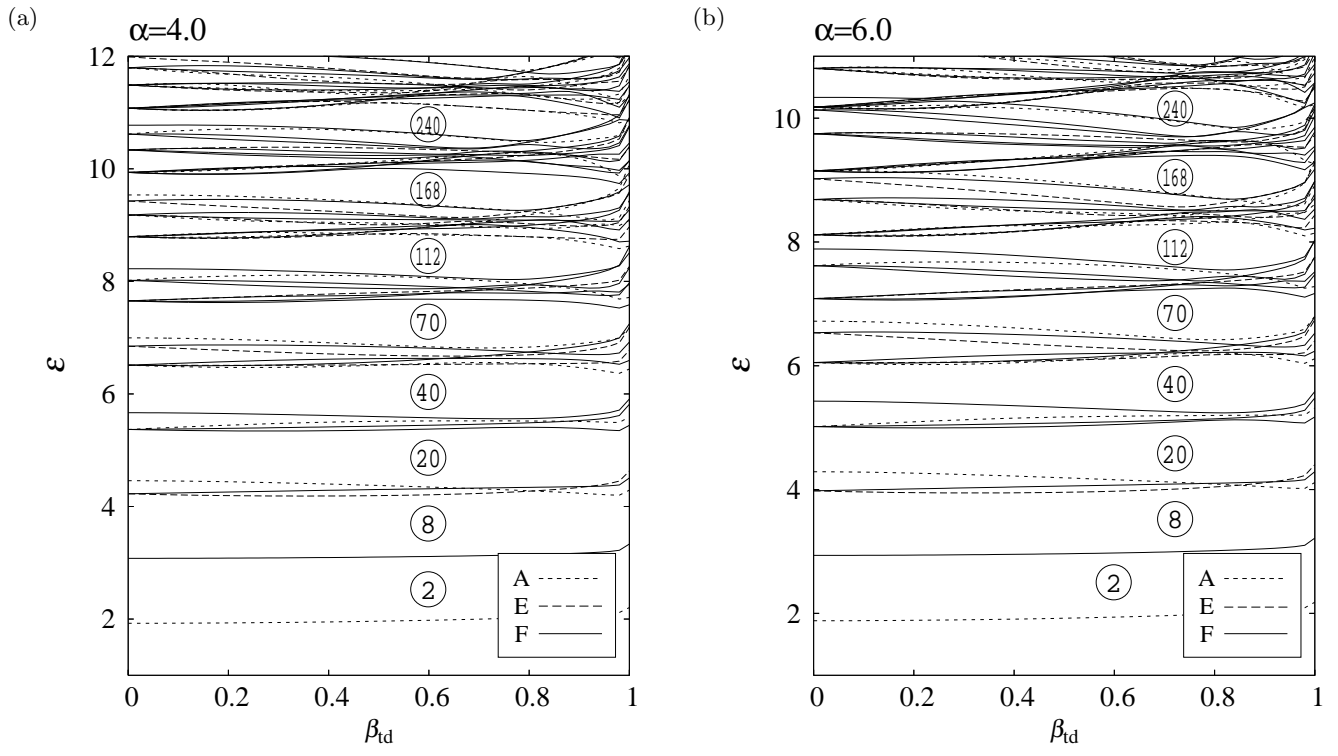


FIG. 31.

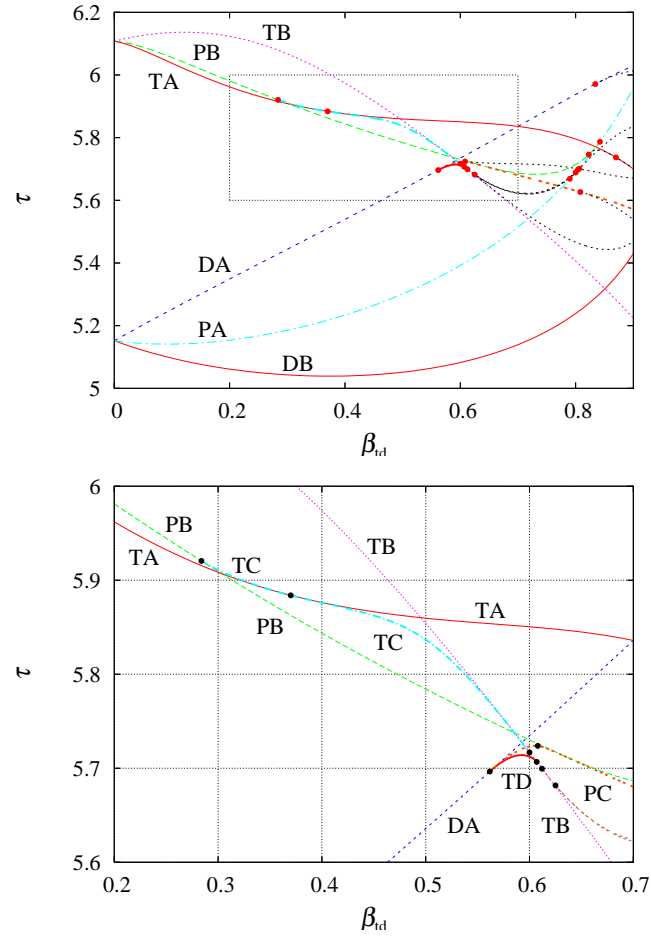


FIG. 32.

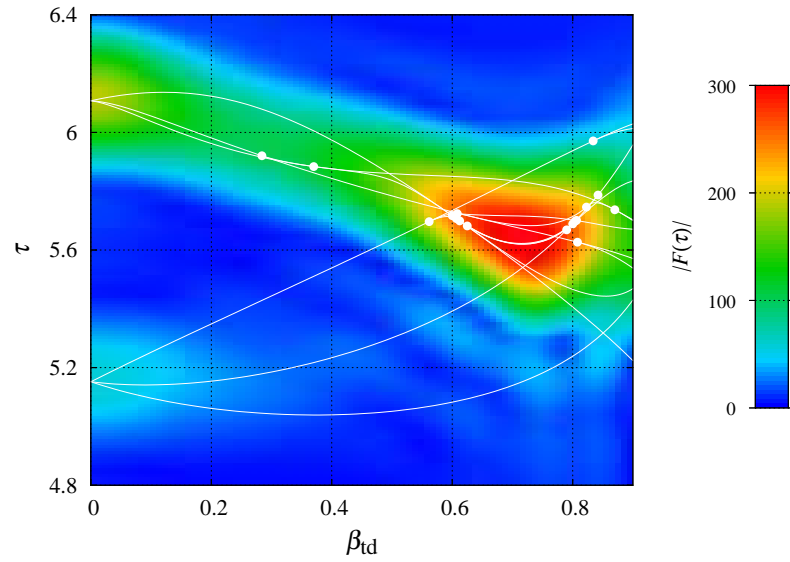


FIG. 33.

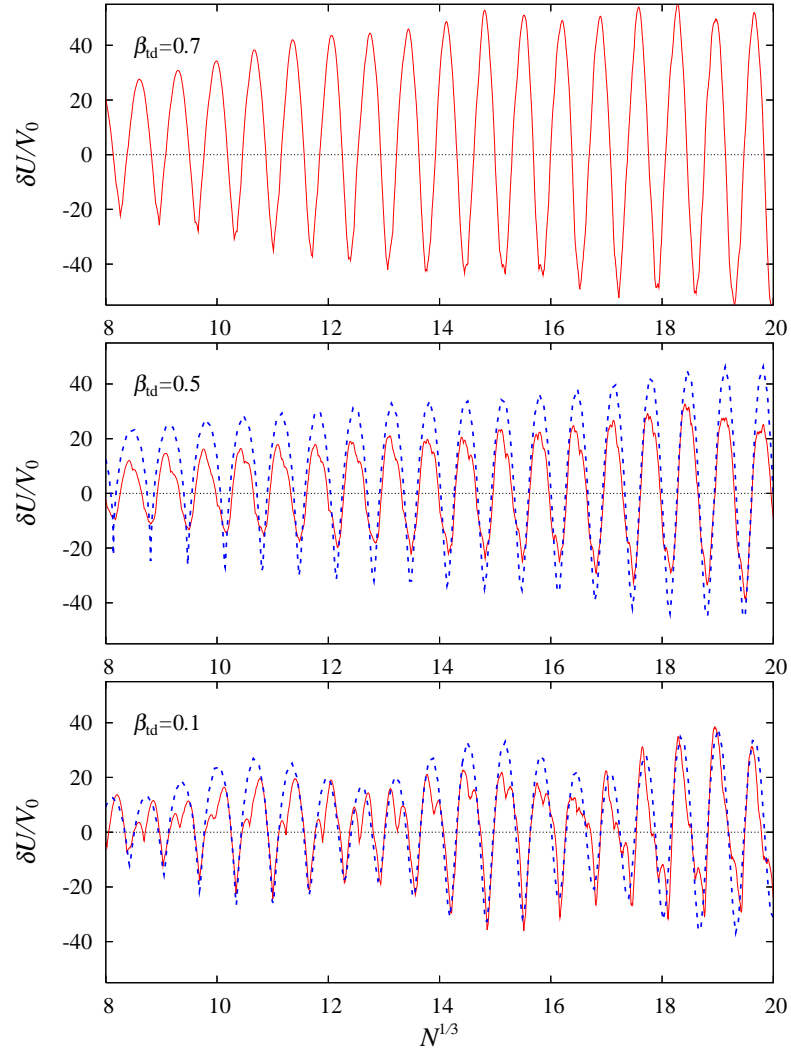


FIG. 34.